UNIVERSITY OF ROMA TRE

DOCTORAL THESIS

High Performance Laser Transmission Spectroscopy: a powerful technique to investigate colloidal suspensions

Author:
Angelo SARRA

Supervisors:
Prof. Fabio BRUNI
Prof. Paolo POSTORINO

January 20, 2020

Contents

List of Abbreviations

AFM	**A**tomic **F**orce **M**icroscopy
DLS	**D**ynamic **L**ight **S**cattering
HPLC	**H**igh **P**erformances **L**iquid **C**romatography
LIA	**L**ock **I**n **A**mplifier
LTS	**L**aser **T**rasmission **S**pectrocopy
MV	**M**icro **V**esicles
NC	**N**ano **C**apsules
NIST	**N**ational **I**nstitute of **S**tandards and **T**echnology
OMV	**O**uter **M**embrane **V**esicles
OPO	**O**ptical **P**arametric **O**scillator
PCB	**P**rinted **C**ircuit **B**oard
SAXS	**S**mall **A**ngle **X**-ray **S**cattering
SEM	**S**canning **E**lectron **M**icroscopy
TEM	**T**ransmission **E**lectron **M**icroscopy

Introduction

In recent years, the study of nanoparticle suspensions has become fundamental in different fields, from medical biotechnologies (e.g. development of innovative vectors for the intracellular drug delivery), to the food industry (e.g. study of new active probiotical agents) and, in general, for the development of new materials.
For such applications, the knowledge of the physical properties of the suspended nanoparticles, in particular size, shape, polydispersity, concentration, and volume fraction, is of paramount importance. Electron and Scanning Probe Microscopies have been widely used for the morphological characterisation, providing essential information on the structure, shape and size of single nanoparticles. However, these techniques usually provide a non statistically meaningful information on size particle distributions, since the study is based on a limited number of images. The statistical significance can be improved by the acquisition of a very large number of images, which, nevertheless, are cost and time expensive, and not representative of the macroscopic level. For these same reasons, microscopy cannot provide quantitative information, indispensable in many applications, on the concentration of the suspended particles.

The statistically significant information of a particle suspension is typically obtained from measurements of light scattering. The traditional technique of Dynamic Light Scattering (DLS) is extremely efficient for this purpose and is extensively employed. However, DLS has three important limitations: *i)* it does not provide absolute concentration values but relative to the different components only; *ii)* size determination is provided in terms of hydrodynamic radius that generally overestimate the real one, as strongly depends on suspending fluid properties (i.e., temperature and viscosity) and fluid-particle interactions; *iii)* scattered light intensity shows a high power dependence on the particle radius. Thus a limited number of large particles (often even just impurities or dust particles) can mask the contribution of a large number of small particles.
To overcome these drawbacks, alternative techniques based on the measurement of turbidity of the suspension have been proposed. However, although these techniques are conceptually quite simple, their practical implementation has presented rather significant difficulties, which have severely limited their applications.

Only in the last ten years, thanks to the development of the tunable lasers, a new technique based on Laser Transmission Spectroscopy (LTS) has been proposed by Li et al., who realised the first LTS apparatus in 2010. LTS allows to determine the density distribution of colloidal suspensions measuring the transmittance of a laser beam as a function of the wavelength. The particle density distribution, as a function of their radius, can be calculated through the Beer-Lambert law and the Mie scattering theory. The transmission data can be analysed and inverted by a mean square root-based algorithm that outputs the particle density distribution as a function of size.
In principle, this method allows to determine the size distribution of the particles

with a radius in the $10\ nm - 2\ \mu m$ range, and the absolute concentration, with values between $10^5\ part/ml$ and $10^7\ part/ml$. The possibility of measuring such low concentrations represents a great advantage, particularly important for samples difficult to prepare, such as purified proteins, constructs of oligonucleotides, exosomes and microvesicles. Moreover, LTS allows to have information also on particles of different shape, e.g. shells, rod-like particles, etc.

During my PhD program, I have designed and assembled an innovative experimental apparatus for LTS, which allows to obtain much better performances with respect to that one proposed by Li et al. Furthermore, I have developed a Fortran code for data analysis. The optical source emplyed in this apparatus is a pulsed laser equipped with a Nd: YAG pump laser (pulse duration 3-5 ns), tuned through an optical paramentric oscillator over a wide range of wavelengths (from about 410 to about 2600 nm). This source is a complex optical system which, using a pump laser and the technology based on non-linear optics (parametric optical oscillators, generators of second and third harmonics), is able to produce a laser beam that can be tuned on a large wavelength range. The whole optical system is able to produce two identical beams: the first impinges on the sample, i.e. particles + solvent, and the second on the solvent only (reference).
Following the method proposed by Li et al., in order to cancel out the wavelength dependence of the optical components and detectors, the currents generated by the photodetectors are collected two times, by swapping the sample and reference positions. The transmission coefficient is then calculated as the double ratio of these measured signals. With this configuration, LTS performances appear significantly better than ones obtained with DLS and electron microscopy. LTS capability to provide size and absolute concentration of particles has revealed fundamental for some interesting cases of study in different field as pharmaceutics, biophysics, and cultural-heritage. In particular, we studied liposomes for drug delivery, microvesicles derived from Microglia cells in brain mice cancer, and nanocapsules as biocide container for stone manufacts preservation.

Although the absolute concentration estimate results to be accurate and rather robust, a close inspection of the results obtained from test measurements on standard polystyrene nanoparticles showed not negligible inaccuracies. In particular, the width of the size distributions was partly uncontrolled, due to the strong dependence of the analysis on the experimental errors.

To overcome this drawback, in collaboration with the Department of Industrial and Information Engineering of the University of L'Aquila, we developed an innovative lock-in amplifier for the detection of the signal. Standard techniques for small-signal detection indeed typically employ lock-in amplifiers whose sensitivity and resolution are limited by the selected full-scale. These characteristics maximise the apparatus sensitivity and resolution respect to the small amplitude variations of the input signal. In particular, we designed a new, highly performant, variable gain, lock-in amplifier that, optimized for repetition rate and pulse duration of our laser, allows to detect small changes of the input signal.
Thanks to this custom variable gain lock-in amplifier, we proposed an alternative method based on a calibration procedure, in which the gain of the new custom lock-in is tuned, for each wavelength, to balance the transmitted intensity in both the experimental optical paths. After the calibration run, it is possible to obtain the transmittance, and the related extinction coefficient, as the single ratio between the

measured intensities. The performances of the new balanced method, which exploits the custom lock-in amplifier, result to be better than those ones obtained from the double ratio procedure. In particular, the width of the size distribution is remarkably reduced, providing a more reliable system characterisation.

In view of a future LTS analysis, a strong effort has been also devoted to the study of Outer Membrane Vesicles (OMVs) produced by Escherichia Coli bacteria (i.e. the analogous of exosomes for bacteria) by DLS and Small Angle X-rays Scattering (SAXS). DLS results showed interesting membrane properties, such as temperature driven phase transition, which could allow to relate OMVs with the progenitor cells. Furthermore, SAXS analysis allowed to determine the membrane thickness variation across the transition.

In these last months, thanks to a new funding, we were able to extend the accessible laser wavelength range down to the ultraviolet region. At present, indeed, the wavelength ranges from 210 nm to 2600 nm. With this upgrade, we hope to reach LTS higher performances both in terms of minimum size (10 nm of radius) and in concentration ($3-4$ order of magnitude lower). We believe that these enhanced LTS performances could be particularly useful for a deeper insight of this kind of systems.

The outline of the thesis is herein presented.

Chapter 1: Laser Transmission Spectroscopy: theory and analysis software

In this chapter the basic concepts of Laser Transmission Spectroscopy (LTS) are reported. In particular, the theoretical model that allows to calculate the extinction matrix and solve the inversion problem, needed to obtain the particle density distribution, is described in details. Finally, the basis of the algorithm for the data analysis is introduced.

Chapter 2: Experimental setup and measurement technique

Here, I present the experimental setup and the detection system developed for the transmission measurements. I report the method developed by Li. et al. [1] to obtain the particle transmission coefficient from the measured transmitted intensities.

Chapter 3: LTS test measurements of standard samples

In the present chapter, I report the measurements and the computational analysis to determine the sensitivity of the apparatus and the error associated with the determination of the radius and concentration. To compare the peroformances of our experimental setup with other standard techniques (DLS and SEM), we measured samples with different size and concentration.

Chapter 4: Cases of study

Some interesting cases of study, for which LTS ability to provide size and absolute concentration of particles has been revealed fundamental, are presented. In particular, I report the results obtained in different field as pharmaceutics, biophysics and

cultural-heritage. The studied samples are liposomes for drug delivery, microvesicles derived from Microglia cells in brain mice cancer and nanocapsules as biocide container for stone manufacts preservation.

Chapter 5: Variable gain lock-in amplifier for a new "balanced" measurement method

In this chapter, I explain the new "balanced" method, implemented thanks to the developed tunable-gain lock-in amplifier, and report the test measurements to validate the method itself.

Chapter 6: Towards LTS measurements of exosomes

In this chapter, I report a preliminary biophysical characterisation performed by DLS, TEM and SAXS of OMVs. The results showed interesting membrane properties (phase transitions) that allowed to discriminate OMVs from Escherichia coli grown at different temperatures.
These properties will deeply studied through LTS technique in the next future.

Chapter 1

Laser Transmission Spectroscopy: theory and analysis software

In this chapter the basic concepts of Laser Transmission Spectroscopy (LTS) are reported. This technique allows the study of the dimension and the absolute concentration of particles in suspension through the measurement of the transmission coefficient as a function of the probing laser wavelength and the computation of the extinction matrix.
In the first part of the chapter, we present the theoretical model that allows to calculate the extinction matrix and solve the inversion problem, needed to obtain the particle density distribution. Finally, we introduce the basis of the algorithm for the data analysis.

1.1 The Beer-Lambert law

Our interest is focused on the interaction of a laser beam with a suspension of particles. As shown in figure 1.1, it is possible to assume a sample with optical path z and particle density n.

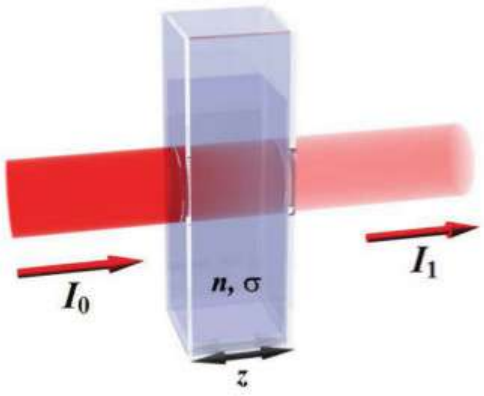

FIGURE 1.1: Laser beam trasmitted through a suspension of particles

The laser beam impinges the sample with intensity I_0, interacts with the sample and then comes out with an intensity I_1. The process of attenuation of the incident beam involves both scattering and absorption phenomena. The cross section $\sigma_{ext}(\lambda_i, r)$ depends on the laser incident wavelength λ_i and on the radius of suspended particles r. Furthermore, the light attenuation process depends on the number of particles of radius r inside the scattering volume. This quantity is defined by

the particle density $n(r)$.
The relation between the transmitted intensity for a determined wavelength $T(\lambda_i)$ and the particle density $n(r)$ is obtained by dividing the optical path through the sample in slices of thickness dz. By intensity variation for each increment dz can be obtained by the following equation [2]

$$dI = -\sigma_{ext}(\lambda_i, r)n(r)Idz \tag{1.1}$$

where the minus sign is due to the decreasing intensity. Integrating the relation 1.1

$$\int_{I_0}^{I_1} \frac{dI}{I} = -\int_0^z dz\sigma_{ext}(\lambda_i, r)n(r) \tag{1.2}$$

we obtain the Beer-Lambert law

$$T(\lambda_i) = \frac{I_1(\lambda_i)}{I_0(\lambda_i)} = e^{-\sigma_{ext}(\lambda_i,r)n(r)z} \tag{1.3}$$

where $T(\lambda_i)$ is the transmittance at wavelength λ_i.
The equation 1.3 assumes a sample of suspended particles with identical radius (homogeneous sample). For a non-homogeneous sample, i.e. particles of different sizes, $T(\lambda_i)$ is the product of the transmittances for each "class" of particles grouped by different radius r_j and density n_j. Therefore, for each wavelength λ_i we have

$$T(\lambda_i) = \prod_{j=1}^{N} T(\lambda_i, r_j) = e^{-\sum_{j=1}^{N} \sigma_{ext}(\lambda_i,r_j)n_j z} \tag{1.4}$$

Employing the logarithm we obtain the effective sample extinction coefficient

$$\alpha_{ext} = -\frac{\ln T(\lambda_i)}{z} = \sum_{j=1}^{N} \sigma_{ext}(\lambda_i, r_j)n_j \tag{1.5}$$

The relation 1.5 connects in a simple way the measured laser transmission as a function of wavelength $T(\lambda_i)$ with the density of particles n_j of radius r_j. Therefore, to obtain the density distribution of particles as a function of size $n(r_j)$, we have to

- calculate the extinction matrix $\sigma_{ext}(\lambda_i, r_j)$
- invert the linear equations system $\alpha_{ext} = \sum_{i=1}^{N} \sigma_{ext}(\lambda_i, r_j)n_j$

In next sections we will explain these two problems in detail.

1.2 Scattering by spherical particles: Mie theory

In order to calculate the extinction matrix, we can use the Mie theory that allows to obtain a complete analytical solution for the scattering of an electromagnetic radiation from homogeneous spherical particles. The Mie theory moves by Maxwell equations to calculate a solution that takes into account the structural and symmetry properties of the system.

Following the reference [3] for the Mie theory it is useful to define the Maxwell equations as

$$\vec{\nabla} \times \vec{H} = \frac{4\pi\vec{J}}{c} + \frac{1}{c}\frac{d\vec{D}}{dt} \tag{1.6}$$

$$\vec{\nabla} \times \vec{E} = -\frac{1}{c}\frac{d\vec{H}}{dt} \tag{1.7}$$

$$\vec{\nabla} \cdot \vec{D} = 4\pi\rho \tag{1.8}$$

$$\vec{\nabla} \cdot \vec{H} = 0 \tag{1.9}$$

with the addition of charge conservation equation [1]

$$\vec{\nabla} \cdot \vec{J} + \frac{d\rho}{dt} = 0 \tag{1.10}$$

where $\vec{J}$ and ρ are the current and charge densities, resepectively. Writing the Fourier components for the electric and magnetic fields in complex forms,

$$\vec{E} = \vec{E}_0 e^{i\omega t} \tag{1.11}$$

$$\vec{H} = \vec{H}_0 e^{i\omega t} \tag{1.12}$$

defining the propagation constant in vacuum (i.e. the wavevector of the electromagnetic radiation) as

$$k = \frac{\omega}{c} = \frac{2\pi}{\lambda_0} \tag{1.13}$$

and the complex refractive index of medium in terms of the dielectric constant ϵ and conductivity σ,

$$m^2 = \epsilon - \frac{4\pi i\sigma}{\omega} \tag{1.14}$$

The Maxwell equations do result:

$$\vec{\nabla} \times \vec{H} = ikm^2\vec{E} \tag{1.15}$$

$$\vec{\nabla} \times \vec{E} = -ik\vec{H} \tag{1.16}$$

From this, a relevant result is represented by the possibility to decoupling the Maxwell equations. By applying the curl operator to equation 1.15 and using the following relation,

$$\vec{A} \times (\vec{B} \times \vec{C}) = (\vec{B} \times \vec{C}) \times \vec{A} = \vec{B}(\vec{A} \cdot \vec{C}) - \vec{C}(\vec{A} \cdot \vec{B}) \tag{1.17}$$

we can write

$$\nabla(\nabla \cdot \vec{H}) - (\nabla \cdot \nabla)\vec{H} = ikm^2(-ik\vec{H}) \tag{1.18}$$

and, using relation 1.9, we obtain

$$\nabla^2\vec{H} = -k^2m^2\vec{H} \tag{1.19}$$

The same procedure can be applied for the electric field $\vec{E}$

$$\nabla^2\vec{E} = -k^2m^2\vec{E} \tag{1.20}$$

[1] For completeness of information we report also the relation between the electric field in medium and in vacuum $\vec{D} = \epsilon\vec{E}$

where in this case is assumed the absence of charge, i.e. $\rho = 0$. In conclusion, from the electromagnetic theory both the fields are solution of the wave equation

$$\nabla^2 \vec{\Psi} = -k^2 m^2 \vec{\Psi} \tag{1.21}$$

The electric and magnetic fields are mutually perpendicular. Moreover, in the free space (as the case of the transmission measurements) one solution is a plane electromagnetic wave. For the measurements purposes, we neglect the Gaussian beam behaviour of the laser beam used for the experiments therefore, the fields can be represented as plane waves

$$\Psi = e^{i(km)z + i\omega t} \tag{1.22}$$

with a propagation constant in the medium $(k \cdot m)$.

Boundary conditions

We consider two isotropic and homogeneus media divided by a sharp surface as shown in figure 1.2, characterised by the costants ϵ_1,σ_1,m_1 and ϵ_2,σ_2,m_2 (where ϵ and σ are the dielectric constant and conductivity respectively, and m is the refractive index). If we define $\hat{n}$ as the unit vector normal to the interface between the two

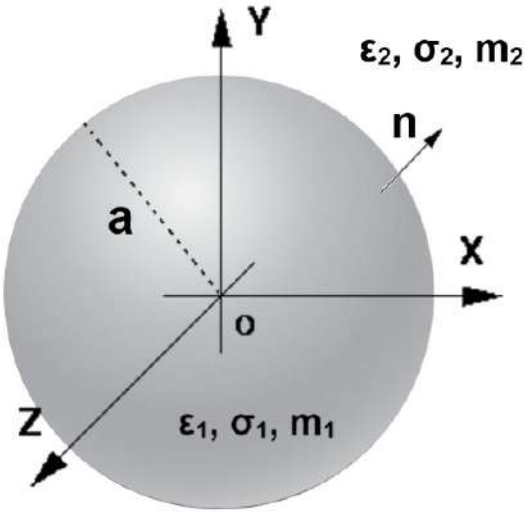

FIGURE 1.2: Sketch of a homogeneous sphere with radius a, refractive index m_1, the real part of dielectric constant ϵ_1 and conductivity σ_1, in a medium of refractive index m_2, the real part of dielectric constant ϵ_2 and conductivity σ_2. The vector $\hat{n}$ is a unit vector normal to the surface of the sphere.

media, directed into medium 2, the field components tangential to surface verify the

following relations

$$\hat{n} \times (\vec{H}_2 - \vec{H}_1) = 0 \tag{1.23}$$
$$\hat{n} \times (\vec{E}_2 - \vec{E}_1) = 0 \tag{1.24}$$

The boundary conditions for the normal components are given by

$$\hat{n} \cdot (\vec{H}_2 - \vec{H}_1) = 0 \tag{1.25}$$
$$\hat{n} \times ({m_2}^2 \vec{E}_2 - {m_1}^2 \vec{E}_1) = 0 \tag{1.26}$$

The set of equations must be completed by adding the boundary conditions on the surface charge. Defining δ as the surface charge density and J_i the surface current densities at the interface between two media, the equation 1.10 becomes

$$\hat{n} \cdot (\vec{J}_2 - \vec{J}_1) + \frac{d\delta}{dt} = 0 \tag{1.27}$$

which, combined with equation 1.26, gives the following relation

$$\hat{n} \cdot (\epsilon_2 \vec{E}_2 - \epsilon_1 \vec{E}_1) = 4\pi\delta \tag{1.28}$$

If we consider two non absorbing media, the refractive indices m_2 e m_1 are real and finite, implying null surface charge density and null surface current. For this reason, to obtain the solution, only the field boundary conditions are applied. For a discussion of the case of metallic particles, see the reference [3].

Wave equation solution in spherical wave functions

Since we are interested to study the scattering process from spherical particles, we write the previous equations in spherical coordinates to fully exploit the advantage to use this symmetry. For simplicity, in the following calculations we will indicate with m the particle refractive index ($m = m_1$) and we will assume the external medium as vacuum ($m_2 = 1$).

Since spherical waves are a complete orthonormal system of functions, it is possible to expand the plane waves, solutions of the equations (1.19, 1.20), in terms of spherical waves.
First of all, using spherical coordinates

$$\vec{r} = [rcos\phi sin\theta, rsin\phi sin\theta, rcos\theta] \tag{1.29}$$

the solutions of the scalar wave equation

$$\delta\Psi = -k^2 m^2 \Psi \tag{1.30}$$

can be expressed as linear combination of such elementary solutions

$$\Psi_{ln} = cos[l\phi] {P_n}^l(cos\theta) Z_n(mkr) \tag{1.31}$$
$$\Psi_{ln} = sin[l\phi] {P_n}^l(cos\theta) Z_n(mkr) \tag{1.32}$$

Here, n and l are integers that follow the relation $n \geq l \geq 0$, ${P_n}^l$ are the associated Legendre polynomials and Z_n are the spherical Bessel functions

$$ {P_n}^l(x) = (1-x^2)^{\frac{n}{2}} \frac{d^n}{dx^n} P_l(x) \tag{1.33} $$

$$ Z_n(x) = \sqrt{\frac{\pi}{2x}} Z_{n+\frac{1}{2}}(x) \tag{1.34} $$

The wave functions are in scalar form, whereas equations of our interest (1.19, 1.20) are in vectorial form. Elementary solutions of our vectorial equations can be found bearing in mind that if Ψ is the solution of the scalar wave equation, then the fields $\vec{M}$ and $\vec{N}$ defined by the following relations

$$ \begin{aligned} \vec{M}_\Psi &= \Delta \times (\vec{r}\Psi) \\ mk\vec{N}_\Psi &= \Delta \times (\vec{M}_\Psi) \\ mk\vec{M}_\Psi &= \Delta \times (\vec{N}_\Psi) \end{aligned} \tag{1.35} $$

are solutions of the corresponding vectorial wave equation.
Writing the fields in spherical coordinates,

$$ \vec{M} = (M_r, M_\theta, M_\phi) = \left(0, \frac{1}{rsin\theta}\frac{\delta(r\Psi)}{\delta\theta}, \frac{1}{r}\frac{\delta(r\Psi)}{\delta\theta}\right) \tag{1.36} $$

$$ \vec{N} = (N_r, N_\theta, N_\phi) = \left(\frac{\delta^2(r\Psi)}{\delta r^2}, \frac{1}{r}\frac{\delta^2(r\Psi)}{\delta r\delta\theta}, rsin\theta\frac{\delta^2(r\Psi)}{\delta r\delta\phi}\right) \tag{1.37} $$

if u and v are two solutions of the scalar wave equation, it is possible to express the electric and magnetic fields in terms of $\vec{M}$ and $\vec{N}$ fields using the following expressions

$$ \vec{E} = \vec{M}_v + i\vec{N}_u \tag{1.38} $$

$$ \vec{H} = m(-\vec{M}_u + i\vec{N}_v) \tag{1.39} $$

The solution to the problem is thus reduced to search scalar functions u and v.

Considering the scattering from a homogeneous sphere, we set the origin at the center of the sphere, the positive z-axis along the propagation direction of the incident wave and the x-axis in the plane of electric oscillations of the linearly polarized incident wave.
We can write the incident wave components as

$$ \vec{E} = \hat{a}_x e^{-ikz+i\omega t} \tag{1.40} $$

$$ \vec{H} = \hat{a}_y e^{-ikz+i\omega t} \tag{1.41} $$

where $\hat{a}_x$ and $\hat{a}_y$ are the unit vectors along x and y directions.

As discussed above, the incident waves in scalar form can be written as

$$ u^i = e^{i\omega t} cos\phi \sum_{n=1}^{\infty} (-i)^n \frac{2n+1}{n(n+1)} {P_n}^1(cos\theta) j_n(kr) \tag{1.42} $$

$$ v^i = e^{i\omega t} sin\phi \sum_{n=1}^{\infty} (-i)^n \frac{2n+1}{n(n+1)} {P_n}^1(cos\theta) j_n(kr) \tag{1.43} $$

where j_n are spherical Bessel functions of first kind.

A complete solution, outside the sphere, has the same form of the incident wave. Indeed, the field outside the sphere is the sum of the incident and the scattered wave. Therefore, the scalar wave functions are

$$u^s = e^{i\omega t} cos\phi \sum_{n=1}^{\infty} -a_n(-i)^n \frac{2n+1}{n(n+1)} P_n{}^1(cos\theta) h_n{}^{(2)}(kr) \tag{1.44}$$

$$v^s = e^{i\omega t} sin\phi \sum_{n=1}^{\infty} -b_n(-i)^n \frac{2n+1}{n(n+1)} P_n{}^1(cos\theta) h_n{}^{(2)}(kr) \tag{1.45}$$

where $h_n{}^{(2)}$ are the spherical Bessel functions of second kind.

The series above, as well as those for the incident wave, contain only simple solutions in terms of the Legendre polynomials of the first order P_n^1. The coefficients a_n and b_n have to be determined through the boundary conditions. The choice of the spherical Bessel functions of second kind $h_n{}^{(2)}$ is due to their asymptotic behaviour,

$$h_n{}^{(2)}(kr) \sim \frac{i^{n+1}}{kr} e^{-ikr} \tag{1.46}$$

which, combined with the factor $e^{i\omega t}$, gives an outgoing spherical wave, as required for the scattered wave.

Likewise, the waves propagating inside the sphere are given by the series

$$u^{sph} = e^{i\omega t} cos\phi \sum_{n=1}^{\infty} mc_n(-i)^n \frac{2n+1}{n(n+1)} P_n{}^1(cos\theta) j_n(mkr) \tag{1.47}$$

$$v^{sph} = e^{i\omega t} sin\phi \sum_{n=1}^{\infty} md_n(-i)^n \frac{2n+1}{n(n+1)} P_n{}^1(cos\theta) j_n(mkr) \tag{1.48}$$

where c_n and d_n are other two undetermined coefficients.

To obtain the analytical solution, the coefficients a_n, b_n, c_n, d_n must be calculated. We note that the field tangential components E_θ,E_ϕ,H_θ,H_ϕ, obtained combining equations 1.36, 1.37 with 1.38, 1.39, exclusively depend by

$$v, \qquad \frac{1}{m}\frac{\delta(ru)}{\delta r}, \qquad mu, \qquad \frac{\delta(rv)}{\delta r} \tag{1.49}$$

Since on the surface of the sphere ($r = a$, where a is the sphere radius) the field tangential components do not change, we can impose boundary conditions simply matching the functions u and v and their first derivatives.
To simplify the notation, we can introduce the Riccati-Bessel functions

$$\psi(z) = zj_n(z) = \left(\frac{\pi z}{2}\right)^{\frac{1}{2}} J_{n+\frac{1}{2}}(z) \tag{1.50}$$

$$\xi(z) = zh_n{}^{(2)}(z) = \left(\frac{\pi z}{2}\right)^{\frac{1}{2}} H_{n+\frac{1}{2}}{}^{(2)}(z) \tag{1.51}$$

and the dimensionless variables

$$x = ka = \frac{2\pi a}{\lambda} \tag{1.52}$$

$$\mu = mka \tag{1.53}$$

Using this notation, the boundary conditions are

$$\psi_n(x) - a_n\xi_n(x) = mc_n\psi_n(\mu) \tag{1.54}$$
$$\psi_n'(x) - a_n\xi_n'(x) = c_n\psi_n'(\mu) \tag{1.55}$$
$$\psi_n(x) - b_n\xi_n(x) = d_n\psi_n(\mu) \tag{1.56}$$
$$\psi_n'(x) - b_n\xi_n'(x) = md_n\psi_n'(\mu) \tag{1.57}$$

from which we derive the coefficients

$$a_n = \frac{\psi_n'(\mu)\psi_n(x) - m\psi_n(\mu)\psi_n'(x)}{\psi_n'(\mu)\xi_n(x) - m\psi_n(\mu)\xi_n'(x)} \tag{1.58}$$
$$b_n = \frac{m\psi_n'(\mu)\psi_n(x) - \psi_n(\mu)\psi_n'(x)}{m\psi_n'(\mu)\xi_n(x) - \psi_n(\mu)\xi_n'(x)} \tag{1.59}$$
$$c_n = \frac{\psi_n'(\mu)\xi_n(x) - \psi_n(\mu)\xi_n'(x)}{\psi_n'(\mu)\xi_n(x) - m\psi_n(\mu)\xi_n'(x)} \tag{1.60}$$
$$d_n = \frac{\psi_n'(\mu)\xi_n(x) - \psi_n(\mu)\xi_n'(x)}{m\psi_n'(\mu)\xi_n(x) - \psi_n(\mu)\xi_n'(x)} \tag{1.61}$$

These coefficients complete the analytical solution to the problem; the electric and magnetic fields can be expressed through analytical functions in each point of the space inside and outside the sphere. We, then, generalise the solution for particles suspended in a medium different from vacuum (for simplicity in the previous treaties we have assumed medium refractive index as 1). If we assume that the surrounding medium has real refractive index m_2 (not absorbing medium) and the spheres have refractive index m_1 (real or complex), we can generalise the solution by replacing the refractive index m (used above) with

$$m = \frac{m_1}{m_2} \tag{1.62}$$

and the wavelength in vacuum with

$$\lambda = \frac{\lambda_{vacuum}}{m_2} \tag{1.63}$$

and, consequently, the Mie parameter with

$$x = \frac{2\pi a}{\lambda} = \frac{2\pi a m_2}{\lambda_{vacuum}} \tag{1.64}$$

Using these parameters, all functions described before remain in the same form.
For our purpose, we are interested in solutions outside the sphere and therefore in the coefficients a_n and b_n.

1.2.1 Scattering by shelled spherical particles: Adan-Kerker theory

As for spherical particles with Mie theory, also for coated spheres it is possible to give a complete analytical solution for the scattering of electromagnetic radiation through the Adan-Kerker theory [4].
Differently from the case of homogeneous spheres (see figure 1.3) there are three propagation constants k_1, k_2, k_3 (and different refractive indices m_1, m_2 and m_3) for different materials of core, shell and external medium. We also have a radius a for the core and a radius b for the total sphere. From the formal point of view, the

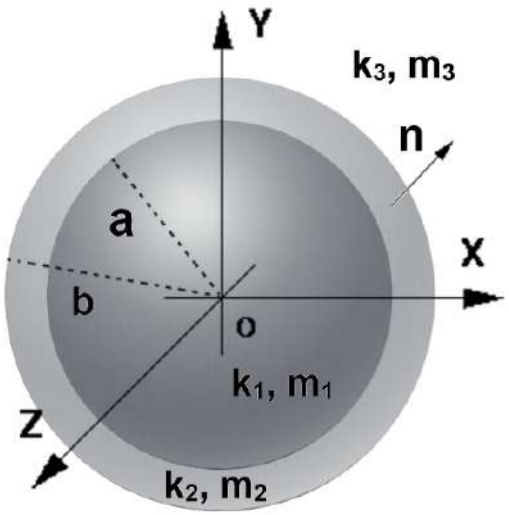

FIGURE 1.3: Sketch of a coated sphere with core radius a and shell radius b. k_1 and m_1, k_2 and m_2, and k_3 and m_3 are the propagation constants and the refractive indices for the core medium, the shell medium, and the external medium, respectively. The vector n is a unit vector normal to the external surface of the coated sphere.

problem is analogous to that one of homogeneous spheres. In terms of scalar waves, the incident radiation is represented by

$$u^i = \frac{1}{k_3} e^{i\omega t} cos\phi \sum_{n=1}^{\infty} (-i)^n \frac{2n+1}{n(n+1)} {P_n}^1(cos\theta) j_n(k_3 r) \quad (1.65)$$

$$v^i = e^{i\omega t} sin\phi \sum_{n=1}^{\infty} (-i)^n \frac{2n+1}{n(n+1)} {P_n}^1(cos\theta) j_n(k_3 r) \quad (1.66)$$

the scattered wave in the external medium by

$$u^s = -\frac{1}{k_3} e^{i\omega t} cos\phi \sum_{n=1}^{\infty} (-i)^n \frac{2n+1}{n(n+1)} {P_n}^1(cos\theta) a_n {h_n}^{(2)}(k_3 r) \quad (1.67)$$

$$v^s = e^{i\omega t} sin\phi \sum_{n=1}^{\infty} (-i)^n \frac{2n+1}{n(n+1)} {P_n}^1(cos\theta) a_n {h_n}^{(2)}(k_3 r) \quad (1.68)$$

the wave in the shell by

$$u^{sh} = -\frac{1}{k_2} e^{i\omega t} cos\phi \sum_{n=1}^{\infty} (-i)^n \frac{2n+1}{n(n+1)} {P_n}^1(cos\theta) [c_n j_n(k_3 r) + d_n n_n(k_3 r)] \quad (1.69)$$

$$v^{sh} = -e^{i\omega t} sin\phi \sum_{n=1}^{\infty} (-i)^n \frac{2n+1}{n(n+1)} {P_n}^1(cos\theta) [e_n j_n(k_2 r) + f_n n_n(k_2 r)] \quad (1.70)$$

where n_n are also Bessel funtions, and wave in the core by

$$u^{co} = -\frac{1}{k_1} e^{i\omega t} cos\phi \sum_{n=1}^{\infty} (-i)^n \frac{2n+1}{n(n+1)} P_n{}^1(cos\theta) g_n j_n(k_1 r) \tag{1.71}$$

$$v^{co} = -e^{i\omega t} sin\phi \sum_{n=1}^{\infty} (-i)^n \frac{2n+1}{n(n+1)} P_n{}^1(cos\theta) h_n j_n(k_1 r) \tag{1.72}$$

Also in this case, to calculate a_n, b_n, c_n, d_n, e_n, f_n, g_n, h_n coefficients, we impose boundary conditions simply matching the wave equations and their first derivates at $r = a$ (i.e. the interface between core and shell) and at $r = b$ (i.e. the interface between the shell and the external medium). Introducing the Riccati-Bessel funtions already described before (see equations 1.50,1.51) combined with

$$\chi(z) = -z n_n(z) = -\left(\frac{\pi z}{2}\right)^{\frac{1}{2}} N_{n+\frac{1}{2}}(z) \tag{1.73}$$

the boundary conditions can be expressed as

$$\begin{aligned}
m_1 c_n \psi_n'(m_2 x) + m_1 d_n \chi_n'(m_2 x) - m_2 g_n \psi_n'(m_1 x) &= 0 \\
c_n \psi_n(m_2 x) + d_n \chi_n(m_2 x) - g_n \psi_n(m_1 x) &= 0 \\
c_n \psi_n'(m_2 y) + d_n \chi_n'(m_2 y) - m_2 a_n \xi_n'(y) &= -m_2 \psi_n'(y) \\
c_n \psi_n(m_2 y) + d_n \chi_n(m_2 y) - a_n \xi_n(y) &= -\psi_n(y) \\
e_n \psi_n'(m_2 x) + f_n \chi_n'(m_2 x) - h_n \psi_n'(m_1 x) &= 0 \\
m_1 e_n \psi_n(m_2 x) + m_1 f_n \chi_n(m_2 x) - m_2 h_n \psi_n(m_1 x) &= 0 \\
e_n \psi_n'(m_2 y) + f_n \chi_n'(m_2 y) - b_n \xi_n'(y) &= -\psi_n'(y) \\
e_n \psi_n(m_2 y) + f_n \chi_n(m_2 y) - m_2 b_n \xi_n(y) &= -m_2 \psi_n(y)
\end{aligned}$$

Here we have assumed a non-absorbing external medium and we defined the parametres $x = k_3 a = 2\pi a/\lambda$ and $y = k_3 b = 2\pi b/\lambda$, and the refractive index of the core $m_1 = k_1/k_3$ and of the shell $m_2 = k_2/k_3$ relative to the external medium. The above system of equations can be easily analytically solved but, for better readability, we report only the coefficients of our interest a_n and b_n.

$$a_n = \frac{\begin{vmatrix} m_1\psi_n'(m_2x) & m_1\chi_n'(m_2x) & -m_2\psi_n'(m_1x) & 0 \\ \psi_n(m_2x) & \chi_n(m_2x) & -\psi_n(m_1x) & 0 \\ \psi_n'(m_2y) & \chi_n'(m_2y) & 0 & -m_2\psi_n'(y) \\ \psi_n(m_2y) & \chi_n(m_2y) & 0 & -\psi_n(y) \end{vmatrix}}{\begin{vmatrix} m_1\psi_n'(m_2x) & m_1\chi_n'(m_2x) & -m_2\psi_n'(m_1x) & 0 \\ \psi_n(m_2x) & \chi_n(m_2x) & -\psi_n(m_1x) & 0 \\ \psi_n'(m_2y) & \chi_n'(m_2y) & 0 & -m_2\xi_n'(y) \\ \psi_n(m_2y) & \chi_n(m_2y) & 0 & -\xi_n(y) \end{vmatrix}} \tag{1.74}$$

$$b_n = \frac{\begin{vmatrix} \psi_n'(m_2x) & \chi_n'(m_2x) & -\psi_n'(m_1x) & 0 \\ m_1\psi_n(m_2x) & m_1\chi_n(m_2x) & -m_2\psi_n(m_1x) & 0 \\ \psi_n'(m_2y) & \chi_n'(m_2y) & 0 & -\psi_n'(y) \\ \psi_n(m_2y) & \chi_n(m_2y) & 0 & -m_2\psi_n(y) \end{vmatrix}}{\begin{vmatrix} \psi_n'(m_2x) & \chi_n'(m_2x) & -\psi_n'(m_1x) & 0 \\ m_1\psi_n(m_2x) & m_1\chi_n(m_2x) & -m_2\psi_n(m_1x) & 0 \\ \psi_n'(m_2y) & \chi_n'(m_2y) & 0 & -\xi_n'(y) \\ \psi_n(m_2y) & \chi_n(m_2y) & 0 & -m_2\xi_n(y) \end{vmatrix}} \tag{1.75}$$

1.3 Extinction cross section

From the previous calculations, it is now possible to calculate the extinction cross section σ_{ext}.

We consider asymptotic wave functions for the scattered radiation [3]. This process is equivalent to write the Bessel functions as ${h_n}^{(2)}(kr) \sim \frac{i^{n+1}}{kr} e^{-ikr}$.

The wave functions thus result

$$u = -\frac{i}{kr} e^{-ikr+i\omega t} cos\phi \sum_{n=1}^{\infty} \left[(-i)^n - a_n \frac{2n+1}{n(n+1)} {P_n}^1(cos\theta) \right] \tag{1.76}$$

$$v = -\frac{i}{kr} e^{-ikr+i\omega t} sin\phi \sum_{n=1}^{\infty} \left[(-i)^n - b_n \frac{2n+1}{n(n+1)} {P_n}^1(cos\theta) \right] \tag{1.77}$$

To simplify the notation we introduce the quantities

$$\pi_n(cos\theta) = \frac{1}{sin\theta} P_n^1(cos\theta) \tag{1.78}$$

$$\tau_n(cos\theta) = \frac{d}{d\theta} P_n^1(cos\theta) \tag{1.79}$$

The field tangential components (1.38, 1.39) become

$$E_\theta = H_\theta = -\frac{i}{kr} e^{-ikr+i\omega t} cos\phi S_2(\theta) \tag{1.80}$$

$$-E_\phi = H_\phi = -\frac{i}{kr} e^{-ikr+i\omega t} sin\phi S_1(\theta) \tag{1.81}$$

where $S_1(\theta)$ and $S_2(\theta)$ are the amplitude functions

$$S_1(\theta) = \sum_{n=1}^{\infty} \frac{2n+1}{n(n+1)} \left[a_n \pi_n(cos\theta) + b_n \tau_n(cos\theta)\right] \tag{1.82}$$

$$S_2(\theta) = \sum_{n=1}^{\infty} \frac{2n+1}{n(n+1)} \left[b_n \pi_n(cos\theta) + a_n \tau_n(cos\theta)\right] \tag{1.83}$$

directly related to the amplitude of the scattered electromagnetic radiation at a given angle.

Since we are interested to the trasmitted radiation, the angle of interest is $\theta = 0$, therefore

$$\pi_n(1) = \tau_n(1) = \frac{1}{2} n(n+1) \tag{1.84}$$

and

$$S_1(0) = S_2(0) = S(0) = \frac{1}{2} \sum_{n=1}^{\infty} (2n+1)(a_n + b_n) \tag{1.85}$$

Using the foundamental extinction formula, the extinction matrix σ_{ext} can be expressed as

$$\sigma_{ext} = \frac{4\pi}{k^2} \Re[S(0)] = \frac{2\pi}{k^2} \sum_{n=1}^{\infty} (2n+1) \Re(a_n + b_n) \tag{1.86}$$

1.4 The inversion problem and Tikhonov regularization

The most delicate problem of this treatment is that one related to the inversion of the equation 1.5, which its integral version is known as Fredholm integral.

$$\alpha_{ext} = \int_{r_i}^{r_f} \sigma_{ext}(\lambda, r) n(r) dr \tag{1.87}$$

Written in terms of operators, the linear system of equations 1.5 becomes

$$\bar{\alpha}_{ext} = \bar{\bar{\sigma}}_{ext} \cdot \bar{n} \tag{1.88}$$

This problem results ill-posed and overdeterminated, whereby it can not be solved analytically. Indeed, the inverse operator ${\bar{\bar{\sigma}}_{ext}}^{-1}$ exists but it is not continuous [5]. The experimental error of measured α_{ext} introduces multiple solutions, of which only some of them have physical meaning [6]. From LTS measurements we get a number of equations (corresponding of the number of wavelengths) that in general is larger than the number of unknowns (i.e. the number of the radii r_j of particles) to be reconstructed. This generates overdetermination, therefore if the simple matrix inversion was used to calculate the system, the solution obtained would be not unique and unstable. In other words it would be a non-physical solution.

To solve ill-posed problems, algorithms based on least squares are generally employed. This kind of algorithms are based on the minimization of the quantity

$$\|\bar{\bar{\sigma}}_{ext} \cdot \bar{n}' - \bar{\alpha}_{ext}\|^2 \tag{1.89}$$

so as to choose as solution the vector $\bar{n}'$ closest to the analytical solution provided by

$$\bar{n} = \bar{\alpha}_{ext} \cdot {\bar{\bar{\sigma}}_{ext}}^{-1} \tag{1.90}$$

In the case of the Fredholm integral, the solution is extremely sensitive to small perturbations and a classical least-squares algorithm fails to compute it. A possible method to calculate the solution was proposed by Tikhonov and it is known as Tikhonov regularization method [6, 7]. This is a least-squares method where the quantity to minimize is

$$\|\bar{\bar{\sigma}}_{ext} \cdot \bar{n} - \bar{\alpha}_{ext}\|^2 + \|\Lambda \bar{\bar{L}} \cdot \bar{n}\|^2 \tag{1.91}$$

The parameter Λ and the operator $\bar{\bar{L}}$, if properly chosen, permit to regularise the system and to select non-oscillatory solutions.
Tikhonov regularization is based on the general idea that the least deviation of the quantity $\bar{\bar{\sigma}}_{ext} \cdot \bar{n}$ by the measured vector $\bar{\alpha}_{ext}$ is stabilized through a non-negative functional $\Omega(\bar{n})$, defined on a subspace of the set of solutions as long as it is a metric space.
The approximate solution is calculated minimizing the quantity

$$\rho_A^2(\bar{\bar{\sigma}}_{ext} \cdot \bar{n}, \bar{\alpha}_{ext}) + \Lambda\Omega(\bar{n}) \tag{1.92}$$

where ρ_A is the metric of the space A of the measured extinction coefficients vector $\bar{\alpha}$. If $\bar{\bar{\sigma}}_{ext}$ is a linear operator and the spaces A, N of $\bar{\alpha}_{ext}$ and $\bar{n}$ are Hilbert spaces, regularization method is reduced to search the solution of the following equation

$$({\bar{\bar{\sigma}}_{ext}}^* \bar{\bar{\sigma}}_{ext} + \Lambda \bar{\bar{L}})\tilde{n}_a = \bar{\bar{\sigma}}^* \tilde{\alpha}_{ext} \tag{1.93}$$

where $\tilde{n}_a$ is the approximate solution and $\bar{\bar{L}}$ is the matrix representation of the operator Ω.
In the next section we introduce a possible method to estimate the regularization parameter Λ.

Estimation of the regularisation parameter

A possible method to estimate the regularisation parameter Λ is the so called Self-Consistente Method [8].
Considering the system

$$\bar{\alpha}_{ext} = \bar{\bar{\sigma}}_{ext} \cdot \bar{n} \tag{1.94}$$

the quantity to minimise is

$$\chi_a^2 = \sum_{i=1}^{N} ((\alpha_{ext})_i - (\bar{\bar{\sigma}}_{ext} \cdot \bar{n})_i)^2 + \Lambda |\bar{n}|^2 \tag{1.95}$$

The *Singular-Value-Decomposition* [9] allows us to decompose the matrix $\bar{\bar{\sigma}}_{ext}$ and write the estimated solution as

$$\bar{n}_\Lambda = \sum_{\nu=1}^{M} \frac{\lambda_\nu}{{\lambda_\nu}^2 + \Lambda} \bar{v}_\nu (\bar{u}_\nu \cdot \bar{\alpha}_{ext}) \tag{1.96}$$

where u_ν are the eigenvectors of the matrix $\bar{\bar{\sigma}}_{ext} {\bar{\bar{\sigma}}_{ext}}^T$, v_ν those ones of ${\bar{\bar{\sigma}}_{ext}}^T \bar{\bar{\sigma}}_{ext}$ and λ_ν are the square roots of the eigenvalues of ${\bar{\bar{\sigma}}_{ext}}^T \bar{\bar{\sigma}}_{ext}$. To take into account that $\bar{\alpha}_{ext}$ is a measurement with an experimental error, we introduce the quantity $\bar{\alpha}_\epsilon$ with components

$$\alpha_i^\epsilon = (\alpha_{ext})_i + \epsilon_i \eta_i \tag{1.97}$$

where η_i are Gaussian variables with mean equal to zero and variance δ_{ij}.
Therefore, it is possible to write the solution as

$$\bar{N}_\Lambda = \sum_{\nu=1}^{M} \frac{\lambda_\nu}{{\lambda_\nu}^2 + \Lambda} \bar{v}_\nu (\bar{u}_\nu \cdot \bar{\alpha}^\epsilon) \tag{1.98}$$

and define the expected error in terms of mean square root between the quantities defined by equations 1.96 and 1.98

$$\langle D_n(\Lambda) \rangle = \langle (\bar{n}_\Lambda - \bar{N}_\Lambda)^2 \rangle \tag{1.99}$$

The minimised quantity is chosen as the regularisation parameter

$$\frac{\delta}{\delta \Lambda} \langle D_n(\Lambda) \rangle = 0 \tag{1.100}$$

1.5 LTS.f analysis software

In the first part of this chapter we have analysed the theory behind the functioning of LTS. Two problems have to be solved computationally, one relating to the calculation of the extinction matrix $\sigma_{ext}(\lambda_i, r_j)$ and the other one to the inversion of the linear equations system $\alpha_{ext} = \sum_{i=1}^{N} \sigma_{ext}(\lambda_i, r_j) n_j$ (in continuous form in equation 1.87). We have seen that it is possible to calculate σ_{ext} for homogeneous spheres via Mie theory and for shelled spheres via Adan-Kerker theory. For the inversion problem we have analysed the Tikhonov theory that allows to solve the linear equations system and obtain physically meaningful distributions.
On this theoretical background, we have written a Fortran code, i.e. LTS.f, which calculates the particle density distribution by reading the measured extinction coefficient as a function of the wavelength of the impinging laser beam. Our code is based on the use of subroutines available in litereture for the σ_{ext} calculation, i.e. MIEV0.f [10] for homogeneous spheres, BHCOAT.f for the shelled spheres [11] and the FTIKREG.f program for the Fredholm integral solution [12]. In figure 1.4 is reported the flow chart of the LTS.f program, where the blocks relative to the three routines are highlighted with different color. In the following the details of the program are well explained.

1.5.1 MIEV0.f: extinction matrix for homogeneous spheres

In LTS code, we use MIEV0 subroutine to calculate the extinction matrix σ_{ext}. The algorithm of this routine is based on the Mie theory for homogeneous spherical particle scattering, discussed in the section 1.2.
MIEV0 is able to compute different quantities and, in particular, as explained in MIEV documentation [13], is able to calculate, among various things,

- the scattering and extinction efficiencies;
- the asymmetry factor;
- the forward and back-scattering amplitudes;

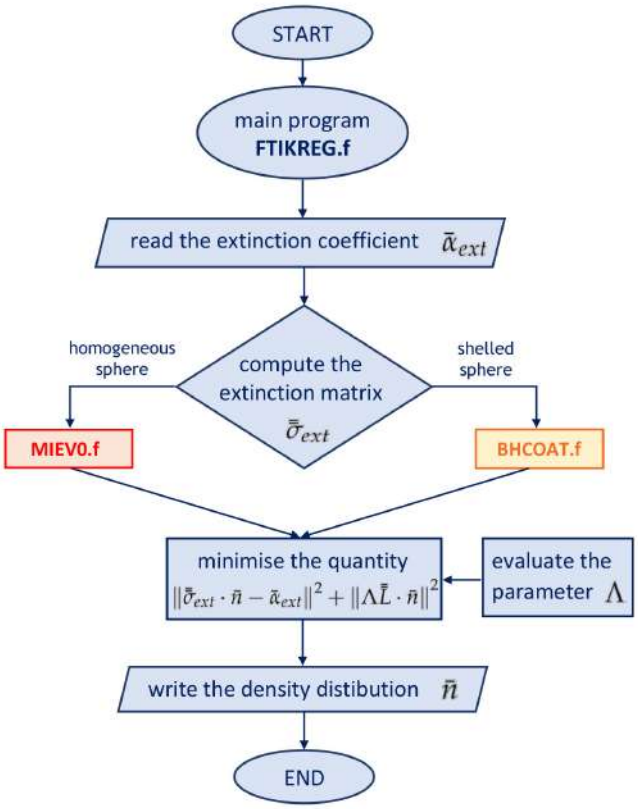

FIGURE 1.4: LTS.f flow chart: in blue are highlighted the blocks relative to FTIKREG.f, in red the ones relative to MIEV0.f, in orang the ones relative to BHCOAT.f.

- the scattering amplitudes vs. the scattering angle for incident polarisation parallel and perpendicular to the plane of scattering;
- the coefficients in the Legendre polynomial expansions of either the unpolarised phase function or the polarised phase matrix.

Our interest is focused on the extinction efficiency Q_{ext} (according to the notation of Bohren & Huffman [11]) because it is directly related to the extinction matrix

$$\sigma_{ext} = (\pi r^2) Q_{ext} \tag{1.101}$$

where r is the radius of homogeneous sphere.

In details, the subroutine requires eleven input variables and provides eleven outputs. In input, we have only two variables with physical meaning, i.e. the Mie parameter XX and the complex refractive index of the sphere $CREFIN$. These variables are defined in the main program LTS.f within a double cycle that allows to vary the radius of the sphere and the wavelength of the incident light.

Considering the presence of an external medium different from vacuum, we have preliminarly defined the dispersion relation $m(\lambda)$ (i.e., the complex refractive index as function of wavelength) of the materials outside the sphere beyond that one inside. In particular, for all the samples studied in this thesis, the external medium used is water and the associated dispersion relation is taken from literature [14]. For the sphere materials, indeed, we have used Polystyrene, Cellulose, Silver and Silica

```
      SUBROUTINE MIEV0( XX, CREFIN, PERFCT, MIMCUT, ANYANG,
     &     NUMANG, XMU, NMOM, IPOLZN, MOMDIM, PRNT, QEXT, QSCA,
     &     GQSC, PMOM, SFORW, SBACK, S1, S2, TFORW, TBACK, SPIKE )


       IMPLICIT  NONE

c ----------------------------------------------------------------------
c --------  I / O SPECIFICATIONS FOR SUBROUTINE MIEV0  -----------------
c ----------------------------------------------------------------------
       LOGICAL  ANYANG, PERFCT, PRNT(*)
       INTEGER  IPOLZN, MOMDIM, NUMANG, NMOM
       REAL*8     GQSC, MIMCUT, PMOM( 0:MOMDIM, * ), QEXT, QSCA, SPIKE,
     &         XMU(*), XX
       COMPLEX  CREFIN, SFORW, SBACK, S1(*), S2(*), TFORW(*), TBACK(*)
c ----------------------------------------------------------------------
...
```

FIGURE 1.5: MIEV0 subroutine heading as declared in LTS.f main program

with different dispersion relations, respectively from references [15, 16, 17].
Considering the cited dispersion relations and definitions 1.62 and 1.64, we have defined the two input paramenters as

$$XX = \frac{2\pi r RE}{\lambda} \tag{1.102}$$

$$CREFIN = \frac{R}{RE} + i\frac{C}{CE} \tag{1.103}$$

where RE and CE are the real and imaginary components of the external medium dispersion relation, while R and C are the correspective for the sphere material.
As to the output parameters, we are interested at the $QEXT$ value, which, through the relation 1.101, provides the extinction cross-section for a given sphere radius and a given wavelength.

1.5.2 BHCOAT.f: extinction matrix for shelled spheres

For shelled spheres extinction analysis, we have modified the first version of LTS.f program sobstituing MIEV0.f subroutine with BHCOAT.f.
In this case, the routine algorithm is based on Adan & Kerker theory [4] reported in section 1.2.1. BHCOAT subroutine has four input parameters XX, YY, $REFREL1$, $REFREL2$ and four output parameters $QQEXT$, $QQSCA$, $QBACK$, $GSCA$. All these parameters have physical meaning and, in particular, the input parameters are defined as

$$XX = \frac{2\pi r_{core} RE_{medium}}{\lambda} \tag{1.104}$$

$$YY = \frac{2\pi r_{shell} RE_{medium}}{\lambda} \tag{1.105}$$

$$REFREL1 = \frac{REF_{core}}{RE_{medium}} \tag{1.106}$$

$$REFREL2 = \frac{REF_{shell}}{RE_{medium}} \tag{1.107}$$

where r_{core} and r_{shell} are the radius of the core and shell, respectively, REF_{core} and REF_{shell} are the compex refractive indices of the core and shell, and RE_{medium} is the real part of the medium refractive index.
The two parameters XX and YY are the analogous of Mie parametres but for a sphere with the core radius and for another with the shell radius. The others parameters REF_{core} and REF_{shell} are the refractive indices of core and shell, relative to the medium.
The output parameters, instead, are the extinction and scattering efficiencies $QQEXT$ and $QQSCAT$, the backscattering efficiency $QBACK$ and a parameter that evaluates the cosine of the scattering angle $GSCA$.
Also in this case, we define the input parameters in the main program LTSshell.f, and compute XX and YY within a double cycle that varies the radius and the light incident wavelength. Actually, to simplify the algorithm, the shell radius r_{shell} is computed inside the cycle that varies the core radius r_{core} by the relation

$$r_{shell} = r_{core} + SHELL\_THICKNESS \tag{1.108}$$

where $SHELL\_THICKNESS$ is the thickness of the shell, which is screen required during the execution of main program.

As for the homogeneous sphere program, we are interested only at the extinction efficiency $QQEXT$ that allows us to calculate the extinction matrix through the relation 1.101.

1.5.3 FTIKREG.f: inversion of the equations system

The program FTIKREG.f developed by Jurgen Weese [12] allows us to calculate this solution using the Tikhonov regularisation.
In general, this program is written to extimate the function f in an extended version of the Fredholm integral of first kind

$$g(t) = \int_{s_{min}}^{s_{max}} K(t,s)f(s)ds + \sum_{j=1}^{m} a_j b_j(t) \tag{1.109}$$

Considering the errors $\sigma_1, ..., \sigma_n$ of the experimental data $g^{\sigma}(t_1), ..., g^{\sigma}(t_n)$, Tikhonov regularisation allows to obtain the function f by minimising the quantity

$$V(\Lambda) = \sum_{i=1}^{n} \frac{1}{\sigma_i^2} \left({g_i}^{\sigma} - \left(\int_{s_{min}}^{s_{max}} K(t_i,s)f(s)ds + \sum_{j=1}^{m} a_j b_j(t_i) \right) \right) + \Lambda \|Lf\|^2 \tag{1.110}$$

where L is the non-negative operator, i.e. usually the identity ($Lf = L$) or the first derivative ($Lf = f''$), and Λ is the regularisation parameter. Choosing a proper value for Λ, the first term on the right hand side of equation 1.110 forces the function f to be compatible with the experimental data whereas the second term drives the function f to be smooth, not-oscillating and not-divergent. To do this, FTIKREG.f program offers the possibility to estimate the optimal value of Λ by using the Self-Consistent method described above.

In LTS.f code we have adapted the FTIKREG main program to solve our problem 1.5. In particular, in the equation 1.110 we have imposed

$$\sum_{j=1}^{m} a_j b_j(t) = 0 \tag{1.111}$$

and defined the Kernel function as

$$K(t,s) = \sigma_{ext}(\lambda, r) \tag{1.112}$$

through the subroutines MIEV0 (homogeneous spheres) and BHCOAT (shelled spheres). Beyond that, we have defined as function $g(t)$ the extinction coefficient $\alpha(\lambda)$ and, consequently, the experimental input data and errors as the measured $\alpha^{\Delta\alpha}(\lambda_1), ..., \alpha^{\Delta\alpha}(\lambda_1)$ and $\Delta\alpha_1, ..., \Delta\alpha_n$. In such a way, the obtained solution function $f(s)$ from LTS.f is the particle distribution density $n(r)$.

The program FTIKREG (and conseguently the program LTS) reads both the input data and parameters by two ASCII files that in our case are called LTS.dat and LTS.par. After the computation, the program writes the estimated solution in a output file called LTS.sol (ASCII).
The data file (LTS.dat) must contain three numerical columns, because whichever non-numeric value cannot be read by the program. The first column must contain the wavelengths at which the extinction coefficients are maesured. The second and the third columns, instead, are reserved to the measured extinction coefficient values and the associated experimental errors respectively. In principle, the number of lines in this file, i.e. the number of experimental data, is not fixed and the only limit is rapresented by the size of the available memory of the computer.
The parametre file (LTS.par) must contain two columns (numerical values and name of parameters respectively) with 8 lines. In this file all the parameters nedeed by the program are defined, as shown in figure 1.6.

```
400             ns
320             smin
1200            smax
360             n
13              errmod
1               error
223             regmod
1e14            lambda
```

FIGURE 1.6: Example of parameters file read by LTS.f

The meaning of these parameters is explained in the following list:

- **ns (integer)**
  Number of points at which the density distribution $n(r)$ should be calculated ($2 \leq$ **ns** ≤ 7000)
- **smin (real)**
  Minimum radius at which the density distribution $n(r)$ should be calculated

- **smax (real)**
  Maximum radius at which the density distribution $n(r)$ should be calculated

- **n (integer)**
  Total number of data points (number of measured $\alpha(\lambda)$ in LTS.dat)

- **errmod (integer)**
  Type of data errors used for calculation. The parameter has two digits. The first digit determines if the error must be multiplied by a scaling factor defined by the parameter **error** (digit value equal to 1) or by a scaling factor calculated by the program (equal to 2). The second digit determines if the data errors (multiplied by the scaling factor) are read from LTS.dat (digit value equal to 1) or the data are assumed with an absolute error (equal to 2) or relative error (equal to 3)

- **error (real)**
  Error scaling factor. This value is used only if the first digit of **errmod** is equal to 1. For **errmod** $= 12$ or **errmod** $= 13$, this parameter is an extimation of the absolute or relative error, respectively

- **regmod (integer)**
  Choice parameter for the regularisation method. The parameter has three digits. The first determines whether in regularisation parameter calculation the constraints that the tails of the function $n(r)$ vanishes smoothly, must be considered (digit equal to 2) or not (equal to 1). The second digit determines if the regularisation parameter Λ is taken by the parameter **lambda** (digit equal to 1) or calculated through the SC-method (equal to 2). Finally, the third digit determines if the operator L is the identity $Ln = n$ (digit equal to 1), the second derivative $Ln = n''$ (equal to 2) or the second derivative with the previous contraints on the function $n(r)$ (equal to 3)

- **lambda (real)**
  Given value for the regularisation parameter Λ. This parameter is used only if the second digit of **regmod** is 1.

The output file LTS.sol contains **ns** lines. The results are written in four columns where the first one contains the radii r_j where the density distribution is reconstructed. The second and third columns, in our case, contain exactly the same values of the calculated $n(r_j)$, whereas the fourth column contains the errors associated to $n(r_j)$. The two identical columns in the output file are due to FTIKREG program, that allows to calculate two different set of data, with two different solutions. For the details we refer to the Weese user manual [18].

Chapter 2

Experimental setup and measurement technique

In the first chapter, we have seen how to obtain the density distribution function of a sample of suspended particles from the measure of the transmission coefficient at different wavelengths of the incident laser beam.
In this chapter, we present the experimental setup and the detection system developed for the transmission measurements. In particular, we report the particle transmission coefficient obtained from the measured transmitted laser intensities [1].

2.1 Experimental setup

Thanks to the advances both in light source technology and in detector performances, we have developed a relatively simple experimental setup for the measurement of the transmission coefficients in the wavelength range from 410 nm to 1100 nm, which is the range of interest for the characterisation of different samples (e.g. suspensions of nanoparticles and nanovesicles).
The scheme of the LTS setup is reported in figure 2.1. The setup can be ideally divided in four parts:

- light source (i.e. the tunable laser)
- optical components
- sample holder
- detection system

The principal component is a tunable laser that provides a pulsed light beam that is partially reflected by an optical window (only few percent of the emitted beam is reflected) to avoid both sample damage (particularly in biologial applications) and damage of the optical components. The laser intensity can be further reduced by neutral density filters. A mirror directs the beam on a broadband beamsplitter that splits it in two parts. Each one of the two resulting beams, focalised by a pair of lenses, passes simultaneously through the sample and reference channels, and is detected and analysed by the detection system, composed by two detectors and a lock-in amplifier. In the next sections, all the setup components are descibed in more details.

2.1.1 Light source

The light source is a Tunable Nd:YAG-Laser System mod. NT342B (Ekspla, Vilnius, LT)[19]. This laser system is tunable in the wavelength range from 410 nm

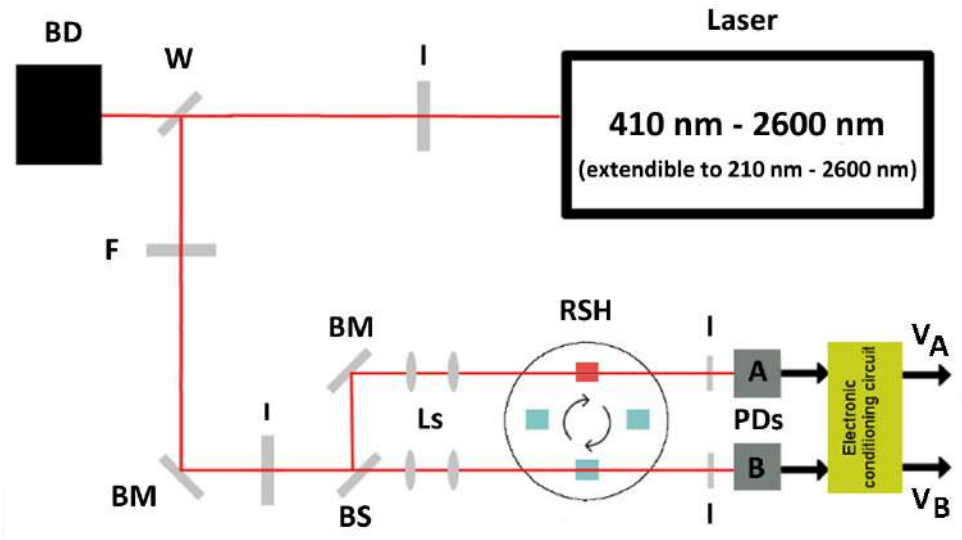

FIGURE 2.1: Scheme of the Laser Transmission Spectroscopy apparatus; the principal components are the tunable laser (Laser), the irises (I), the optical windows (W), the beam dumper (BD), the filters (F), the broadband fully reflecting mirrors (BM), the broadband 50/50 beam-splitter (BS), the lens collimating systems (Ls), the rotating sample holder (RSH), the Si photodetectors (PDs) and the electronic conditioning circuit. This electronic circuit provides two voltage pulses V_A and V_B proportional to the intensities of the incoming laser beam on the photodetectors A and B, respectively.

to 2600 *nm*, and can be upgraded with different tools to extend of the wavelength range in the UV region (down up to 210*nm*) [1]. It consists of a pulsed Nd-YAG laser generating a fundamental radiation at 1064 *nm*, which is converted into the second and third harmonics (at 532 *nm* and 355 *nm* respectively). The laser beam passes through an optical parametric oscillator (OPO), which generates the various output wavelengths through the rotation of two nonlinear crystals, generates the various wavelengths. The principal components of the NT342B laser are reported in figure 2.2. First of all, we focus on the Nd:YAG pump laser. The active medium material (Nd:YAG rod) is hosted in an unstable optical resonator with a concave rear mirror (99% of reflectivity) and a convex output variable reflectivity mirror. Inside the cavity, a polariser and a Pockels cell (forming the Q-switch system) are also present, which allows to provide the nanosecond laser pulses. As known, the Pockels cell consists of a crystal that becomes birefringent when an electric field is applied. This device permits to select a particular polarisation at certain voltage and, combined with the action of the external polariser, allows to fast switch the resonator cavity Q-factor. While the voltage is applied on Pockels cell,the Q-factor is very low, thus corresponding to very high intracavity losses. The Nd:YAG rod is pumped by a flash lamp to reach the maximum population inversion. When the maximum population inversion is reached, the voltage applied to the crysral drops fastly to zero allowing for the generation of laser pulses with a duration of about 5 *ns*, at a repetition rate of 10 *Hz*.
The generation of second (532 *nm*) and third (355 *nm*) harmonics is carried out by two nonlinear crystals of Potassium Dideuterium Phosphate of type II (DKDP-II).

[1] In September 2019, the wavelength extension was carried out and currently the laser is operating in the range between 210 *nm* and 2600 *nm*.

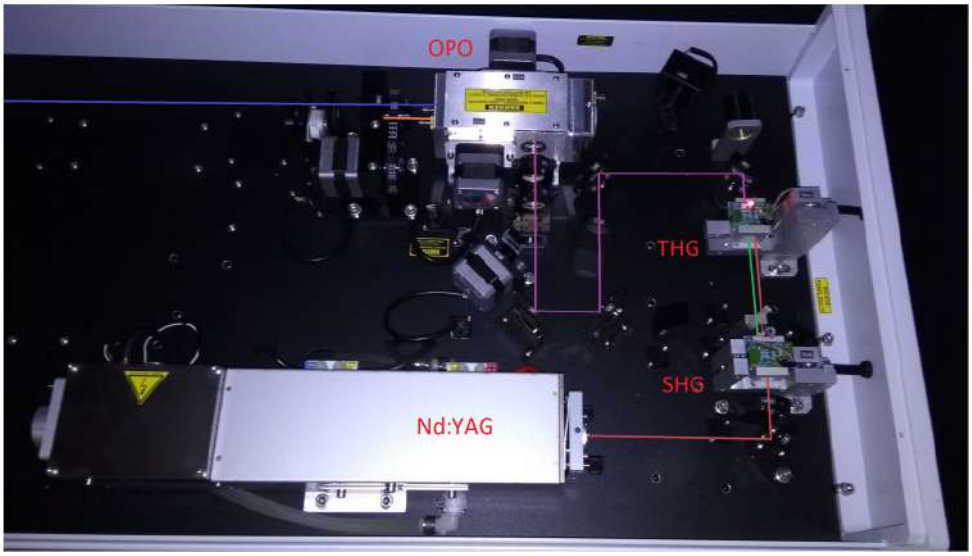

FIGURE 2.2: Picture of the principal components of the Nd:Yag tunable laser.

These crystals are positioned along the Nd:YAG beam optical path at fixed orientation, thus satisfying the phase matching conditions [20]. Since the angle at which the phase matching is achieved strongly depends on the crystal temperature, and the DKDP-II crystals are highly hygroscopic, they are mounted inside two ovens that mantain them at the constant temperature of $60 \pm 1°C$.
The harmonic radiation propagates collinearly to the fundamental beam, whereby, a dichroic mirror is employed to isolate the third harmonic required to activate the OPO. The generated pulses have a measured energy of $\simeq 96\ mJ$ at 355 nm.

The wavelength tunability is reached by the OPO. This device is based on the Optical Parametric Amplification process as described in reference [20], and, in our case, it employs two crystals of $\beta-$ Barium Borate of type II (BBO-II). The BBO crystals, pumped by the third harmonic, if suitably rotated (phase matching condition), generate a radiation with tunable wavelength in the range between 410 nm and 2600 nm. In particular, the process generates two waves, conventionally called Signal and Idler, with different frequency and polarisation, separated by an external Rochon prism to optimize the energy of the output laser pulses over the entire wavelength range. As an example, the measured output spectrum obtained with the OPO pumped by 4.2 ns laser pulses at 355 nm with an energy per pulse of 96 mJ, is reported in figure 2.3.

2.1.2 Optical components

To partially reflect the laser beam an uncoated N-BK7 glass window (Thorlabs, Newton, NJ - USA) is employed. This window has a thickness of 12 mm and a constant transmittance of about 92% in the range between 400 nm and 1800 nm. As reported in figure 2.4, the transmittance remains quite flat for wavelength values extended to the infrared, but rapidly decreases in the UV range [21]. This window is appropriate for our purpose since it reflects only a few percents of the intensity emitted by the laser source in the range of wavelength [410 nm;1100 nm].

Nevertheless, to avoid detector saturation, we have added neutral density filters of different Optical Density (OD) for the different wavelength range. Filters employed have OD between 0.5 to 3, which correspond to filtering factors of 68% and

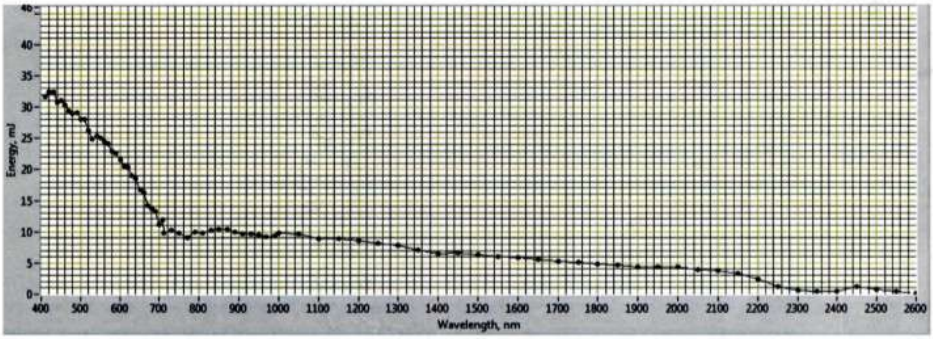

FIGURE 2.3: Output spectrum obtained with the OPO pumped by 4.2 ns laser pulses at 355 nm with an energy per pulse of 96 mJ.

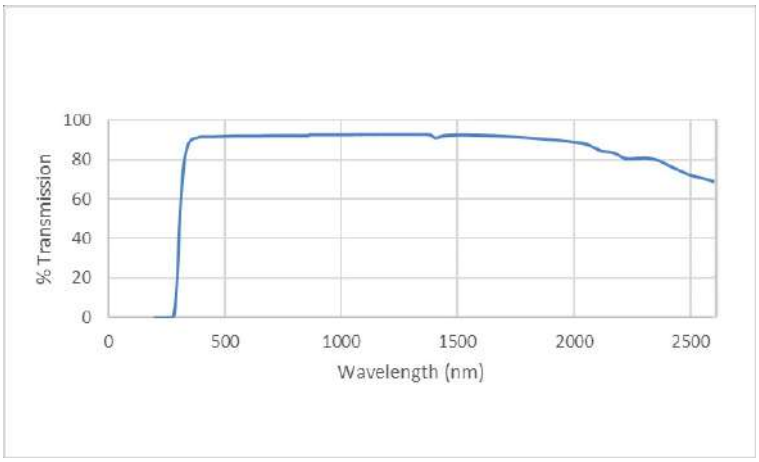

FIGURE 2.4: Trasmittance of a 10 mm thick sample of uncoated N-BK7 as reported by Thorlabs

99.9% respectively.

The used mirrors are Deep Ultra Violet Enhanced type (Edmund Optics, Barrington, NJ - USA), with a 25.4 mm diameter, consisting of a silicon substrate coated by enhanced aluminum film. These mirrors have a reflectivity higher than 85% in the 170 nm up to 11 μm range, so they are particularly suitable for our experimental purpose, also taking into account the extension to the ultraviolet frequencies (down to 210nm) of the laser source.

The beamsplitter is a 25.4 mm diameter Polka-Dot Beamsplitter (Edmund Optics, Barrington, NJ - USA) that nominally reflects and transmits the beam in a $\frac{50}{50}$ ratio. It consists of a silicon substrate covered by a pattern of aluminum with an overcoat of magnesium fluoride, with a center-to-center spacing of the coating square of 150 μm. Incident light is reflected by the coated area and transmitted through the surrounding uncoated substrate. Thanks to this reflection-transmission system, the beamsplitter covers a wide spectrum ranging from 200 nm to 2000 nm.
Due to the particular optical design, this beamsplitter generates a diffraction pattern. The typical diffraction pattern is shown in figure 2.5. This pattern changes according with the different wavelengths, introducing possible differencies in the laser pulse intensity incoming on the sample and reference channels. To avoid this kind of problems, the diffraction pattern in the two channels, shown in figure 2.1, is re-focalised

and suitably collimated in a quasi non diverging beam by two pairs of N-BK7 lenses positioned along the optical path.

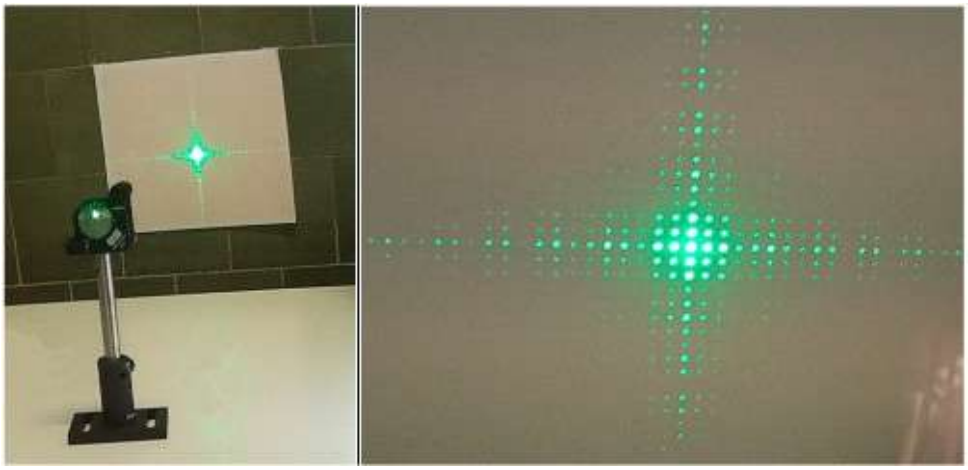

FIGURE 2.5: Diffraction pattern generated by the Edmund optics Polka-Dot Beamsplitter illuminated by a green laser emitting at 532 nm.

2.1.3 Sample holder

The sample holder is a Turret-400 model of Quantum North West company (Liberty Lake, WA - USA). This model (shown in figure 2.6) allows to control the sample temperature in a very precise way and to rotate four-position cuvette holder with high reproducibility. This second aspect is fundamental to our transmission coefficient measurements, as we explain in details in the following.
The Turret-400 contains a stepping motor drive for rapid position changes between four perpendicular positions. In each holder a standard square quartz cuvette (Hellma, Jena, DE) is host, with optical path of 10 mm and a transmittance up to 85% in the wavelength range between 200 nm and 2500 nm. Optiocal viewports are provided on 3 sides of each cuvette through 10 mm wide and 10 mm high apertures.

This turret is provided by a TC425 Temperature Controller: a microprocessor-based controller allows to change the four cuvette positions, to control the temperature (also programming temperature changes) and to activate the magnetic stirring. The operative temperature ranges between $-10°C$ to $+105°C$. Lower temperatures require additional insulation stages. A cooling water circuit, through a heat exchanger, allows to remove heat from the thermoelectric device (Peltier cell) when the temperature of the holder is lowered. The temperature of the heat exchanger is monitored and, if it exceeds a certain cutoff value, the temperature controller (TC425) is automatically shut down to protect the holder.
Temperatures lower than $-10°C$ require pre-cooled circulating fluid with a temperature within $25°C$ of the target temperature to draw heat from the Peltier device. The TC425 can control temperature down to $-55°C$, although about $-30°C$ is the limit under practical circumstances.
Turret-400 has a variable speed magnetic stirring for each cuvette and dry gas ports under each optical windows to minimise condensation on the cuvette surfaces.

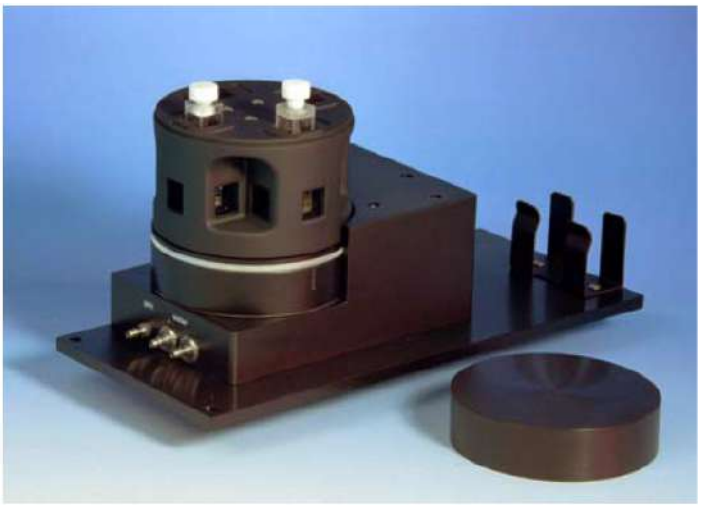

FIGURE 2.6: Termalized rotating sample holder Turret-400 of Quantum North West company (Liberty Lake, WA - USA) employed in LTS apparatus

2.1.4 Detection system

The Laser Transmission Spectroscopy is developed to evaluate both the concentration and dimension of nanoparticles (or nanovesicles) for biomedical and biophysical applications. Nowadays, the challenge is to investigate the role of nanovesicles in activating biological processes when their concentrations are less than $10^9 part/ml$ and their size ranges from few tens to few hundreds of nanometers. In such a situation, only slight variations of the transmitted laser intensities detected by photodiodes are expected, and the resulting minimum variations are mainly limited by the Signal-to-Noise Ratio (SNR). For this reason, the employed optoelectronic detection system is based on the use of the phase-sensitive synchronous demodulation technique carried out by a Lock-In Amplifier (LIA) that maximises the SNR also in the presence of very noisy conditions [22, 23, 24, 25, 26, 27].
In particular, in collaboration with the Department of Industrial and Information Engineering and Economics of the University of L'Aquila, an *ad hoc* LIA, optimized for our laser source, has been developed. Through this device, the signal detected by photodiodes is processed and amplified, and the output is a voltage signal proportional to the input intensity. The analog output signal is converted in a digital one by a Data Aquisition (DAQ) device (National Instruments, a Austi, TX - USA), and collected by a LabView programm that we developed.
In this section we describe the details of the detectors and lock-in amplifier.

Detectors

Although the laser source provides radiation in a wavelength range up to 2600 nm, for the study of suspensions of nanometric particles it is sufficient to measure the transmitted intensities below 1000 nm because the infrared radiation is almost totally transmitted with a negligible content of information.
Therefore, the detectors choosen for our setup are silicon detectors of Thorlabs (model DET10A2), operating in photoconductive mode, for light signals ranging in the $200nm$ to $1100nm$ wavelegth range. They have an active area of 0.8 mm^2, particularly useful to avoid the detection of radiation scattered by the particles at small angle. Indeed, in principle we need to collect the radiation transmitted at zero angle only.

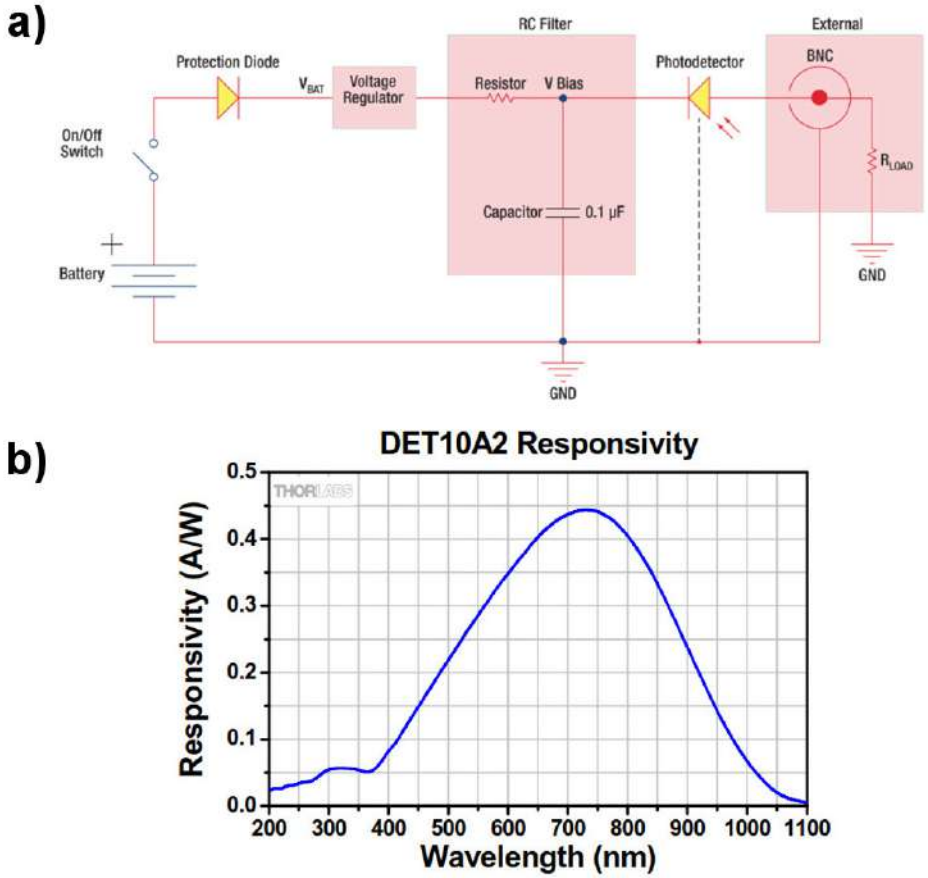

FIGURE 2.7: a) basic DET10A2 detector circuit: voltage regulator, RC filter and external components are highlighted by red squares; b) the DET10A2 responsivity in the wavelength range between 200nm and 1100nm.

The detectors operate according to the circuit depicted in figure 2.7a. The detectors are reverse biased [28] to produce a linear response with the applied input light. The circuit is powered by an A23 12V bias battery and is stabilised by a voltage regulator to obtain a bias voltage $V_{bias} = 10V$. The RC Filter cancels out any high frequency noise from the input supply, which may contribute to a noisy output.
The photocurrent generated is based upon the incident light and wavelength according to the responsivity defined as $R(\lambda) = \frac{I_{PD}}{P}$, where I_{PD} is the current generated by the photodiode and P is the power of incident light. In figure 2.7b, the DET10A2 responsivity is shown, as reported by Thorlabs.
The detectors are connected to the two channels lock-in amplifier by BNC cables, terminated by a load resistence $R_{load} = 50\ \Omega$. The output voltages, provided by the lock-in, thus result

$$V_A \propto \frac{I_A}{R_{load}} \tag{2.1}$$

$$V_B \propto \frac{I_B}{R_{load}} \tag{2.2}$$

where the proportionality is due to the gain factors introduced by the lock-in.

Lock-in amplifiers

The lock-in amplifier have two channels with tunable amplification (tunable gain) and operate at 10 Hz (i.e. at the same repetition rate of the laser) repetition rate and has been designed to measure input voltage signals with 10 ns pulse duration (i.e.the same duration of the laser pulses). These characteristics maximise the apparatus sensitivity and resolution with respect to the small amplitude variations of the input signal, which are related to the changes of intensity of the laser beam passing through the sample.

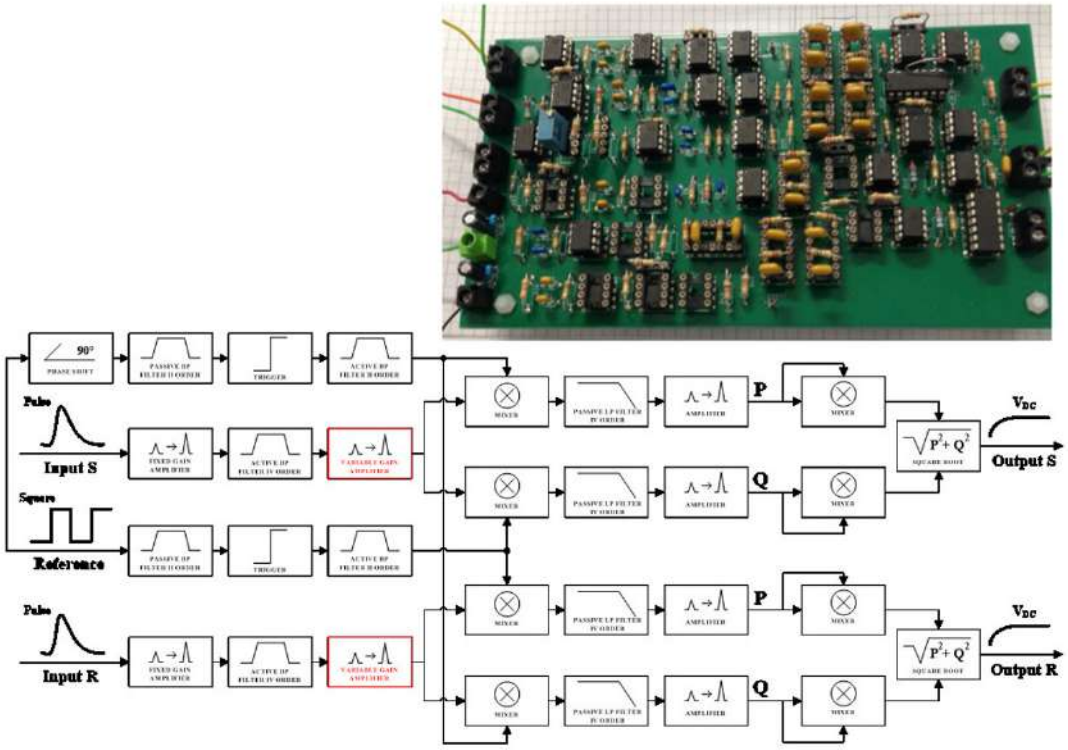

FIGURE 2.8: Block scheme of lock-in amplifier developed for our LTS apparatus; the inset show the fabricated Printed Circuit Board (PCB) implementing the proposed lock-in amplifier

To deeply understand how the LIA is designed, we consider the block scheme reported in figure 2.8. LIA main stages have been designed by employing standard circuit topologies and configurations for filters, triggers, phase-shifters and amplifiers [29, 30]. The other functions, namely the mixers and the square root operations, have been directly implemented by commercial active devices, as described in detail in the following. All the LIA internal blocks have been optimized to achieve the best enhancement of the detection sensitivity, resolution and SNR, measuring the small variations of the amplitude of short pulsed signals with a non-zero mean value. In particular, referring to the two input stages (i.e. the Input S and Input R paths), the fourth-order band-pass filter reduces the harmonic content of the input signal as well as the input noise bandwidth. Moreover, they remove the input disturbs and interferences and, extract and amplifies the main harmonic components of the input pulsed signal. It is based on a cascade of two active second-order multiple negative feedback inverting filters, centered at $f_0 = 10\ Hz$ with a quality factor $Q = 12.5$ (i.e., a bandwidth $BW = 0.8\ Hz$) and a maximum gain equal to 560. This block is combined with two amplifiers implemented with operational amplifiers (OA) in a

non-inverting configuration. The first one, the input stage of the LIA, provides a fixed gain equal to 11, while the second one is a variable gain stage whose amplification value can be properly tuned from 11 up to 271, through the regulation of an external resistor acting on the non-inverting amplifier topology. Furthermore, referring to the output stages, low-pass filters have been implemented to extract the DC components and regulate the system response time. They are based on a fourth-order passive topology composed by a cascade of four RC-cells whose resulting cut-off frequency f_t is about 10 mHz, much smaller than the LIA input pulsed signal repetition frequency $f_0 = 10\ Hz$ and its main harmonics. Moreover, additional amplifiers have been also included providing a further gain to the overall architecture thus strongly enhancing the overall LIA detection sensitivity and resolution. These stages have been implemented with OA in a non-inverting configuration having a fixed gain equal to 6 for all the branches of LIA. Finally, the phase shifter block is introduced to add a fixed 90° phase shift between the two paths of the reference signal (i.e., Phase P, and Quadrature Q), while the trigger blocks have been implemented through OA in an open-loop comparator configuration to square the signal.

Based on this scheme, a Printed Circuit Board (PCB) prototype of LIA, reported in figure 2.8, has been realised by using commercial discrete electronic components. In particular, the active components employed for the implementation of the different blocks composing LIA are AD711 BiFET high speed OA (Analog Devices, Norwood, MA - USA). The mixers are AD633 analog multipliers, while the square root has been implemented through AD734 high speed four-quadrant analog multiplier. All the OA and the other active components are powered at a dual DC voltage equal to $\pm 15\ V$.

2.2 Transmission coefficient measurement

The experimental apparatus described in the previous sections, allows to measure the radiation intensity transmitted through the sample.
From the theory (chapter 1) it is known that, to obtain the particle density distribution $n(r)$, we need to measure the extinction coefficient $\alpha_{ext}(\lambda$, which is given by the relation

$$\alpha_{ext}(\lambda) = \frac{-lnT(\lambda)}{z} \tag{2.3}$$

where T is the transmission coefficient.
Therefore, the experimental problem is reduced to find the appropriate method to obtain the particle transmission coefficient from the intensity measurements.
The LTS apparatus (figure 2.1) allows the simultaneous light intensity measurement on the sample and on the reference, i.e. the fluid in which the particles are suspened. This is sufficient to calculate the transmittance as the ratio of these two quantities.
On the contrary, the light intensities, as well as the corresponding voltages obtained by the lock-in amplifier, show differencies between the two measurment channels, due to the peculiar wavelength dependences of optic components and detectors sensitivity. In particular, in the case of the beamsplitter, the reflection-transmission coeffcients are not the same for all the considered wavelengths. Moreover the mirror, needed to reflect part of the splitted laser beam, introduces another asymmetry between the two beams. The detectors are not perfectly indentical since they have two different responsivity curves and the lock-in amplifier introduces a different gain on the two acquisition channels. Measured voltages as a function of wavelength of the

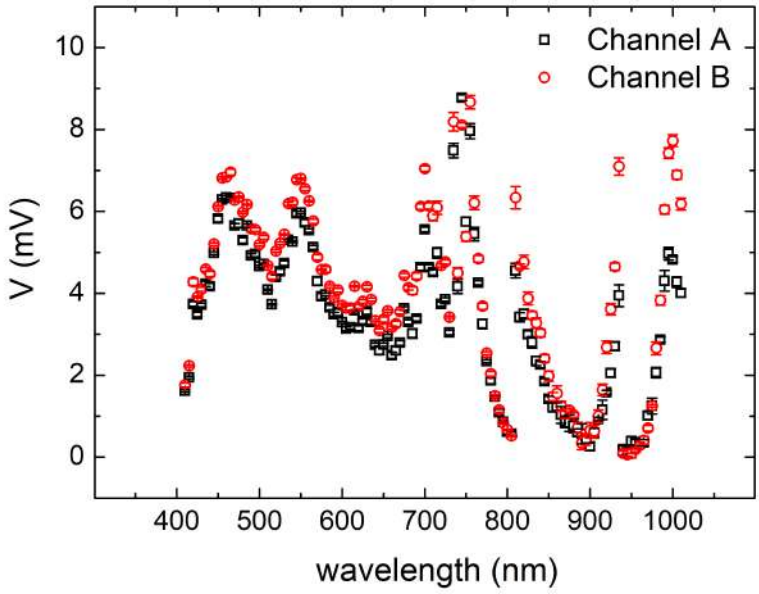

FIGURE 2.9: Measured voltages as a function of wavelength for the two channels in absence of sample and reference; light intensities variations have been limited by using neutral density filters, to keep the output voltage under the saturation limit of $10V$

two channels in absence of sample and reference, reported in figure 2.9, clearly show this behaviour.

To overcome this problem, it is possibile to collect the transmission spectra two times, by turning the Turret-400 to change the sample-reference order.
With this approach we measure four output voltage signals $V_{I,J}$ that are proportional to the laser beam intensity passing through the cuvettes and impinging on the detectors. The four voltage signals are

$V_{A,P}$ = the signal through the particle sample P measured by the detector A

$V_{B,F}$ = the signal through the suspending fluid F measured by the detector B

$V_{B,P}$ = the signal through the particle sample P measured by the detector B

$V_{A,F}$ = the signal through the suspending fluid F measured by the detector A

which, following the sketch shown in figure 2.10, can be defined as a function of wavelength by

$$\begin{aligned} V_{A,P}(\lambda_i) &= g_A \epsilon_A(\lambda_i) T_P(\lambda_i) T_F(\lambda_i) P_A(\lambda_i) \\ V_{B,F}(\lambda_i) &= g_B \epsilon_B(\lambda_i) T_F(\lambda_i) P_B(\lambda_i) \\ V_{B,P}(\lambda_i) &= g_B \epsilon_B(\lambda_i) T_P(\lambda_i) T_F(\lambda_i) P_B(\lambda_i) \\ V_{A,F}(\lambda_i) &= g_A \epsilon_A(\lambda_i) T_F(\lambda_i) P_A(\lambda_i) \end{aligned}$$

where P_I are the intensities of the two beams impinging on the cuvettes, T_I the transmission coefficients of the particles and suspending fluid, ϵ_I the sensitivity of the detectors and g_I the gains of the LIA channels.

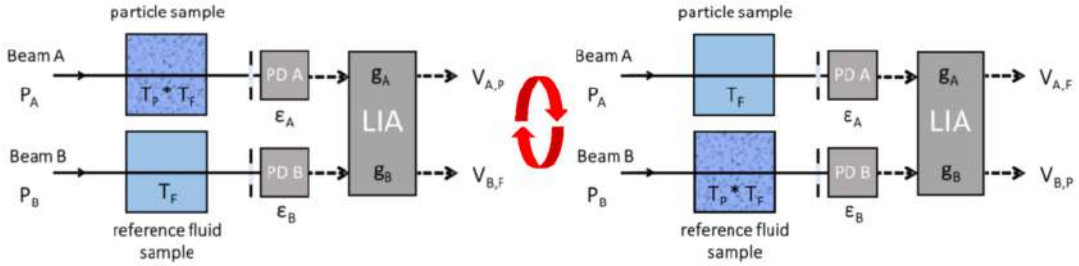

FIGURE 2.10: Sketch of measurement configuration: P_I are the intensities of two beams, T_I the transmission coefficients of particles and suspending fluid, ϵ_I the sensitivity of the detectors, g_I the gains of the two LIA channels and $V_{I,J}$ the output voltage signals.

Computing the product of ratio of the two pairs of voltage signals $V_{A,P}$, $V_{B,F}$ and $V_{B,P}$, $V_{A,F}$

$$\frac{V_{A,P}}{V_{B,F}} * \frac{V_{B,P}}{V_{A,F}} = \frac{g_A \epsilon_A(\lambda_i) T_P(\lambda_i) T_F(\lambda_i) P_A(\lambda_i)}{g_B \epsilon_B(\lambda_i) T_F(\lambda_i) P_B(\lambda_i)} * \frac{g_B \epsilon_B(\lambda_i) T_P(\lambda_i) T_F(\lambda_i) P_B(\lambda_i)}{g_A \epsilon_A(\lambda_i) T_F(\lambda_i) P_A(\lambda_i)} = T_P^2 \tag{2.4}$$

all the wavelength dependent contributions of the optics and detectors cancel out, and only the squared transmission of particles survives.
Consequently, despite the different lock-in channel gains g_A, g_B (which are canceled in the product of the two ratios), the particle transmission coefficient is given by

$$T(\lambda) = \sqrt{\frac{V_{A,P}(\lambda)}{V_{B,P}(\lambda)} * \frac{V_{B,P}(\lambda)}{V_{A,F}(\lambda)}} \tag{2.5}$$

Resuming, we have that measuring two times the intensities transmitted by sample and reference (changing their positions), it is possible to obtain the particle transmission coefficient, which analised with LTS.f program allows us to obtain the particle density distribution.

Chapter 3

LTS test measurements of standard samples

In order to verify the performances of our experimental setup, we measured the transmission coefficient of different standard samples, with different size and concentration. Here, we report the measurements and the computational analysis, which allow to determine the sensitivity of the apparatus and the error associated with the values of both the standard particles radius and concentration.

3.1 Uncertainity and sensitivity determination

To verify the performances of the LTS apparatus, we measured the size and concentration of a polystyrene particle acqueous suspension DUKE STANDARD by Thermo Scientific (Waltham, MA - USA). In particular, the sample used for these measurements has a nominal mean radius of 254 $nm \pm 4$ nm and a concentration of about 1×10^9 $particles$ per ml. All the characteristics of this sample are certified by the National Institute of Standard and Technology (NIST). The mean diameter is obtained from the distribution calculated by analysing the Transmission Electron Microscopy (TEM) images. The associated uncertainty is the standard deviation of the TEM distribution multiplied for a factor $k = 2$, to define an interval with a level of confidence of the 95%. In the following, we analyse the LTS results obtained for this standard sample and for two dilutions.

3.1.1 Comparison between the measured and nominal size and concentrations

In figure 3.1a we report the measured transmission coefficient in the wavelength range between 410 nm to 1010 nm. We collected 70 data points with a 10 nm wavelength spacing. Each point results from a double intensity measurement, as explained in section 2.2, and has an error bar obtained from the propagation of the measured intensity experimental error. The measured transmission function is quite smooth and continuous within the error bars of the experimental data, as expected for a non-absorbing sample. In the inset of figure 3.1a the respective extinction coefficient is reported. Notice that the error of the extinction coefficient is amplified by the error propagation. Because the LTS.f program analyses the extinction coefficient taking into account its associated error (see chapter 1), some problems in the analysis results can be expected.
Analysing these data we obtain the particle density distribution shown in figure 3.1b. The program builds the density distribution $n(r)$ as a histogram with a proper bin-width defined by the number and the interval of radii (see section 1.5). The

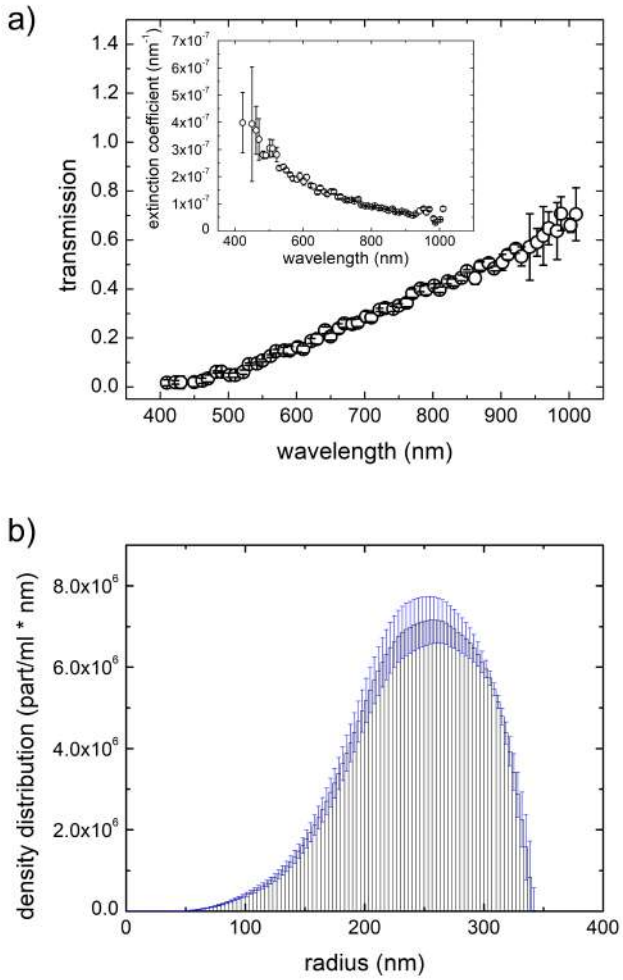

FIGURE 3.1: a) Transmission coefficient measured for a NIST polystyrene standard sample of nominal radius of 254 nm and nominal concentration of 1×10^9 $part/ml$. In the inset the respective extinction coefficient is shown. b) Particle density distribution obtained analysing the transmission coefficient with LTS.f program; the distribution is a histogram (in black) with an associated error for each bin (in blue).

height of each bin (i.e. the concentration of particle of the same radius) has an error bar (in blue in figure 3.1) calculated by the program by propagating the uncertainty of input data.
The first catching thing is the asymmetric shape and the broadening of the LTS distribution respect to the very narrow distribution provided by NIST (254 $nm \pm 4$ nm). This is certainly an artifact introduced by the program, which does not correctly reproduce the distribution, mainly due to the measurement uncertainty but, also, for the reduced measurement wavelength range. Indeed, in this wavelength window, we can only appreciate the tail of the scattering peak (dominant in the region below 400 nm) of the transmission coefficient, with a lower content of information. To reduce significantly the measurement uncetainity, we developed a new measurements method (see chapter 3) and, recently, extended the laser wavelength range down to 210 nm.
Despite the LTS distribution width is distorted, the obtained avarage particle radius

and the value of the sample concentration are in good agreement with those provided by the factory. In particular, to take into account the asimmetry of the distribution, we calculated the mean radius as the weighted average of the concentration of the different bins. This allowed us to obtain a mean radius of 258 nm.
As to the concentration, we calculated the discrete sum of the bin concentrations (i.e. using the rectangle rule for numerical integration). Through the propagation of the error of each bin, it is also possible to compute the error of the calculated sample concentration. We thus obtained the concentration of $1.03 \pm 0.09 \times 10^9$ $part/ml$ for the measured sample, in excellent agreement with the nominal value. This is of great importance because, while the radius can be measured with different other techniques, the absolute concentration measurements is the peculiar characteritics of the LTS tecnique.
To further validate the results, and also to estimate the uncertainity associated with the mean radius, we performed other measurements on the same sample (NIST standard polystyrene particle suspension, $r = 254 \pm 4$ nm and $C = 1 \times 10^9$ $part/ml$). The average radius and concentration from the analysis of the five performed measurements are reported in figure 3.2. The measured radii (back squares) are reported in figure 3.2a with the avarage value 252 ± 13 nm (in blue), where the error bar represent the 95% confidence interval. All the measured average radii are in accordance with the nominal ones, and, as shown in figure 3.2b, contained under the 6% of variation from the expected value. We can assume this relative variation as the relative error associated to measured radius.
We obtain analogous results also for the concetrations, as shown in figures 3.2c and 3.2d. The average value of the five concetrations is equal to $1.0 \pm 0.1 \times 10^9$ $part/ml$ with a relative variation of the measured concentration of about 10%. This result confirms what has been obtained for the single measurement, and allows to consider the value calculated from the error propagation as a good estimate of the concentration error.

3.1.2 Concentration sensitivity

Starting from the results obtained for the NIST sample at 1×10^9 $part/ml$ concentration, we measured also other diluted samples to check the sensitivity of our LTS apparatus.
In particular, we prepared two samples diluting 100 μl and 10 μl of NIST 10^9 $part/ml$ in 900 μl and 990 μl of distilled water, respectively. These dilutions have been carried out using pipets of PIPETMAN L series by Gilson (Middeleton, WI - USA), which guarantee a systematic error below the 0.8%.
The measured transmission coefficients for the two diluted samples are reported in figure 3.3, together with that one measured for the previous sample ($C = 1 \times 10^9$ $part/ml$). Decreasing the particle concentration, the transmission coefficient approach to 1, in the measurement wavelength window.
Nevertheless, we analysed the transmission data and the resulting particle density distributions to provide the particle concentrations and radii as reported in figure 3.4. The measured concentration values as a function of nominal values were fitted with a linear function with the constrain of the intercept equal to zero. As expected, the slope resulting from the fitting procedure is 1.00 ± 0.03. The data show a perfect matching with the fitting line for the values of the nominal concentrations of 1×10^9 $part/ml$ and 1×10^8 $part/ml$. Only the value obtained at low concentration shows some differences and bigger uncertainty ($2.4 \pm 0.5 \times 10^7$ $part/ml$). This may be related to a transmission coefficient very close to 1 that is associated to a very low

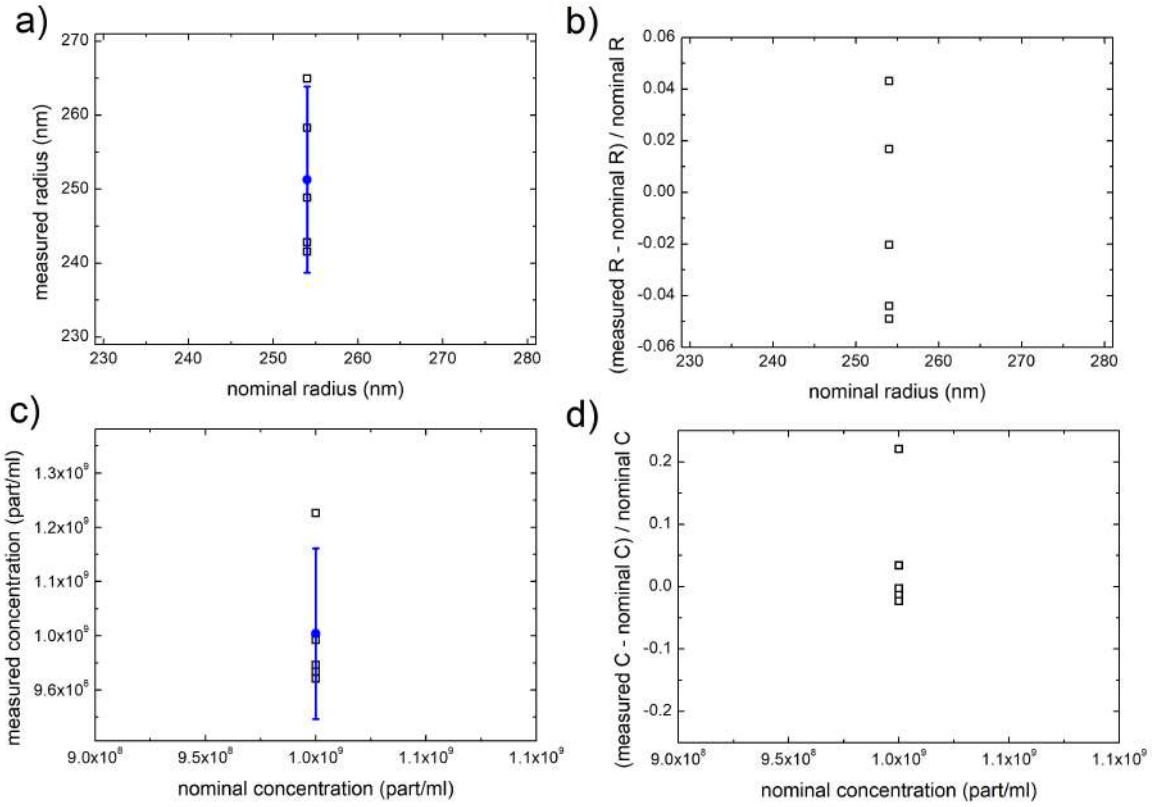

FIGURE 3.2: a) Particle radius as obtained from five measurements of NIST polystyrene standard sample ($R_{nominal} = 254\ nm$, $C_{nominal} = 1 \times 10^9\ part/ml$; the mean value is reported in blue with the associated error bar (95% confidence interval). b) Relative variation between the measured and the nominal radius for the five measurements. c) Particle concentration as obtained from five measurements of NIST polystyrene standard sample ($R_{nominal} = 254\ nm$, $C_{nominal} = 1 \times 10^9\ part/ml$; the mean value is reported in blue with the associated error bar (95% confidence interval). d) Relative variation between the measured and the nominal concentration for the five measurements.

content of information. For semplicity, the results are reported in log-log scale in figure 3.4a.
The particle radii obtained by the analysis are in accordance with the nominal value within the error (figure 3.4b), and the average value (reported in blue) is of $260 \pm 10\ nm$. From the results discussed above, particle suspension with concentrations lower than $10^7\ part/ml$ cannot be measured in the wavelength region allowed by the employed laser source. In this regards, the palanned extension in the ultraviolet region will permit to measure sample at lower concentrations and with smaller size. Therefore, we can assume this concentration ($10^7\ part/ml$) as the sensitivity limit of our LTS apparatus.

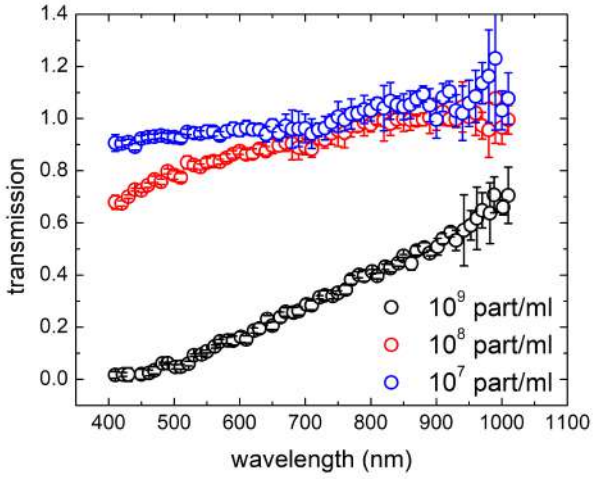

FIGURE 3.3: Transmission coefficients measured for a NIST polystyrene standard sample of nominal radius of 254 nm and nominal concentrations of 1×10^9 $part/ml$, 1×10^8 $part/ml$, 1×10^7 $part/ml$

3.2 Comparison with other techniques: measurements on different samples

Moving from the results obtained for the NIST standard sample, we studied other samples of polystyrene and silver, at different size and concentration.
To further validate the performances of the LTS technique, we performed Scanning Electron Microscopy (SEM) and Dynamic Light Scattering (DLS) measurements. These two techniques are considered as reference for the particle size analysis, even if they are limited by several problems and they do not give information on the absolute sample concentrations. As known, indeed, the SEM technique requires the sample deposited on a conductive substrate, a measurement performed under vacuum and, finally, provides results with poor statistic. The DLS technique, despite be non-invasive with good statistic, furnishes the size distribution in terms of hydrodynamic radius, which generally over-estimates the real radius. More details on SEM and DLS techniques are discussed in appendix B.
Nevertheless, the comparison between SEM, DLS and LTS results allowed us to verify the size resolution performances.
In this section, we report the results obtained from LTS, DLS and SEM measurements for different polystyrene samples in a wide range of radii, from a few tens of nanometers up to a micrometers. We also report the LTS measurements for a sample of silver particles of 50 nm of radius, in order to compare the results from different materials.

3.2.1 Polystyrene samples of different size and concentration

First of all, we show the results obtained for a polystyrene sample with nominal radius of 50 nm (Sigma-Aldrich, St. Louis, MO - USA). In figure 3.5a is reported the normalised density distributions provided by the three techniques. The LTS analysis provided a density distribution with a mean radius of 54 nm and a Full Width Half Maximum (FWHM) of 20 nm, which is visibly asymmetric towards smaller radii.

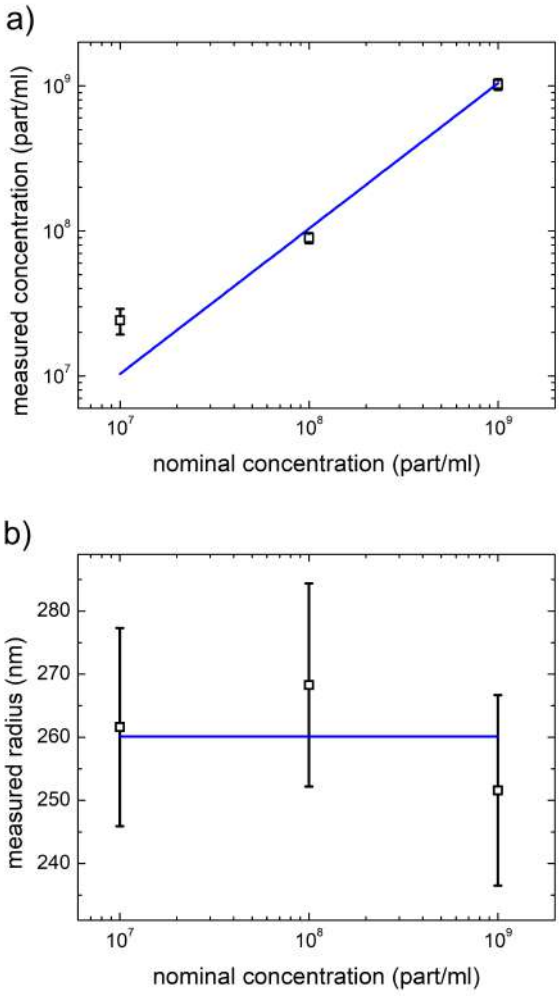

FIGURE 3.4: Particle concentration (a) and corresponding measured radius (b) for NIST polystyrene standard sample of the nominal radius of 254 nm as a function of the nominal concentration. The error bars are the propagated errors and relative errors of 6%. The blue lines represent the linear fit (reported in log-log scale) and the average radius (reported in linear-log scale) for concentration and radius dependence, respectively.

Although, in this case, the asimmetry seems to be attributable to the sample, as suggested by the SEM image reported in figure 3.5b, we have to keep in mind that the shape of LTS distribution is strongly influenced by the experimental error propagation. Therefore it is not possible to extract information from this parameter.
The avarage radius is further confirmed by the SEM distribution, reported as the red histogram in figure 3.5a. The distribution, extracted from the analysis of about 100 particles through the Gwyddion analysis software [31], provides a mean radius of 51 nm. The mean radius value obtained from LTS is also confirmed by DLS results ($R = 59$ nm), although with a very slight difference. The obtained avarge radii are summarised in table 3.1 (for completeness are reported also the FWHM). A similar behavior is also observed for the polystyrene sample of nominal radius of 163 nm (Seradyn, Indianapolis, IN - USA). The measurement results are reported in figure 3.6a. In this case, the LTS distribution shows a mean radius of 148 nm, different from the nominal ones. However, the LTS mean radius is confirmed by the analysis

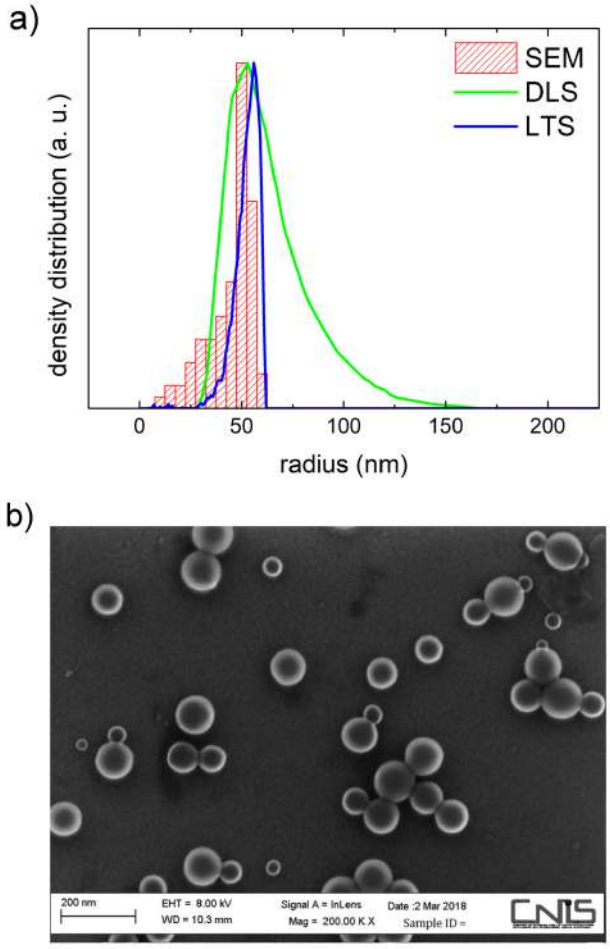

FIGURE 3.5: a) Particle density distribution for polystyrene sample of nominal radius 50 nm as results from SEM, DLS and LTS measurements. b) SEM image of polystyrene sample ($R_{nominal} = 50\ nm$) deposited on silicon substrate.

of some SEM images (a typical image is shown in figure 3.6b). Indeed, the obtained SEM distribution provides a radius of 145 nm. Also DLS distribution, although it is very broad, confirm the LTS result, providing a mean value of 169 nm for the radius. Distribution parametres measured by LTS, SEM and DLS are reported in table 3.2. Also for this sample, LTS technique provides results confirmed by SEM and DLS, in terms of avarage radius. To support this result, we also measured other polystyrene sample of nominal radius of 230 nm, 411 nm and 1100 nm. The measured mean radii as a function of nominal ones, are shown in figure 3.7a. This plot shows a very good accordance between the LTS measured radii and nominal ones (as highlighted by the black dashed line). Moreover, the LTS distribution mean radii are consistent with the SEM ones, and are definitely better than the corresponding DLS distribution. In particular, focusing on the results for the sample of 1100 nm radius, it is clear that DLS fails, whereas LTS provides very good results. The reason behind this behavior is that LTS measures the static light scattering while DLS the dynamic light scattering. Therefore, DLS is inevitably influenced by the motion (dynamic) of the suspended particles. The analysis behind DLS technique is based on Brownian motion and the results are reliable only for particles subject to this behavior. For particles of 1100 nm of radius, the motion is not really Brownian and the resulting radius is distorted.

	LTS	SEM	DLS
radius	54 nm	51 nm	59 nm
FWHM	20 nm	10 nm	108 nm

TABLE 3.1: Radius and FWHM of polystyrene particles with nominal radius of 50 nm and concentration of 1×10^{12} $part/ml$, obtained from LTS, SEM and DLS techniques.

	LTS	SEM	DLS
radius	148 nm	145 nm	169 nm
FWHM	18 nm	16 nm	100 nm

TABLE 3.2: Radius and FWHM of polystyrene particles with nominal radius of 163 nm and concentration of 7×10^9 $part/ml$ obtained from LTS, SEM and DLS techniques.

All the results discussed above, demonstrate that the LTS technique provides size resolution definetly better than DLS. These performancies are comparable with SEM, but with the advantage of a wide radius statistic. Moreover, the LTS has the peculiar characteristic of providing the absolute concentration with an extreme affidability.
As a matter of fact, the comparison between nominal and measured concentrations, for all the polystyrene sample are shown in figure 3.7b.
The measured values are in excellent agreement with the nominal ones over a wide range of concentrations, from $10^{12} part/ml$ down to $10^7 part/ml$, according to the different particle sizes. For all the samples, the measured and nominal concentrations are equal within the uncertainity (about 10%), which is calculated as described in the section 3.1.

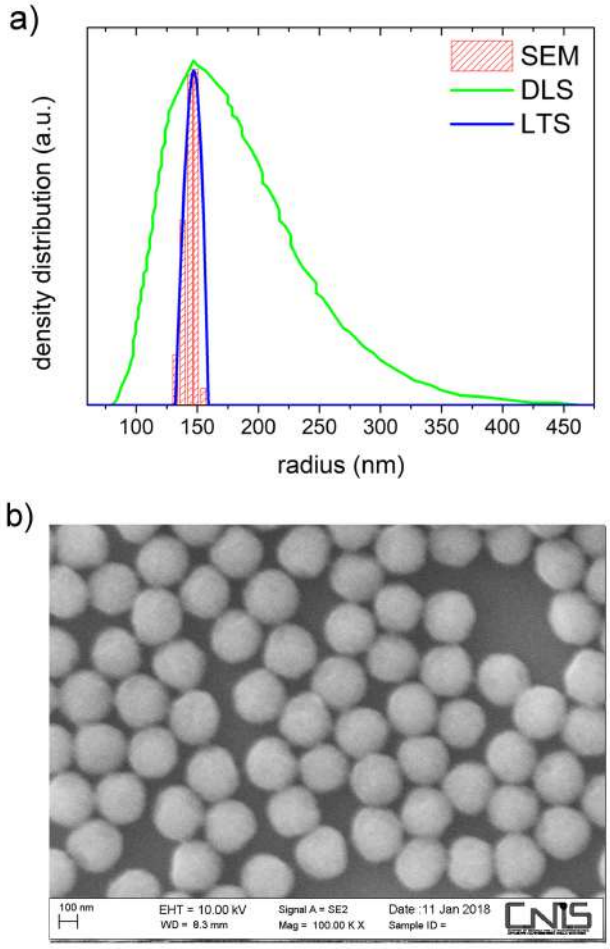

FIGURE 3.6: a) Particle density distribution for polystyrene sample of nominal radius of 163 nm from SEM, DLS and LTS measurements. b) SEM image of a polystyrene sample deposited on a silicon substrate.

3.2.2 Measurements on Silver suspended nanoparticles

Besides the polystyrene samples, we also measured a sample of silver particles of nominal radius of 50 nm and nominal concentration of 1×10^9 $part/ml$ (Ted Pella, Altadena, CA - USA).
Unlike the polystyrene, silver has a non-null immaginary refractive index and it thus absorbes a fraction of the incident light. Therefore, the transmittance of suspended silver nanoparticles, shown in figure 3.8, is influenced not only by the scattering but also by the absorption (as clearly visible in the region between 450 nm and 600 nm of wavelength). For these reasons, the content of information of the transmission coefficient is higher respect to non-absorbing particles and this is reflected on an achievable higher concentration sensitivity. Indeed, in this case we are able to measure concentration of the order of 10^9 $part/ml$, much lower than the measured value for the analogous size polystirene sample (of about 10^{12} $part/ml$). Also for the silver sample, we compared the density distribution obtained from LTS with those ones frome DLS and SEM. The LTS avarege radius results in very good agreement with SEM distribution and is much better that one obtained from DLS. The distribution parameters are reported in table 3.3. As to the absolute concentration obtained by LTS, the resulting value is $1.2 \pm 0.3 \times 10^9$ $part/ml$, which confirms the resolution

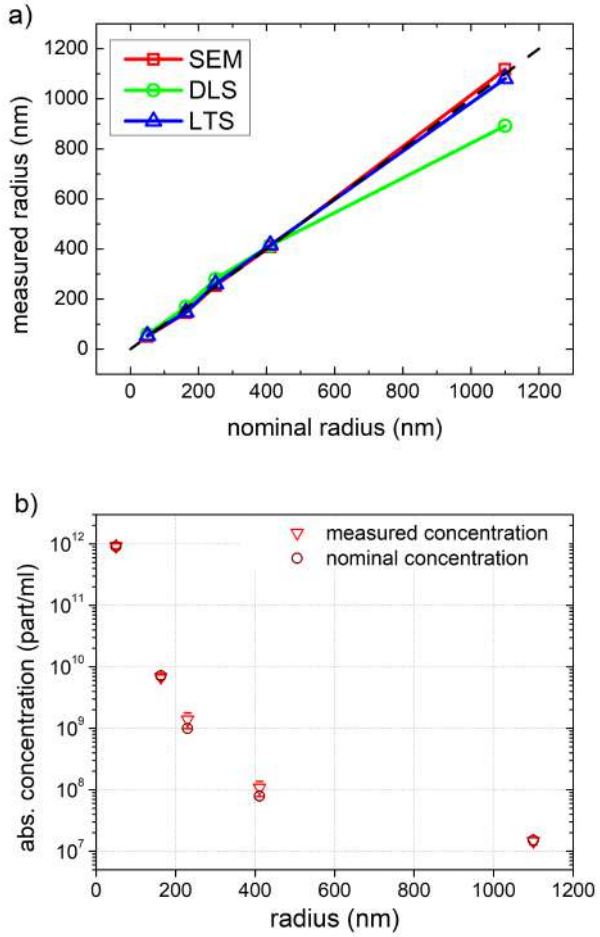

FIGURE 3.7: a) Comparison of the radii obtained by measuring different polystyrene samples in a size range between 50 *nm* and 1100 *nm*, by employing SEM, DLS and LTS techniques; the error bars represent the FWHM of the obtained distributions; the black dashed line rapresents the values for which the nominal and measured radii are equal. b) Comparison between the nominal and measured concentrations obtained by different polystyrene samples in a size range between 50 *nm* and 1100 *nm* of radius.

observed for polystyrene particles.

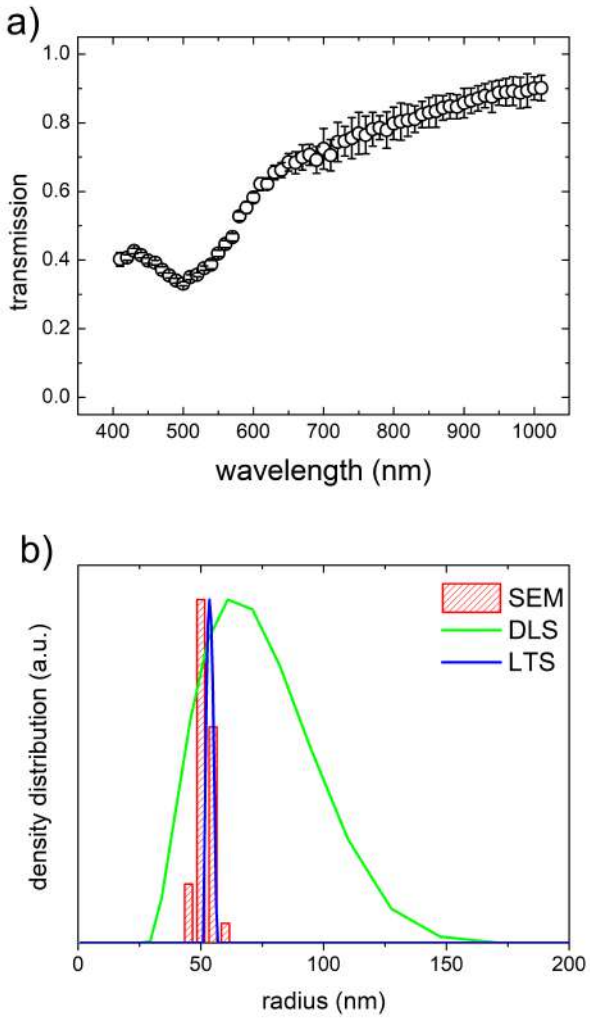

FIGURE 3.8: a) Transmission coefficient measured for a sample of silver particles of nominal radius of 50 nm and nominal concentration of 1×10^9 $part/ml$. b) Particle density distribution for a sample of silver particles of nominal radius of 50 nm and nominal concentration of 1×10^9 $part/ml$ from SEM, DLS and LTS measurements.

In conclusion, the apparatus developed for the LTS measurements allows to study suspended particles over a wide range of size and concentration. In particular, although with the used laser source the apparatus provides measurement between 410 nm and 1100 nm only, with the double ratio measurement method the propagation of the experimental error prevents to obtain reliable information on the shape and width of the distribution, the LTS average radius determination provides results better than those ones achieved from DLS and comparabale with those ones of SEM. Regarding the concentration, LTS allows to easily measure concentration of particles that are hardly detectable with DLS, and provides the absolute concentration value. From the experimental results, although the FWHM does not provides stable informations, the LTS determination of the average distribution radius and of the absolute concentration results to be very robust.

	LTS	SEM	DLS
radius	54 nm	51 nm	61 nm
FWHM	8 nm	12 nm	112 nm

TABLE 3.3: Radius and FWHM of a sample of silver particles with nominal radius of 50 nm and concentration of 1×10^9 $part/ml$ from LTS, SEM and DLS.

Chapter 4

Cases of study

Here, we present and discuss some interesting cases of study for which the LTS capability to provide size and absolute concentration of particles has been revealed fundamental. In particular, we report on the results obtained in different fields such as those ones of as pharmaceutics, biophysics and cultural-heritage. The studied samples are liposomes for drug delivery, microvesicles derived from Microglia cells in brain mice cancer and nanocapsules as biocide container for stone manufacts preservation. It is worth to notice that the broadness of the applications confirms the great potential of the LTS technique.

4.1 Liposomes characterisation for drug delivery

In the last fifty years, liposomes have become one of the most widely used vector systems for drug delivery (see the statistics provided by the Pubmed database [32]). This is basically due to their versatility, biocompatibility and possibility of modulating chemical-physical properties (e.g. size, surface charge, fluidity and thickness of the double layer, permeability to solutes, etc). It is also important to notice that owing to the above carge property of tunability, they are able to transport both hydrophobic and hydrophilic drugs [33]. Moreover, thanks to the lipid composition similar to that one of biological membranes, liposomes are able to cross the barrier represented by cell membranes and release the drug inside the cell. Another their important property is represented by the possibility of functionalising their membrane with different types of molecules and to direct them specifically towards a target system [34, 35]. In that way, they are able to improve the therapeutic index of a drug and its kinetics, allowing to reduce the dose of drug to employ, decreasing the toxicity of the molecule. In the lung disease field, one of the main effort from the pharmaceutical point of view is represented by the production of new drug delivery systems against pulmonary tuberculosis. Isoniazid is one of the main antibiotic agents active against tuberculosis as it is able to suppress the formation of mycolic acid, which is fundamental for the cell membrane of mycobacteria. Unfortunately, its efficacy is accompanied by serious side effects [36]. For this reason, the use of liposomes as vectors for isoniazid can be an application of remarkable interest.
In general, liposomes are employed to administration of several classes of drugs like antiviral, antifungal, antimicrobial, vaccines and gene therapeutics. They are applied in the immunology, dermatology, vaccine adjuvant, eye disorders, brain targeting, infective disease and in tumour therapy [37].

The strategy mainly used for the preparation of drug encapsulating liposomes can be summarised in three distinct phases:

- Preparation of liposomes and drug trapping,

- Purification of the solvent from the drug not trapped in liposomes,
- Check of the encapsulation efficiency.

As to the efficiency of encapsulation, it allows us to characterise the trapping capacity of a vector system. It is generally defined as the ratio between the mass concentration of drug trapped in the system ($C_{trapped}$) and that one of drug present in the final suspension (C_{drug}). This parameter is of fundamental importance since the effective quantities of encapsulated liposomes can be very different from those ones expected, for reasons related to the preparation of the sample itself, i.e. the loss of material during the preparation and purification processes.
Considering that drug-trapping liposomes are a colloidal suspension characterised by a certain volume fraction, it is possible to define in a more appropriate way the encapsulation efficiency by means of the volume fraction of liposomes

$$\phi = N_{lipo}\frac{4}{3}\pi R^3 \tag{4.1}$$

defining the concentration of drug trapped as

$$C_{trapped} = C_M\phi = C_M N_{lipo}\frac{4}{3}\pi R^3 \tag{4.2}$$

where C_M is the drug concentration employed at the beginning of the preparation, N_{lipo} and R are the absolute concentration and the inner radius of the suspended liposomes, respectively.
Therefore, it is necessary to measure the amount of drug at the final stage of the preparation (C_{drug}) and, also, the absolute concentration (N_{lipo}) of a certain size (R) of the vesicles in which it was encapsulated. While the final drug concentration is typically measured by UV-Vis spectroscopy [38], the proper measurement of absolute concentration and size is more debating.

To date, for this purpose, microscopy techniques such as Scanning Electron Microscopy (SEM), Transmission Electron Microscopy (TEM) and Atomic Force Microscopy (AFM) are used [39]. Alternatively, methods based on size separation were also emplyed. Typical examples of such techniques are the Size Exclusion Chromatography (SEC), Differential Centrifugal Sedimentation (DCS) and Flow-Field Fractionation (FFF) [40]. Each of these techniques has strong limitations in the characterisation of absolute concentration and characteristic size of liposomes. Indeed, liposomes are structures composed of perishable organic materials and are sensitive to environmental conditions (temperature, pH, etc.). The structure of the liposome is held together by the entropic forces that are created in polar solvents and it is therefore difficult to preserve it in different environments. The vesicles are also sensitive to mechanical stresses. When studying loaded liposomes, it must also be taken into account that any disturbance (due to measurement techniques) can lead to losses of the included substance. It is therefore very difficult to develop techniques capable of performing efficient and non-invasive measures for such systems.
High Performance Liquid Chromatography (HPLC) is certainly a widespread method with better performances than previous techniques. This is an analytical chemistry technique: it allows to break down a sample into its fundamental chemical components by providing an estimate of the weight concentration (mg/ml) of the lipid

components of the liposomes. The sample is injected at fairly high pressures (hundred of atmospheres) into a column filled with adsorbent material and the less interacting molecules with the internal phase are first eluted. The output materials are typically quantified by UV-Visible (UV-VIS) spectroscopy [41]. In particular, through the Beer-Lambert low, the measured absorbance gives information on the concentration of the sample molecules. Therefore, this technique is sensitive only to molecules with absorptions in this spectral range, thus limiting the tipology of the samples to be analysed. Moreover, the HPLC does not provide direct information on the number of the objects in suspension, which can only be estimated by combining lipid concentration results with geometric models for liposomes.
In this scenario, LTS is certainly the optimal technique for obtaining the required informations, i.e. liposomes concentration ($part/ml$) and liposomes size. For this, we performed LTS measurements on liposomes of diffeterent compositions, both empty and loaded. The aim of this study is to confirm the applicability of LTS on these vesicular systems, comparing the results with the more established HPLC method. In order to compare LTS liposomes concentration ($part/ml$) with respect to HPLC lipid concentration (mg/ml), a conversion model has been introduced. Moreover, we demonstrated that LTS provides useful information also on liposomes that are not detectable with HPLC, for example unilamellar isoniazid encapsulating liposomes.

4.1.1 Materials

Samples were prepared in the Physics Department of the Sapienza University by the group of Prof. Federico Bordi. In the following, some characteristics of the two investigated samples are described.

Soy-Phosphatidylcholine - Cholesterol (SPC:Chol)

These liposomes are prepared with a composition ratio of SPC:Chol 80:20 in HEPES medium. Phosphatidylcholine, thanks to its amphiphilic nature, guarantees the formation of vesicles, while cholesterol in these molar proportions has the function of stabilising the membrane by raising the transition temperature [42]. The lipids of this preparation are detectable by the HPLC method. This allows the comparison between the HPLC and LTS results on the same system.

Hydro Soy-Phosphatidylcholine - 1,2-Dipalmitoyl-sn-glycero-3-Phosphoglycerol (HSPC:DPPG) with isoniazide (ISN)

These liposomes are prepared with a composition ratio of HSPC:DPPG 60:10 in HEPES medium with ISN, in molar concentration of 0.026 M. This formulation has a low percentage of negatively charged lipid with the advantage of decreasing possible interactions of the membrane with the drug (positively charged) but guaranteeing electrostatic repulsion between liposomes, useful for preventing aggregation. This is a preparation of interest for isoniazid encapsulation but it is not suitable for HPLC measurements. For this reason, it represents the kind of system for which the use of the LTS technique is more useful.

4.1.2 SPC:Chol liposomes as function of lipid concentration: LTS vs HPLC

To verify the applicability of LTS on liposomes, the SPC:Chol 80:20 sample was measured at different concentrations. LTS measurements are performed on liposomes

suspended in HEPES medium at a constant temperature of $25°C$, collecting the transmission data in the wavelength range between 410 nm and 1010 nm. For the analysis, the shelled sphere model was used, with a shell thickness of 5 nm (typical dimension of lipid bilayer). In figure 4.1 we report, as example, the transmission coef-

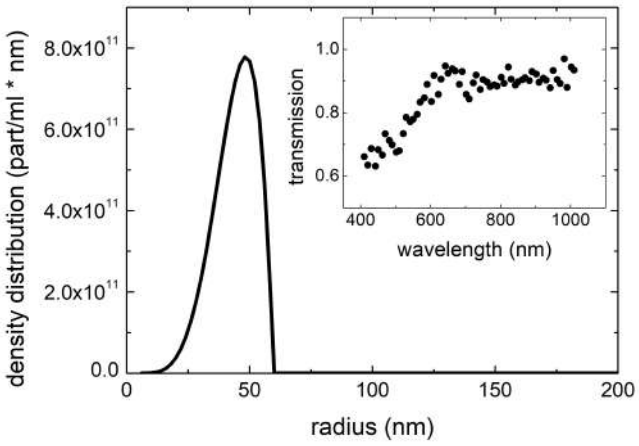

FIGURE 4.1: Density distribution as obtained from LTS measurements for SPC:Chol 80:20 liposomes suspension. In the insets the measured transmission coefficient is reported.

ficient (inset) and the distribution obtained by measuring SPC:Chol 80:20 liposomes suspended in HEPES medium whit a nominal lipid concentration of 0.95 mg/ml. The obtained distribution has a mean radius of 48 ± 3 nm and a concentration of $1.7 \pm 0.1 \times 10^{13} part/ml$. This is the lower concentrated sample measured in this experiment but it does not represent the sensitivity limit, as clear by the transmission coefficient reported in the inset of figure 4.1 (that is far from the limit of $T = 1$ over the entire spectral range).

We also analysed other samples with different (higher) nominal lipid concentration. LTS results (concentrations of liposomes per milliliter, $part/ml$) are shown in figure 4.2a as a function of the nominal lipids concentration (milligrams of lipids per milliliter, mg/ml). A clear linear dependence is observed and the data show a rather small scattering around the blue line in figure 4.2a, which represents the best fit line of a linear regression obtained with the intercept constrained to zero. The obtained angular coefficient is $1.78 \pm 0.08 \times 10^{13} part/mg$ where the error represents the 95% of confidence interval. Notice that, according with the above linear dependence, the average radius plotted as a function of the nominal concentration shown in figure 4.2b does not change appreciably over the whole concentration range. The blue line in 4.2b represents the average radius value of 47 ± 4 nm.

The same samples were also measured with HPLC technique obtaining in this case directly the weight concentration of lipids in mg/ml. In order to have a direct comparison between LTS and HPLC results, the former expressed in number densities of liposomes ($part/ml$) have to be converted into weight concentration of lipids in (mg/ml). To perform the conversion, a simple geometrical model has to be introduced. Once known the peculiar lipid species, the basic parameter to calculate the liposome weight is the number of lipid molecules per liposome.

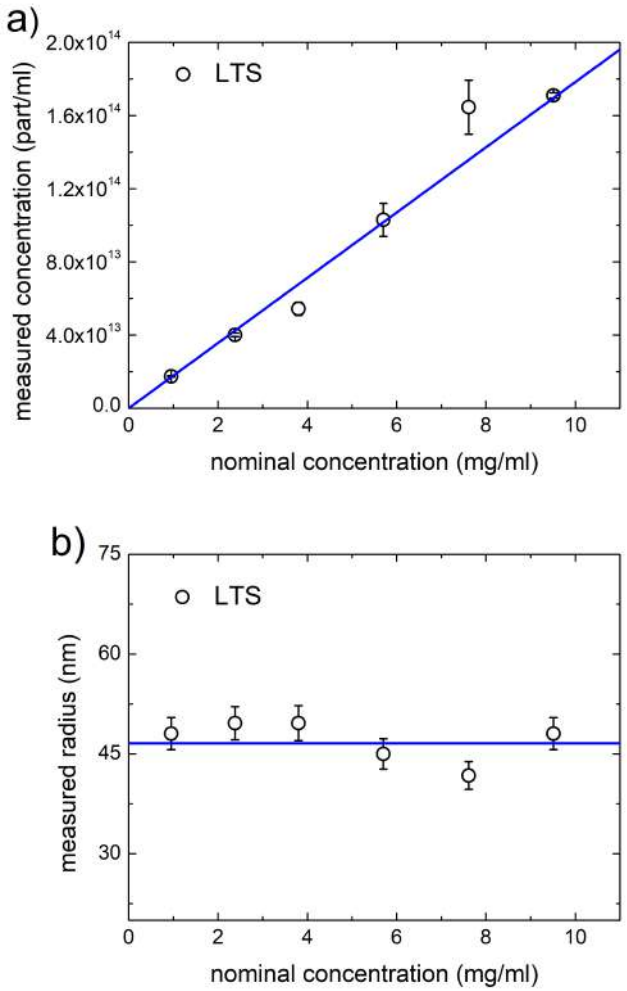

FIGURE 4.2: a) Particle concentration measured with LTS for SPC:Chol 80:20 liposomes suspension prepared with a lipid nominal concentration between 0.95 mg/ml and 9.5 mg/ml, and corresponding measured radius (b). The error bars are the propagated errors and the relative error of 6%, respectively. The blue lines represent the linear fit and the average radius for concentration and radius dependencies, respectively.

We define the number of molecules per liposome as

$$n_{lipids/liposome} = \frac{4\pi(R_{in}^2 + R_{out}^2)}{A} \tag{4.3}$$

where R_{in} and R_{out} are the inner and outer radii of the liposome, respectively, while A represents the occupation area of each lipid.
With this definition, the concentration of lipid molecules relative to each bin of the LTS distribution is calculated as

$$c_{lipid}^{bin}(lipid/ml) = c_{liposomes}(part/ml) \cdot n_{lipids/liposome} \tag{4.4}$$

Adding the contribution of all the distribution bin and taking into account the molar ratio f and the molecular weight M_W of the membrane components, it is possible to

obtain the mass concentration

$$C(mg/ml) = \sum_{bin} c^{bin}_{lipid}(lipid/ml) \sum_{j} f_j \frac{M^j_W(mg/mol)}{N_A} \tag{4.5}$$

The more critic parametre of this simple model is the area per lipid A. Its determination, indeed, is extremely complex, as it depends on the geometry, the chemical structure of the system and the environmental conditions. As a reference value of this quantity, the molecular area and the headgroup area are usually used. These quantities are generally measured through the Langmuir method [43]. However, these quantities are measured in a condition (membrane formed by a planar lipid monolayer) very far from the reality, in which there is a double-layer and, the area per molecule is different between the internal and external face, due to curvature effects [44]. Furthermore, if the vesicles are composed of different lipids with different molecular geometries, the lipids can be disposed in an inhomogeneous manner, for the internal or external face. Cholesterol, for example, having a very different structure from phospholipids, can lead to a lack of homogeneity of the lipid species in the internal and external surfaces of the liposome [45]. All these problems can be reflected in a higher value of the real area occupied by a lipid, with respect to the values measured as above [46, 47].
For the mass concentration values, calculated from liposome LTS distributions, we used an area per lipid value of 96.5 $Å^2$. The results of LTS concentration espressed in

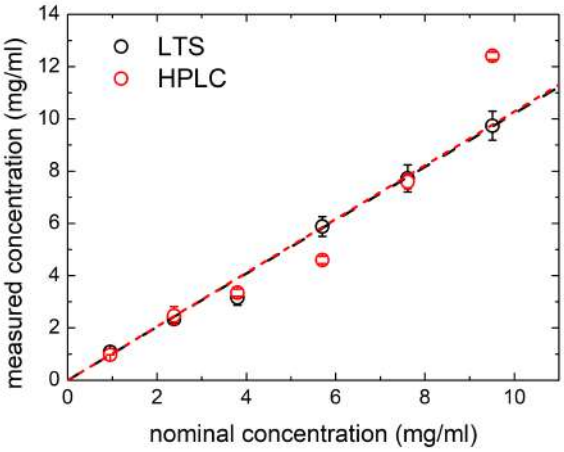

FIGURE 4.3: Lipid concentration for SPC:Chol 80:20 sample from LTS and from HPLC measurements as a function of nominal concentration. The dashed lines are linear fits.

mg/ml, in comparison with HPLC results, are shown in figure 4.3. The LTS results are in very good agreement with those obtained by HPLC. Moreover, for high lipid concentration, LTS results seem to be better than HPLC ones. Looking at the two fitting lines, the agreement between the techniques is further highlighted, but, more interstingly, the close correspondence with nominal values is clear. In particular, the fitted angular coefficients for LTS and HPLC values are 1.02 ± 0.02 and 1.03 ± 0.02, respectively. These results are very interesting, especially given the simplicity of the model used and the critical issues concerning the estimation of the area per lipid. They suggest the use of LTS technique also for the estimation of the occupation area per lipid in a vesicular system.

4.1.3 HSPG:DPPG isoniazide encapsulating liposomes as function of lipid concentration: LTS

The LTS characterisation was extended to the more complex system, i.e. the drug loaded liposomes. The studied liposomes have a lipid composition of HSPC: DPPG 6:1 with ISN in a molar concentration of 0.026 M. This system is characterised by both electrostatic interactions (inter- and intra-particle) due to the lipids and interactions with the solvent due to the presence of the drug. As mentioned above, the lipid composition used in this preparation does not allow HPLC measurements. Therefore, the LTS technique becomes fundamental for their characterisation. Also for this sample we performed LTS measurements at differerent concentration. The liposome measured concentration as a function of lipid nominal concentration is reported in figure 4.4a. Also in this case, the LTS results show a linear response, with an angular

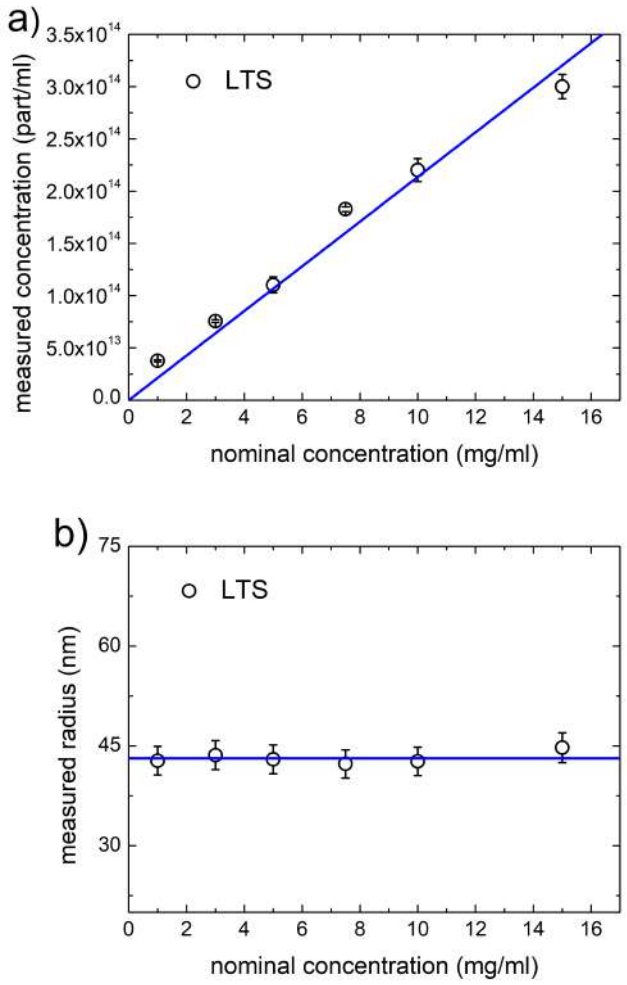

FIGURE 4.4: a) Particle concentration measured for HSPC:DPPG 60:10 liposome suspension prepared with a lipid nominal concentration between 1 mg/ml and 10 mg/ml, and corresponding measured radius (b). The error bars are the propagated errors and the relative error of 6%, respectively. The blue lines represent the linear fit and the average radius for concentration and radius dependencies, respectively.

coefficient of $2.1 \pm 0.1 \times 10^{13} part/mg$. The radius does not have concentration dependence, as shown in figure 4.4b, with an average value of $43 \pm 1\ nm$.
In conclusion, the results obtained for both liposome systems provide the great unique ability of LTS technique also for the characterisation of systems of pharmaceutical interest.

4.2 Microglia-derived microvesicles in Glioma: study of their dimension and concentration

Extracellular-released vesicles (EVs), such as microvesicles (MVs) and exosomes (Exo) provide a new type of inter-cellular communication, directly transferring a ready to use box of information, consisting of proteins, lipids and nucleic acids. In the central nervous system (CNS), microglia cells are responsible for the main form of active immune defense. In particular, their EVs participate in the neuron-glial cross-talk, an important two-way communication to preserve brain homeostasis and, when dysfunctional, involved in various diseases of the CNS.
Within a large collaboration including different departments of Sapienza University and "Istituto Italiano di Tecnologia", the possibility of using microglia-derived EVs could be used to transfer a protective phenotype to dysfunctional microglia in the context of a brain tumor (as the glioma) has been investigated [48].
Microvesicles (MV) released by microglia BV2 line cells in inflammatory conditions were isolated and analysed for their *in vitro* and *in vivo* effects in glioma bearing mice. In particular, MV released by untrated BV2 cells (control), BV2 cells treated with LPS/IFNγ (lipopolysaccharide and γ-interferon) and IL4 (Interleukin-4) were tested to verify their ability to interfere with glioma cell migration and proliferation. The results demonstrated that *in vitro* microglia derived LPS/IFNγ-MVs reduces the glioma cell movement and invasion. *In vivo*, LPS/IFNγ-MVs injected in the brain of mice with glioma reduces the anti-inflammatory phenotype of Tumor Associated Myeloid cells (TAMs) and significantly reduces tumor size and tumor induced neurotoxicity. This suggests that the cargo of LPS/IFNγ-MV, which contains specific mRNA for inflammatory genes, transfers this information to recipient cells modifying their gene expression profile toward a protective one. Altogether, these findings demonstrate that the administration of exogenous MVs could be a valuable approach to transfer protective signals to TAMs, restoring the homeostatic microglia phenotype.
In this context, we performed DLS and LTS measurements, which have been of fundamental importance for the size characherisation and for quantification of MVs employed both for *in vivo* and *in vitro* experiments. In particular, to avoid a different amount of MVs employed in the experiments, we measured the LTS absolute concentrations of MVs released by *i)* untrated BV2 (C-MVs), *ii)* BV2 treated with LPS/IFNγ (LPS/IFNγ-MVs) and *iii)* IL4 (IL4-MVs). In this section, we report in details the dimension and concentration analysis carried out [48], particularly highlighting the LTS contribution. The complete version of the paper is reported in appendix A.

4.2.1 LTS and DLS analysis of MVs derived from BV2 cells

The extraction procedure allowed to obtain vesicle samples of different volumes from a different number of BV2 cells. In particular, for untrated BV2, a volume of

480 μl of vesicles is obtained from a culture of about 1.3×10^9 cells. For the stimulated cells, indeed, the obtained volumes are of 150 μl and the number of cells are 4.6×10^9 (LPS/IFNγ) and 7.2×10^8 (IL4). These samples were diluted of a factor 4, 10 and 8 respectively, in order to optimize DLS and LTS measurements.
Microvesicle sizes were preliminary characterised by DLS performed at a constant temperature of 15°C on MVs suspended in KRH medium. The distributions, obtained by CONTIN analysis, are shown in figure 4.5. In particular, for C-MVs, the intensity-weighted distribution of hydrodynamic radius (figure 4.5a) shows that the main population is centered around 95 nm, providing the totals of the scattered intensity, as evidenced by the integral of the distribution reported in the inset. The obtained distribution has a polydispersity of about 36%, which attests the good quality of the isolated microvesicle sample. Simililar results are obtained also for MVs

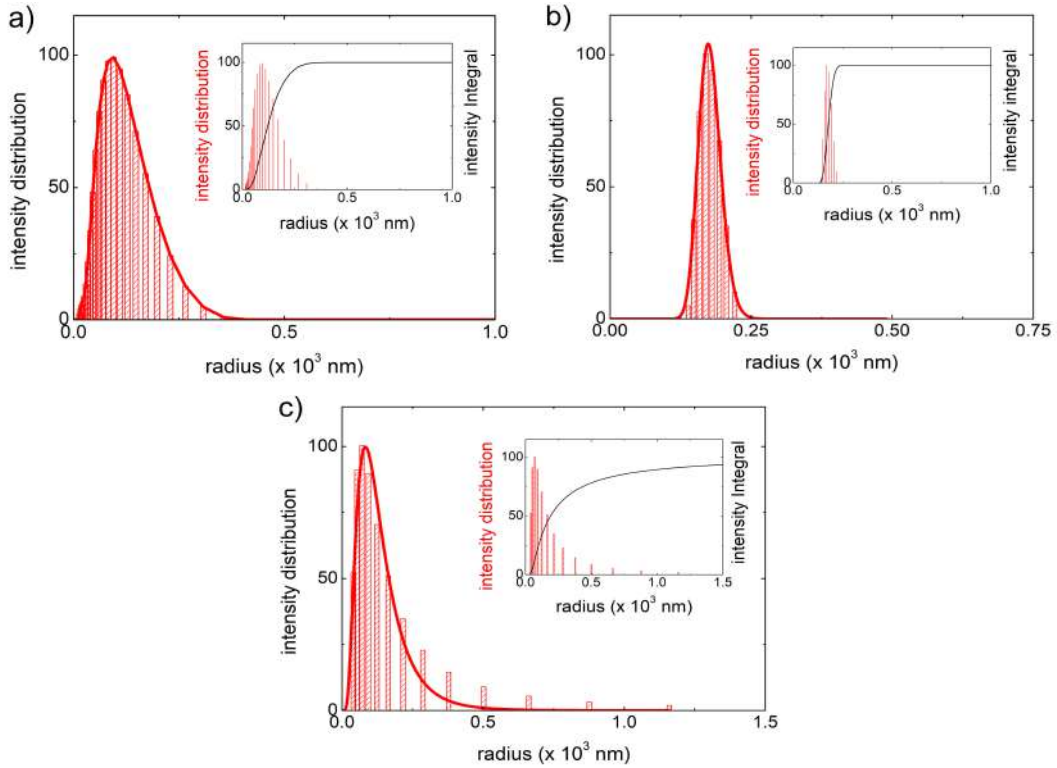

FIGURE 4.5: Hydrodynamic radius distribution as obtained from CONTIN analysis of the intensity autocorrelation curves (see appendix B), for microvesicles obtained from BV2 microglia cells (control) (a), from BV2 microglia cells treated with LPS/IFNγ (b) and IL4 (c). In the insets are reported the integrals of the intensity distributions.

isolated from stimulated cells. The distributions for LPS/IFNγ-MVs and IL4-MVs are centred around 170 nm and 140 nm respectively, with polydispersities of 5% and 35%, confirming also in these cases the presence of narrow populations of vesicles in the samples.
How to concern the LTS, our measurements not only confirmed the sizes obtained by DLS, but also provided the unique possibility to quantify the amount of MVs isolated from BV2 cells.
LTS measurements are performed on MVs suspended in KRH medium at a constant temperature of 15°C, collecting the transmission data in the wavelength range between 410 nm and 1010 nm. Also in this case the shelled sphere model with a shell

thikness of 5 *nm* has been used.
In figure 4.6 are reported the distributions obtained for C-MVs (4.6a), LPS/IFNγ-MVs (4.6b) and IL4-MVs (4.6c), with the relative transmission coefficients (shown in the insets). The distributions obtained from the analysis provides mean radii of

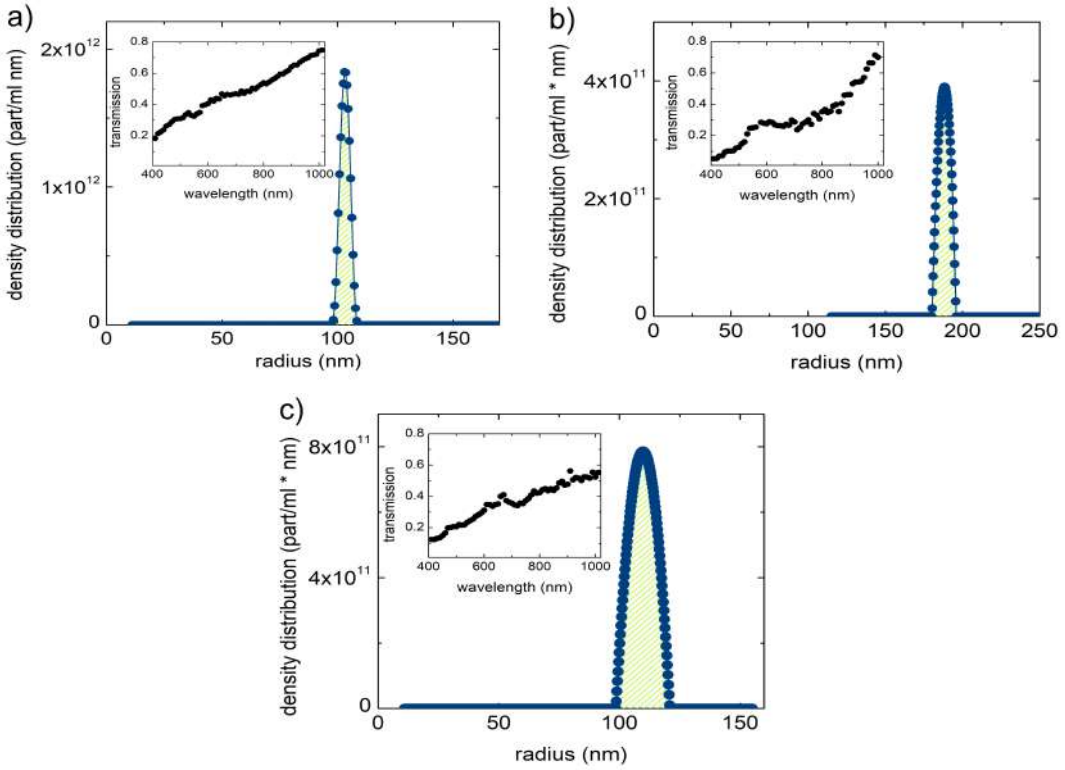

FIGURE 4.6: Density distribution obtained from LTS measurements, for microvesicles obtained from BV2 microglia cells (control) (a), from BV2 microglia cells treated with LPS/IFNγ (b) and IL4 (c). In the insets the measured transmission coefficients are reported.

102 ± 6 *nm* (C-MVs), 190 ± 10 *nm* (LPS/IFN*gamma*-MVs) and 109 ± 7 *nm* (IL4-MVs), in good accordance with DLS results[1].
For the concentrations, in the case of BV2-derived microvesicles (C-MVs), LTS measurements showed that the number of MVs per ml of solution is $9.95 \times 10^{12} vesicles/ml$. Taking into account the dilution factor, we found that the number of vesicles in 480 μl is about 1.9×10^{13}. Therefore, the number of vesicles produced by each cell is $N = 1.5 \times 10^4$.
LTS measurements performed on BV2-derived MVs stimulated through LPS/IFNγ showed that the number of microvesicles per ml of solution is $4.05 \times 10^{13} vesicles/ml$. Analogously, we found that the number of vesicles in 150 μl is about 6.1×10^{13}, meaning that each cell produces $N = 1.3 \times 10^4$ vesicles.
Similar results were obtained for BV2-derived MVs stimulated through IL4. In this case, indeed, the number of microvesicles per ml of solution is $1.16 \times 10^{13} vesicles/ml$. Taking into account the dilution factor, we found that the number of vesicles in 150 μl is about 1.4×10^{13}, meaning that each cell produces $N = 1.2 \times 10^4$ vesicles.
The results here reported, allowed us to conclude that the number of microvesicles per cell is comparable in the three cases. Therefore, considering that for both *in vivo* and *in vitro* experiments we employed microvesicles produced from a fixed number

[1]The error bar of each mean radius is the relative error of 6%

of cells (1×10^6), we can conclude that the response of the microvesicles stimulated with LPS/IFNγ, with respect to control and IL4-stimulated ones, is not influenced by a different amount of infused vesicles. This result was fundamental to achieve that LPS/IFNγ-MVs effectively transfer their cargo of mRNA to recipient glioma cells, modifying their genes and, consequently, their response in terms of movement, invasion and proliferation.

4.3 Silica nanostructures as biocide container in cultural haritage: their dimension and concentration characterisation

Most of the worldwide Cultural Heritage monuments are built using stone materials. Different types of natural and man-made stone materials (concrete, brickwork, mortar) have extremely variable physical and chemical properties (texture, high porosity etc), resulting with widely different abilities to resist weathering (durability) [49]. Decay of stone materials is due to their interaction with the environment: weathering and atmospheric conditions (such as light, temperature, humidity, pollutants, acid rain) [50, 51]. The most immediate consequence of this interaction is a chemical and physical alteration followed, in most cases, by biological colonisation. The biodeterioration of stone is associated to nearly all environmentally induced degradation processes in a synergic manner, as the presence of one deterioration process enhances the effectiveness of the others [52, 53]. Currently, to reduce the biological colonisation on outdoor surfaces, the biocides are applied directly on the stone surface or added into coating formulations [54]. These methods, however, have several important drawbacks. When the biocides are directly applied on the stone surface, the treatment is effective for a limited period of time and the biocides easily deteriorate and/or are washed away. When small biocide molecules are added into the coating formulation, they are subject to fast self-diffusion in the coating matrix [55, 56]. These disadvantages can be smartly faced by the encapsulation of biocides in nanocontainers and by uniformly dispersing them in the coating. The dispersed nanocontainers can release the biocide on demand, during the life of the applied coating. Literature [57] reports the synthesis and characterisation of a few systems, such as mesoporous silica-based materials, for controlled release of biocides over time.
In particular, our collegues of Liquid group (Science Departement of Roma Tre University) have synthesised silica-based nanocontainers, namely a core-shell nanocapsule (Si-NCs), loaded with one of the most common commercial biocide, i.e.
2-mercaptobenzothiazole (MBT) [58]. The formation of the nanocapsules involves the dripping of the TEOS (silicon oxide precursor) in a constantly stirred water bath. In particular, the quality of silica nanocapsules results influenced by the dripping and stirring speeds. To characterise this behaviour and choose the best syntesis parametres to obtain suspension of nanocapsules useful for stone material protection, we performed LTS measurements on suspension of Si-NCs obtained at different stirring speeds. The obtained density distributions, compared with DLS distribution and SEM images, are reported below.

4.3.1 Materials

The analysed silica nanocapsules are synthesised at dripping speed of 300 $\mu l/min$, with three different stirring speeds of the water bath (450 rpm, 400 rpm and 350 rpm). Since the syntesis products are dried nanocaspules (powder form), to perform our

measurements, we suspended the nanocaspules in deionised water. Immediately after the suspension preparation, a high amount of deposited material is observed. Therefore, preleveting the supernatant, we escluted from the samples all the non-suspended residuals. To control the mass concentration of suspended nanocapsules, we weighted the nanocapsule initial powder and the dessicated corresponding suspension residual. With this procedure, we obtained stable samples with mass concentrations of 4.5 mg/ml, 1.7 mg/ml and 1.8 mg/ml, for samples relative to stirring speeds of 450 rpm ((450rpm)Si-NCs), 400 rpm ((400rpm)Si-NCs) and 350 rpm ((350rpm)Si-NCs), respectively.

4.3.2 Characterisation of samples synthesised with different stirring speed

LTS measurements on suspended Si-NCs were performed collecting the transmission data in the wavelength range between 410 nm and 1010 nm, at a constant temperature of 25°C (the same temperature is used also for DLS measurements). For the shelled sphere model analysis, in this case, we used a thikness of 20 nm, as extimated from SEM images [59].
The LTS density distribution obtained for the (450rpm)Si-NCs sample is reported in figure 4.7a. This distribution shows a mean radius of 145 ± 9 nm, with a rel-

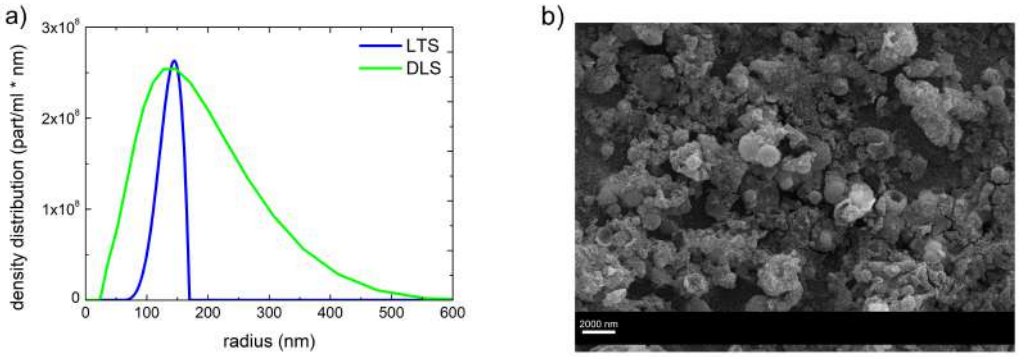

FIGURE 4.7: a) LTS density distribution compared with DLS intensity-weighed distribution of silica nanocapsules obtained with a stirring speed of 450 rpm. b) the corresponding SEM image of the silica nanocapsules. Scale bar: 2000 nm.

ative error of 6%, and an absolute concentration of $1.3 \pm 0.6 \times 10^{10} part/ml$. The size value is confirmed by the DLS intensity-weighted distribution (figure 4.7a) but observing the SEM image (figure 4.7b) some problems become evident. Indeed, beyond the nanocasules, a great amount of granules (probably unstructured silica) is present in the sample. These granules strongly influence the LTS and DLS measurements, which furnish a mean radius lower than that one obtained from microscopy (350 ± 40 nm). The analyses of the other two samples are reported in figure 4.8 and 4.9. For what concern the (400rpm)Si-NCs, LTS provides a mean radius of 290 ± 18 nm and a concentration of $2.3 \pm 0.8 \times 10^{8} part/ml$. In this case, the LTS results are confirmed not only from the DLS, but also from the SEM images (figure 4.8b). On this basis, the (400rpm)Si-NCs seem better than the previous one, in terms of lower amount of unstructurated silica, but show very broad distributions as observed from both the LTS and DLS analysis.
Looking, instead, at the SEM image (figure 4.9b), granules seem to be strongly reduced, and the nanocapsules have sizes more similar to each other. The LTS analysis provides a more narrow distribution with respect to the previous sample, but

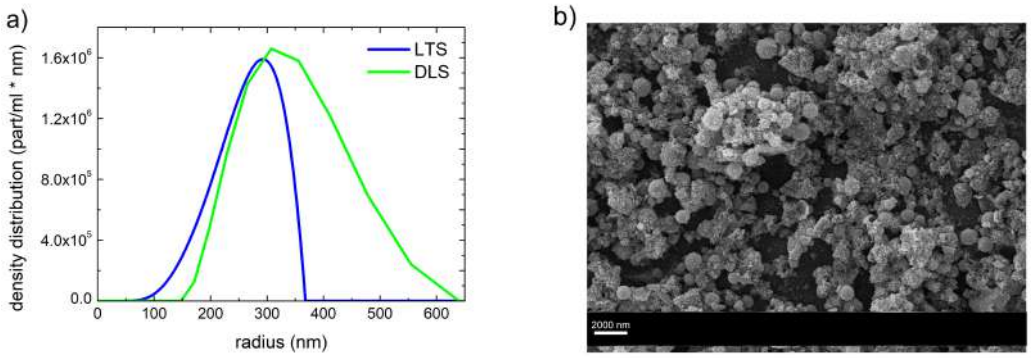

FIGURE 4.8: a) LTS density distribution compared with DLS intensity-weighed distribution of silica nanocapsules obtained with a stirring speed of 400 rpm. b) the corresponding SEM image of the silica nanocapsules. Scale bar: 2000 nm.

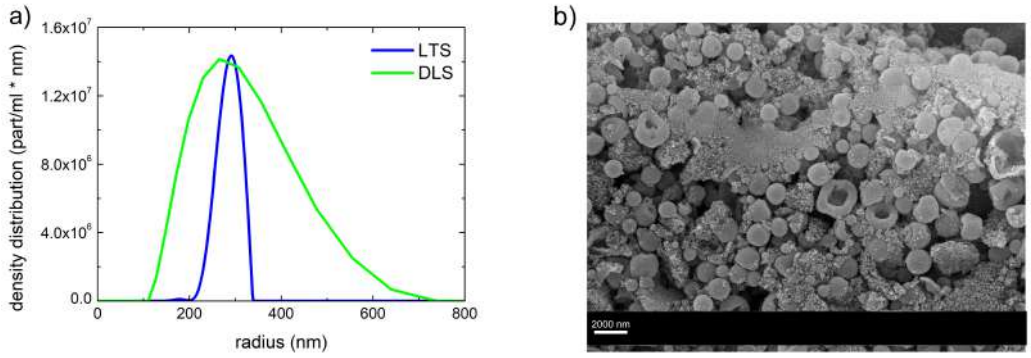

FIGURE 4.9: a) LTS density distribution compared with DLS intensity-weighed distribution of silica nanocapsules obtained with a stirring speed of 350 rpm. b)the corresponding SEM image of the silica nanocapsules. Scale bar: 2000 nm.

with the same radius of 290 ± 18 nm, also confirmed by DLS. However, the most interesting result is represented by the nanocapsule concentration. Indeed, although the mass concentrations of the two samples ((400rpm)Si-NCs and (350rpm)Si-NCs) are essentially the same (1.7 mg/ml and 1.8 mg/ml respectively), the (350rpm)Si-NCs concentration is $9.9 \pm 0.2 \times 10^8 part/ml$, which is almost an order of magnitude greater than that one of the (400rpm)Si-NCs. This result implies that the highest number of nanocapsules per milligram of powder is achieved for a stirring speed of 300 rpm, indicating that this is the better stirring speed for the syntesis.

Chapter 5

Variable gain lock-in amplifier for a new "balanced" measurement

Nowadays, the challenge is to investigate the role of nanoparticles or nanovesicles involved in biological processes, when their concentrations are less than 10^9 *part/ml* and/or their size ranges from few tens to few hundreds of nanometres. These characteristics are peculiar of the so called exosomes, extracellular vesicles that have recently attracted the growing interest of a vast community of researchers for their role of intercellular messengers with implications, for example, in cancer metastatisation, cell and bacteria differentiation, and infectious response [60, 61, 62, 63]. Moreover, the possibility of enhancing the sensitivity and, consequently, decreasing the minimal detectable concentration, is particularly important for samples difficult to prepare, as for example, purified proteins, oligonucleotides constructs or exosomes.
As previously discussed, when the nanoparticles size and concentration are small, also the light scattering and absorption processes that influence the transmittance are small, and the value of the transmission tends to one. In this cases, it is of paramount importance to develop methods to perform measurements with very low indetermination, in order to distinguish as much as possible slightest differences. Moreover, a higher quality of the transmission measurements can positively affect the results of the data analysis, providing more realiable density distribution. Among the possible experimental solutions, a double channel Lock-in amplifier with a tunable gain (that one proposed in chapter 2) allows to implement a new "balanced" method for performing LTS measurements. In this chapter we explain the balanced method and report the test measurements to validate the method. Finally, we report the comparison with the standard approach.

5.1 New "balanced" measurement method

As presented in chapter 2 and developed by Frank Li [1], to obtain the transmission and make it independent from random laser power fluctuations, the laser intensities are simultaneously measured in the sample and reference channels, before performing the sample-to-reference ratio calculation. Moreover, to avoid any differences in the sample and reference channels due to optical components that can affect the LTS measurements, an identical second set of data is acquired by inverting the sample channel respect to the reference one. This allows to calculate a second sample-to-reference ratio for each laser wavelength. However, this approach ("double ratio" method) to determine the extinction coefficient presents the drawbacks to propagate the total measurement indetermination and, consequently, to increase the associated final relative error.
The latter is particularly detrimental in measuring concentrations lower than 10^9 *part/ml*

and particles sizes ranging from few tens to few hundreds of nanometres. The possibility to vary the LIA gain allows to perform a calibration measurement ("balanced" method) to avoid the use of the double ratio method described before.
The basic idea is that, for each laser wavelength, the calibration measurement balances the amplitude of the voltage signals generated by the two silicon photodiodes, by acting on the LIA gain of each of its channels. In particular, for the calibration, we

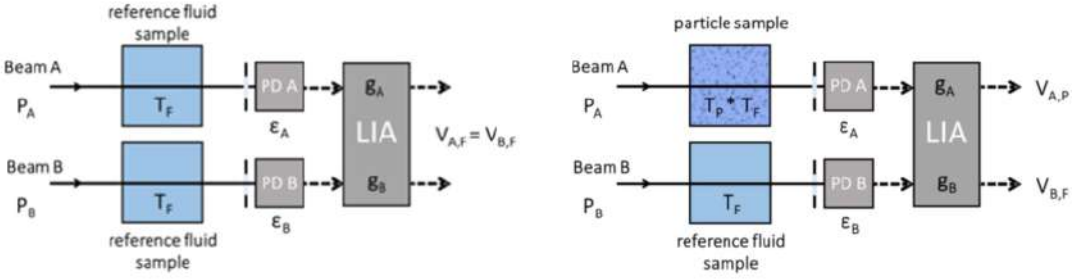

FIGURE 5.1: Sketch of measurement configuration: P_I are the intensities of two beams, T_I the transmission coefficients of particles and suspending fluid, ϵ_I the sensitivity of the detectors, g_I the gains of the two LIA channels and $V_{I,J}$ the output voltage signals.

measure the voltage signals proportional to the light intensity of the beams impinging on the detectors, after passing through the suspending fluid for each wavelength. Following the sketch reported in figure 5.1, for the calibration we obtain:

$V_{A,F}$ = signal through the suspending fluid F measured by the detector A

$V_{B,F}$ = signal through the suspending fluid F measured by the detector B

which can be defined as function of wavelength by the equations

$$\begin{aligned} V_{A,F}(\lambda_i) &= g_A \epsilon_A(\lambda_i) T_F(\lambda_i) P_A(\lambda_i) \\ V_{B,F}(\lambda_i) &= g_B \epsilon_B(\lambda_i) T_F(\lambda_i) P_B(\lambda_i) \end{aligned}$$

By tuning the gain of each LIA channel, it is possible to force the LIA output signals to be equal for each wavelength. This is equivalent to affirming that the voltage signals on the detectors are equal

$$V_{A,F}(\lambda_i) = V_{B,F}(\lambda_i)$$

and, consequently, that

$$\begin{aligned} g_A \epsilon_A(\lambda_i) T_F(\lambda_i) P_A(\lambda_i) = g_B \epsilon_B(\lambda_i) T_F(\lambda_i) P_B(\lambda_i) \Rightarrow \\ \Rightarrow \frac{g_A \epsilon_A(\lambda_i) P_A(\lambda_i)}{g_B \epsilon_B(\lambda_i) P_B(\lambda_i)} = 1 \end{aligned} \tag{5.1}$$

The relation 5.1 represents the balancing condition and corresponds to a perfect symmetry of the optics and detectors of the two channels.
Now, with this calibration, it is possible to obtain the transmission coefficient from

a single ratio between the voltages measured through the sample and the reference. Considering the sketch of figure 5.1, we have that the only difference in the measurement configuration is the presence of the particles to be investigated. The signal voltage

$V_{A,P}$ = signal through the particle sample P measured by the detector A

is defined by the relation

$$V_{A,P}(\lambda_i) \quad = \quad g_A \epsilon_A(\lambda_i) T_P(\lambda_i) T_F(\lambda_i) P_A(\lambda_i)$$

Therefore, dividing the intensity through the sample $V_{A,P}$ by the intensity through the reference $V_{B,F}$, we obtain the transmission coefficient of the particles in suspension:

$$\frac{V_{A,P}}{V_{B,F}} = \frac{g_A \epsilon_A(\lambda_i) T_P(\lambda_i) T_F(\lambda_i) P_A(\lambda_i)}{g_B \epsilon_B(\lambda_i) T_F(\lambda_i) P_B(\lambda_i)} = \frac{g_A \epsilon_A(\lambda_i) P_A(\lambda_i)}{g_B \epsilon_B(\lambda_i) P_B(\lambda_i)} * T_P = T_P \tag{5.2}$$

The simplified form of the equation 5.2 results in a lower impact of the propagation of experimental error with respect to the "double ratio" method.

5.2 Channel balancing: calibration measurement and temporal reproducibility

The calibration procedure consists in choosing the proper gains that make the intensities of the two channels equal to each other (as described in section 5.1). In detail, for each wavelength, we measure the voltage (proportional to the light intensity) of each channel of the LIA and, tuning its gain, we compensate the difference between these two values. Once the voltage difference becomes lower than the 1% for each wavelength used in the LTS measurement, we save the value of the proper gains with the corresponding wavelength. These values are collected in an external file and then automatically applied in the measurement of suspended particles, to ensure to achieve the balancing condition described above.
To verify the goodness of this method, we performed the calibration procedure using deionaized water as suspending medium. The ratio between the measured intensities obtained by the calibration procedure for seven wavelength, between 410 nm and 1010 nm, is reported in figure 5.2a. The ratio between the LIA output voltage pulses is very close to 1 and the error bars, calculated by the propagation of the maesured uncertainity, are within the 2%. The red line represents the mean value of 0.999 ± 0.006, where the error represents the 95% confidence interval. These results show that the calibration procedure guarantees a very good compensation of the differences between the two optical channels and allows to obtain the particle transmission coefficient from the single ratio of the voltage amplitudes coming from the sample and reference channels.
After the calibration, we checked its temporal reproducibility, measuring the same NIST standard polystyrene nanoparticle suspension (nominal radius of 254 nm and concentration of 1×10^9 $part/ml$), already employed for the double ratio test measurements (see section 3.1). The extinction coefficients obtained by performing three balanced measurements on NIST sample, for different times after the calibration procedure, are reported in figure 5.2b. The results obtained at times of 0, 6 and 24 hours after the calibration are very similar, with a relative error less then 7%. These data demonstrate that the "balanced" method is powerful, reliable and reproducible.

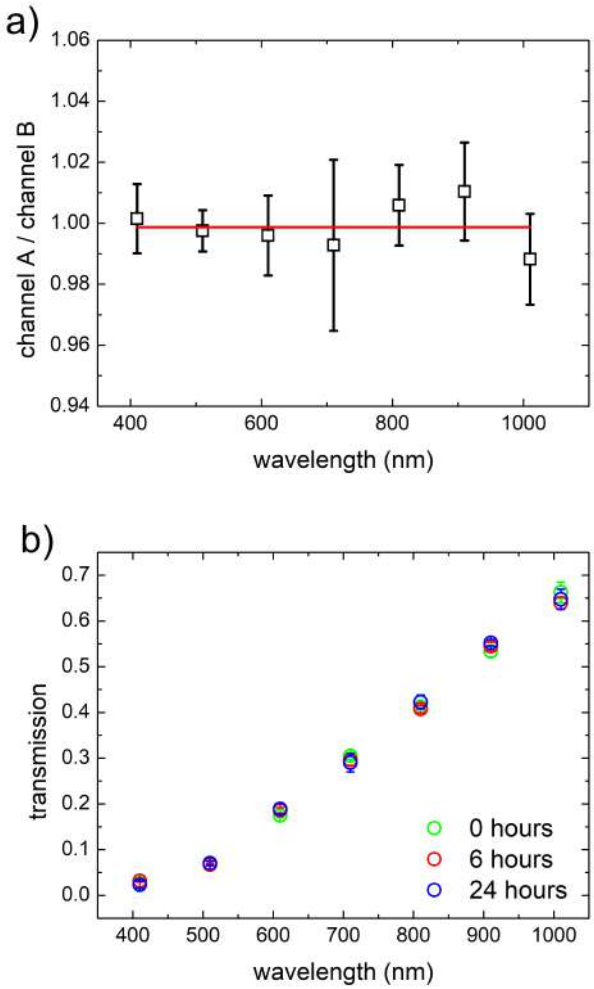

FIGURE 5.2: a) Ratio between the transmitted laser intensity through the signal and reference channels in absence of particles after performing a calibration run (see text). b) Extinction coefficient as a function of wavelength of a NIST standard polystyrene particle suspension ($R_{nominal} = 254\ nm$, $C_{nominal} = 1 \times 10^9\ part/ml$), measured at 0, 6 and 24 hours after the calibration procedure.

The excellent temporal reproducibility allows to avoid the LIA calibration immediatly before the measurement for each wavelength, and, moreover, to performs the calibration only one time, at least during 24 hours of measurements.
This is the first interesting result that implies a halved measurement time with respect to the double ratio method.

5.3 Comparison with the standard method

In order to compare the "balanced" method with respect to the "double ratio" one, we measured the transmission coefficient of the NIST sample already analysed in section 3.1.1 employing the two methods. The comparison between the transmission coefficients are shown in the inset of figure 5.3a. However, a more suitable comparison can be done considering the calculated extinction coefficients, which represent the input data of the analysis software. Looking at figure 5.3a, it is evident that the

error propagation induces an uncertainity much lower for the balanced method respect to the double ratio method, in particular in the low wavelength region. More-

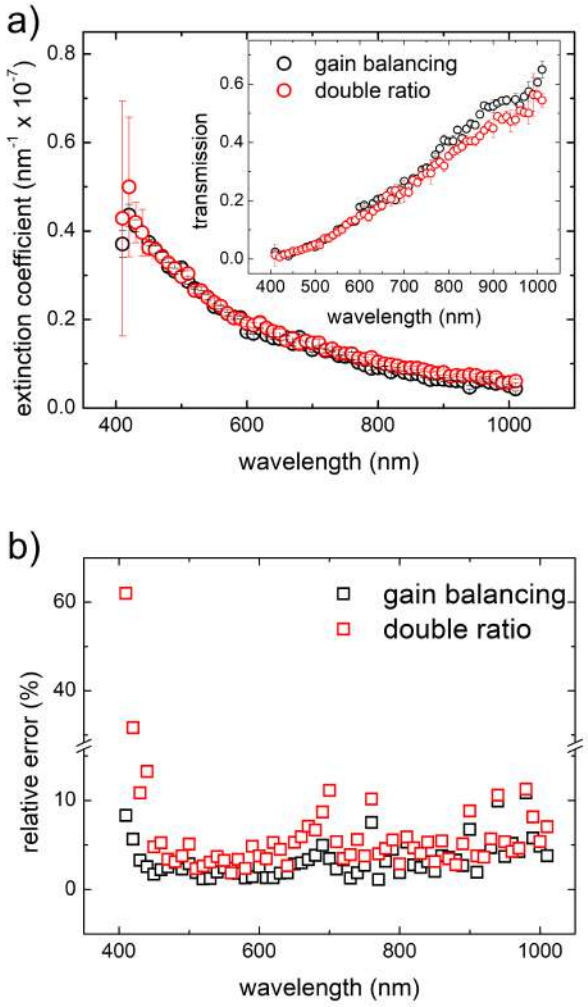

FIGURE 5.3: a) Extinction coefficient as a function of wavelength of a NIST standard polystyrene particle suspension ($R_{nominal} = 254\ nm$, $C_{nominal} = 1 \times 10^9\ part/ml$) obtained by the balanced method (black) and the double ratio method (red). In the inset the respective transmission coefficients are shown. b) Comparison between the extinction coefficient relative error for the balanced (black) and double ratio (red) methods.

over, analysing the wavelength dependence of the relative errors (figure 5.3b), it is more evident that the uncertainty significantly decreases, especially in the region of the lower wavelengths. This region is the most interesting in the perspective of measuring low concentrated samples and small size particles in view of the biological and biomedical applications. The relative error obtained from the balanced method for wavelengths below 450 nm is almost six times lower than that one from the double ratio method, while for the higher wavelengths the difference is less evident. On this bases, we expect an increased resolution in the analysis, which strongly depends on the error of the input data (as discussed in section 1.5.3). The analysis of the balanced method data (black circles in figure 5.3a) furnishes the density distribution reported in black in figure 5.4. If compared with the density distribution

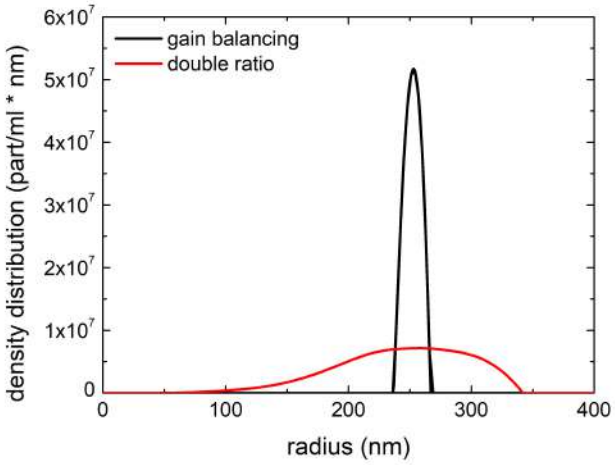

FIGURE 5.4: Comparison between the density distribution of a NIST standard polystyrene particle suspension ($R_{nominal} = 254\ nm$, $C_{nominal} = 1 \times 10^9\ part/ml$) obtained through balanced (black) and double ratio (red) methods.

obtained by using the double ratio method (red), it is evident that the new method provides a particle shape distribution much narrow and much more similar to that one expected from the NIST specification (refer to section 3.1). In particular, from the balanced method, the mean radius of the distribution is 253 nm and the FWHM is 20 nm, in very good agreement with the nominal values ($254 \pm 8\ nm$). The double ratio corresponding values, indeed, are 258 nm (radius) and 143 nm (FWHM). Thus, by using the balanced method, the particle size indetermination respect to the nominal value is equal to 0.3%, which is four times lower than the corresponding value calculated by the double ratio method.
As to the concentration, the balanced method furnishes a value of $1.01 \pm 0.03 \times 10^9\ part/ml$, while the analogous with the double ratio is of $1.03 \pm 0.09 \times 10^9\ part/ml$. As already observed, the estimate of the concentration is anyhow very robust.
The FWHM decreases and the symmetric shape of the distribution, marks a very significant enhancement of the performances. The density distribution in now more reliable and very close to the real one, differently from what observed and discussed in section 3.1.1. Moreover, the possibility of reducing the measurement time must not be neglected. For these reasons, we can assert that the balanced method represents an important improvement for the LTS technique.
This new method, combined with the recent extension of the usable wavelength range, is fundamental for the study of low concentrated samples. In the next future, we will perform preliminary studies of low concentrated sample.

Chapter 6

Towards LTS measurements of exosomes

In all domains of life, Eukarya, Archaea and Bacteria produce and release membrane vesicles for reasons that are still not completely understood [64]. In humans, many cells such as dendritic cells, lymphocytes and tumor cells actively release (i.e., by exocytosis) small (from 30 nm to 100 nm of diameter) membrane vesicles, referred as exosomes, into biofluids (i.e., plasma/serum, urine, cerebrospinal fluid and saliva). These vesicles are powerful cell-to-cell messengers as they transfer lipids, proteins, DNA and ribonucleic acids (i.e., mRNA, microRNA, lncRNA and other RNA species) between cells [60, 65, 61]. In the last few years, exosomes and their inner content (i.e. nucleic acids, proteins and other small molecules) have been also exploited as innovative and effective biomarkers for the diagnosis of many different diseases (i.e., tumors, obesity, gastrointestinal disorders, fibromyalgia, etc.) [66],[62, 63, 67].
For these reasons, quantitative and label-free analysis of membrane vesicles and, more in general, of their progemitor cells is very challenging and widely investigated nowadays. In particular, articulated imaging techniques based on the refractive index contrast analysis are recently developed [68]. Laser Transmission Spectroscopy, instead, can be considered as a relatively simple technique with very powerful applications in this field. LTS, indeed, allows to measure with high precision both size and concentration of the vesicles produced by cells grown at different environmental conditions.
Similarly to human cells, either gram-negative and gram-positive bacteria produce extracellular vesicles, referred as Outer-Membrane Vesicles (OMVs) and Membrane Vesicles (MVs), respectively.
In this chapter, we report a preliminary biophysical characterization perforemed by Dynamic Light Scattering (DLS), Transmission Electron Microscopy (TEM) and Small Angle X-ray Scattering (SAXS), which showed interesting membrane properties (phase transitions) that allowed to discriminate OMVs from Escherichia coli grown at different temperatures and to distinguish vesicles coming from different bacteria (i.e., gram-positive and gram-negative bacteria), with great relevance in biomedical applications.
These properties will be deeply studied through LTS technique in next future.

6.1 Membrane phase transitions of E. coli Outer Membrane Vesicles (OMVs)

Gram-negative bacteria (e.g. Escherichia coli, Pseudomonas aeruginosa, etc.) spontaneously secrete OMVs, small (from 20 nm to 100 nm of diameter) spherical bilayered vesicles, delivered in a variety of environments, including planktonic cultures, fresh and salt water, biofilms, inside eukaryotic cells and within mammalian hosts [69, 70, 71, 72]. Also gram positive bacteria (Lactobacillus rhamnosus, Staphylococcus aureus, Bacillus subtilis, Bacillus anthracis, Streptomyces coelicolor, Listeria monocytogenes, Clostridium perfringens, Streptococcus mutants, and Streptococcus pneumoniae) spontaneously produce MVs, as reported by [73, 74, 75, 76, 77, 78, 79, 80].
Owing to the recent employ of OMVs and MVs as adjuvants in vaccines [80, 81] or as novel vaccines platform [82], to regulate pathogenic processes [83], an in depth biophysical characterization (i.e., identification, discrimination and quantification) of these types of vesicles is highly desired for biomedical applications.
Here, we report the characterisation of morphology and size and the study of thermotropic properties of the lipid membrane vesicles. Indeed, although DLS is generally used to determine vesicles size, at the same time it provides information about the reorganization of lipid molecules of the membrane bilayer with a turbidimetric method [84]. Actually, the intensity of light scattered at a fixed angle by particles in a suspension depends on their size and on their optical properties, and concequently on the structure and on the refractive index of the components. By measuring the time-averaged intensity of scattered light as a function of the temperature, the apparatus allows the determination of thermotropic lipid phase transitions (with transition temperature Tc), related to the lipid organization and their remodeling within the bilayer, which affect the membrane optical properties (refractive index) [85]. In principle, observed differences in their thermotropic behaviour can be used to discriminate vesicles of different compositions, different bacterial origins or different culture conditions. In fact, it was previously known that E. coli bacteria show a phase transition due to conformational changes of the lipid component of the outer membrane [86] and that lipid composition modifications have been also observed in their membrane when the environmental conditions change (i.e. growth temperature) [87, 88]. Similar behaviour is expected also for vesicles.

6.1.1 Extraction procedure and analysis techniques

Bacterial culturing conditions and isolation of extracellular vesicles

E. coli ($ATCC8739$) was cultured at three different temperatures: $20°C$, $27°C$ and $37°C$ in essential M9 microbial growth medium consisting in Na_2HPO_4 (6.8 g/L), KH_2PO_4 (3 g/L), NH_4Cl (1 g/L) and $NaCl$ (0.5 g/L). To M9 medium, a solution containing D-glucose (4 g/L), $MgSO_4$ (241 mg/L) and $CaCl_2 \cdot 2H_2O$ (15 mg/L) was added and the resulting solution was adjusted to $pH = 7$.

Bacteria were cultured overnight until the culture reached an Optical Density at 600 nm of wavelength ($OD600$) of approximately 1. Lactobacillus rhamnosus (L. rhamnosus) LGG ($ATCC53103$) (Dicoflor 60, DICOFARM, Rome, IT) was cultured overnight in a De Man, Rogosa and Sharpe medium (MRS broth, 51 g/L) at $37°C$ in anaerobic conditions up to an $OD600$ of approximately 2. Aliquots (5 ml) of the bacterial culture (both E. coli and L. rhamnosus) were retained for further analysis and to be used as controls.

To isolate either OMVs or MVs, bacteria were removed from culture media by centrifugation (Beckman Avanti $J-25$ centrifuge, $JA-10$ rotor, $6000 \times g$, 15 min), and the supernatant was filtered through a 0.45 μm filter unit (Sartorius, Goettingen, DE). The supernatant, which contains vesicles, was concentrated by ultrafiltration (Vivaflow 200, Sartorius) up to small volume (50 mL) then filtered through a 0.45 μm filter.
Bacterial vesicles (OMVs or MVs) were separated by ultracentrifugation (107000 g for $3h$ at $4°C$) (Optima $XPN-100$ Ultracentrifuge, Beckman Coulter, $SW40$ Ti-rotor) of the ultrafiltered solution obtained previously. The pellet was washed once in phosphate buffered saline and suspended in the same buffer. At the end of the isolation protocol, a drop of the purified solution was cultured on agar plates at $37°C$ for one day to exclude the presence of residual bacteria.

Dynamic Light Scattering and turbidimetric analyses

DLS experimental set-up has been employed to provide vesicles size, as in its most common use, and to characterise the bilayer organisation because its sensitivity to the sample refractive index. In this case, we use the term "turbidimetric" measurements for this unconventional way of using a light scattering apparatus, although this term is not strictly appropriate, because we observe changes in the refractive index of the lipid membranes, concerning the scattered light and not the transmitted light, as in conventional turbidimetric measurements. DLS and turbidimetric measurements were performed employing a MALVERN Nano Zetasizer apparatus equipped with a 5 mW HeNe laser (Malvern Instruments LTD, UK). This system uses backscattering detection, i.e. the scattered light is collected at 173°. To obtain the size distribution, the measured autocorrelation functions were analyzed using the CONTIN algorithm [89]. The values of the radii shown in this work correspond to the average values on several measurement and are obtained from intensity weighted distributions [89, 90]. The thermal protocol used for OMVs, MVs, and bacteria in DLS measurements consists of an ascending ramp from $10°C$ to $45°C$ with steps of $1°C$ and thermalisation time chosen to obtain reproducible transitions with the shortest overall measurement time. The optimal thermalisation time for samples grown at $37°C$ was 360 s, for those samples grown at $27°C$ and $20°C$ was 720 s and 1080 s, respectively. These different time intervals are probably related to different concentration and size of the samples which in turn depend on the different growth temperature of the bacteria. For the turbidimetric determination of vesicle membrane thermotropic behaviour, we measured the mean count rate of scattered photons (i.e. the time-averaged intensity of the scattered light), I, as a function of temperature, T, and fitted the data to a Boltzmann sigmoidal curve:

$$I = I_0 + \frac{(I_1 - I_0)}{(1 + e^{((T-T_0)/\Delta T)})} \tag{6.1}$$

where the fitting parameters are I_0 and I_1, the minimum and maximum intensity respectively, the transition temperature T_0 , and the so called "slope" ΔT which describes the steepness of the curve. ΔT roughly measures the transition width.

Small Angle X-ray Scattering

SAXS experiments were performed at the Austrian SAXS beamline of the Elettra Synchrotron in Trieste, Italy [91]. SAXS images were recorded with a $2D$ pixel detector Pilatus3 $1M$ spanning the Q-range between 0.1 nm^{-1} and 6 nm^{-1}, with

$Q = 4\pi \sin(2\Theta)/\lambda$, where 2Θ is the scattering angle and $\lambda = 0.0995\ nm$ the X-ray wavelength. The image conversion to one-dimensional SAXS pattern was performed with FIT2D [92]. Detector calibration was performed with silver behenate powder ($d - spacing = 0.05838\ nm$). Samples were held in a 1 mm glass capillary (Hilgenberg, Malsfeld, DE). Experiments were carried out between $10°C$ and $45°C$, by using the same heating rate already adopted in DLS experiments. Each measurement was performed for 1 s and followed by a dead time of at least 10 s in order to avoid radiation damage. We obtained a set of SAXS curves resulting from the average of overlapping SAXS spectra obtained at about the same temperature ($\pm 1°C$), in order to analyse data with an improved signal-to-noise ratio. SAXS data were fitted according to a core-shell model [93] by GENFIT software [94], and taking into account the vesicle polydispersion, in agreement with the DLS results. The fitting parameters are OMVs radius R and thickness d, as well as the electron densities of the core and of the shell, ρ_i and ρ_e, respectively.

Transmission Electron Microscopy

Transmission electron microscopy (TEM) was used for the morphological characterisation of OMVs. Measurements were carried out at Department of Occupational and Environmental Medicine, Epidemiology and Hygiene of INAIL-Research in Rome, by using a FEI TECNAI 12 G2 Twin (FEI Company, Hillsboro, OR, USA). This instrument operate at 120 kV and is equipped with an electron energy loss filter (Biofilter, Gatan Inc, Pleasanton, CA, USA) and with a slow-scan charge-coupled device camera (794 IF, Gatan Inc, Pleasanton, CA, USA). Samples for TEM measurements were prepared by depositing 20 μl of vesicle suspensions on a 300-mesh copper grid for electron microscopy covered by a thin amorphous carbon film. Samples were deposited at room temperature. TEM images were performed both in the absence and in the presence of negative staining to test if the same structural information could be obtained and check the presence of possible artefacts, as already performed in a previous investigation on mammalian exosomes [95]. For negative staining, 10 μl of 2% aqueous phosphotungstic acid (PTA) solution (pH-adjusted to 7.3 using 1 $N\ NaOH$) was added before samples were completely dried.

Scattering intensity simulations

To better understand the behaviour of phase transitions in OMVs and bacteria, Mie scattering simulations were performed using the MiePlot 4.6 simulator by P. Laven [96, 97]. This simulator allows to calculate the scattered intensity as a function of scattering angle for inhomogeneous spheres where the refractive index is a function of the radius. For simplicity sake, both OMVs and bacteria were described as multiple-shelled spheres. In all the calculations, we assumed a wavelength of 633 nm for the incident light and a scattering angle of 173°. For the refractive index of the aqueous core (of both vesicles and bacteria), we used the value $n_{cytoplasm} = 1.367$ according to the literature [98], whereas for the bacterial cell wall we used $n_{cellwall} = 1.455$ [99]. Finally, we assumed that the dependence of the refractive index as a function of the temperature of the lipid membrane (both of vesicles and bacteria) was described by a Boltzmann sigmoidal curve (equation 6.1).

6.1.2 Vesicle characterisation and membrane phase transition study

DLS and TEM characterisation of OMVs

Size and shape of isolated OMVs at the three growth temperatures have been characterised by DLS and TEM measurements. Figure 6.1 shows the intensity-weighted

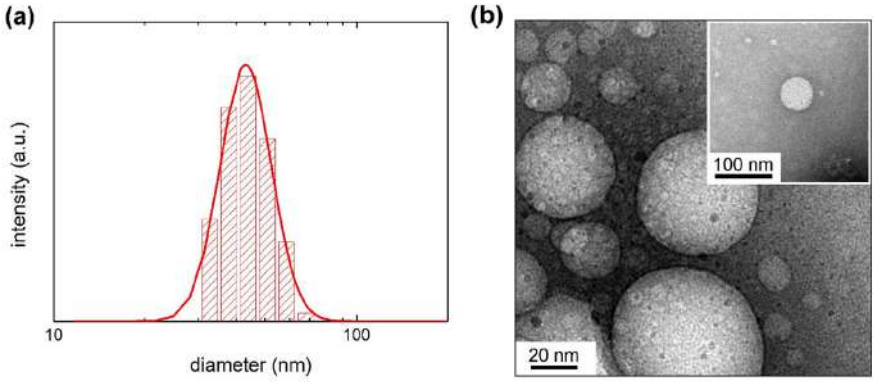

FIGURE 6.1: a) Dynamic Light Scattering intensity-weighed distribution of vesicles by E. coli grown at 37°C. b) Transmission Electron Microscopy image of vesicles by E. coli grown at 37°C obtained without negative staining. In the inset is shown a detail of a TEM image obtained with negative staining

size distribution of OMVs from E. coli grown at 37°C obtained by DLS measurements (panel a) and the morphological characterisation carried out by TEM microscopy, considering both the case of absence of any staining (panel b) and the PTA staining (inset of panel b). In both imaging conditions, we observed spherical vesicles. As shown in panel b, we observed a heterogeneous population of unilamellar spherical vesicles with size ranging from $\approx 15\ nm$ to $\approx 65\ nm$, in agreement with DLS intensity weighed distribution average values of $48 \pm 12\ nm$. Notably, the DLS analysis revealed that the vesicle size decreases as the growth temperature is lowered (Table 6.1). OMVs grown at 27°C and 20°C have a mean hydrodynamic

growth temperature	mean diameter	FWHM
37°C	$48 \pm 3\ nm$	$24 \pm 2\ nm$
27°C	$37 \pm 4\ nm$	$32 \pm 2\ nm$
20°C	$24 \pm 2\ nm$	$20 \pm 3\ nm$

TABLE 6.1: Mean hydrodynamic diameter and Full Width Half Maximum (FWHM) of DLS intensity weighed size distribution obtained by CONTIN analysis of correlation function measured at 23°C of OMVs by E. Coli grown at different temperature; reported errors are the standard deviation of three measurements.

diameter of $37 \pm 16\ nm$ and $24 \pm 10\ nm$, respectively. Typical TEM images and DLS intensity weighed distributions for vesicles grown at 27°C and 20°C are reported in figure 6.2. Such a reduction of the size of the OMV is probably related to a different lipid composition of the membrane of the vesicles released by the bacteria grown at different temperatures. Actually, it is well known that as the growth temperature is reduced, the content of unsaturated lipids, which confer a higher flexibility to the membrane, increases. However, once the vesicles are formed, their size is not

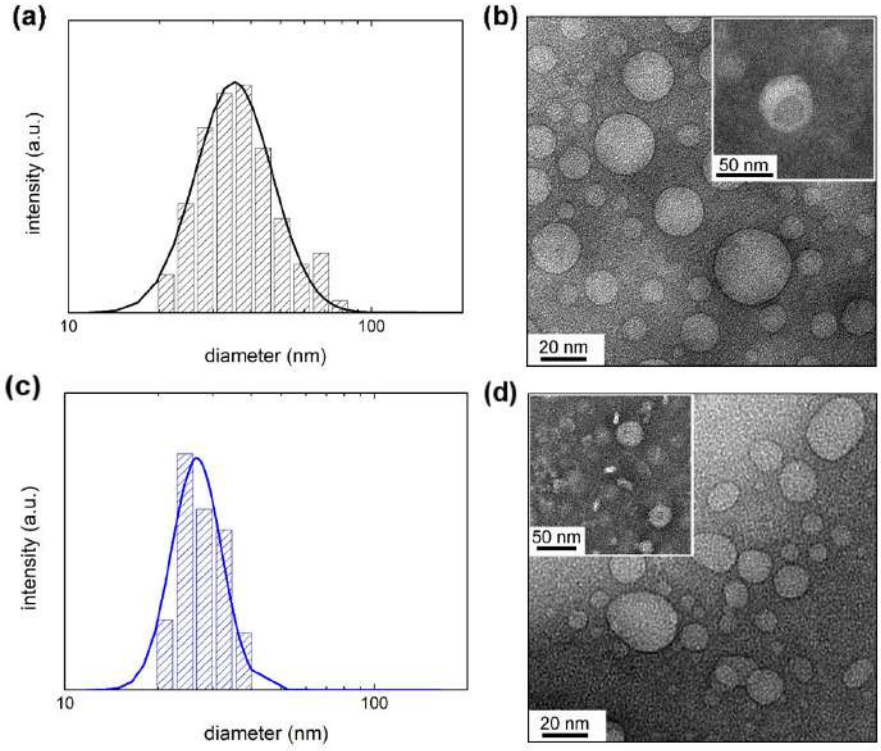

FIGURE 6.2: Dynamic Light Scattering intensity-weighed distribution of OMVs by E. coli grown at 27°C(a) and 20°C (c). Transmission Electron Microscopy image of vesicles by E. coli grown at 27°C (b) and 20°C (d) obtained without negative staining. In the insets details of TEM images obtained with negative staining are shown.

influenced by successive changes of the temperature, i.e. the size of the vesicles produced by bacteria grown at a given temperature does not change significantly over the range of temperature (10°C to 45°C) of interest for our measurements (see for example the lower panel of figure 6.3 of the section 6.1.2).

Turbidimetric experiments on Gram-negative OMVs

The intensity of light scattered at a fixed angle by particles in a suspension depends on their size, geometry and optical properties (structure and refractive index of the components). In particular, the refractive index of a lipid bilayer depends on the conformational state of the lipids and on their ordering in the bilayer. Hence, by measuring the time-averaged intensity of scattered light as a function of the temperature, it is possible to determine the thermotropic lipid phase transitions (with characteristic transition temperatures Tc), related to the lipid organization and their remodeling within the bilayer [85, 86]. In figure 6.3 the results obtained from turbidimetric measurements for vesicles (figure 6.3a) and, as comparison, E. coli (figure 6.3b) grown at 37°C are reported. How to concern the vesicles, the mean scattering intensity (figure 6.3a, upper panel) decreased significantly (about 25%) when the temperature was increased. We determined a transition temperature by fitting with a Boltzmann sigmoidal curve (equation 6.1) the experimental data (red line in figure 6.3a, upper panel). The fitting procedure provided a transition temperature of $32 \pm 2°C$, where the uncertainty is the fitted slope ΔT. In principle, the observed

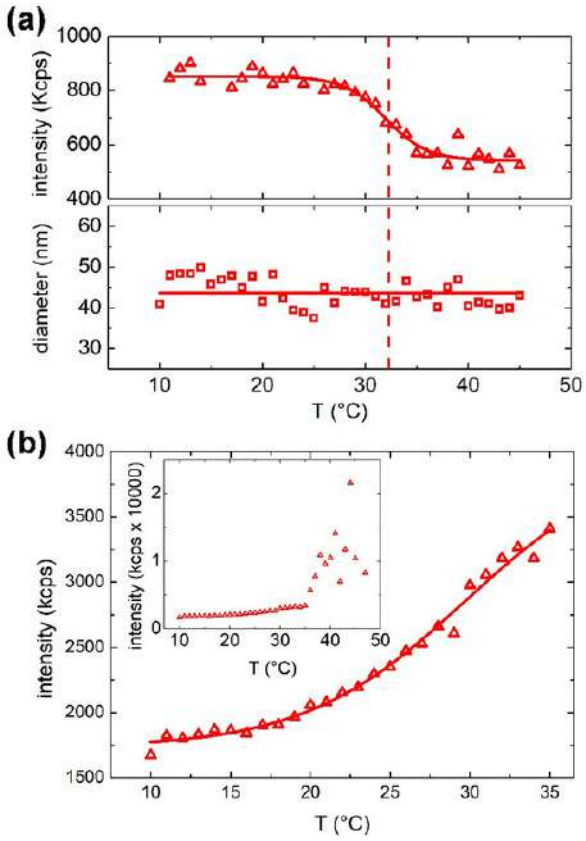

FIGURE 6.3: a) Mean scattering intensity (upper panel) and hydrodynamic diameter (lower panel) resulting from DLS measurements of vesicles grown at 37°C; red lines results from Boltzmann fit and linear fit, respectively, while the red dashed line highlights the transition temperature. b)DLS mean scattering intensity at increasing temperatures between 10°C and 35°C of E. coli bacteria grown at 37°C. In the inset the mean scattering intensity until 45°C is show (above 35°C the bacteria start to grow).

change of the scattered intensity, could be ascribed to different factors [100]: a decrease of the concentration, the size of the suspended particles, or a variation of vesicles refractive index [84]. However, we did not observe any phase separation (flocculation or precipitation of the particles) and the hydrodynamic diameter of the particles determined by DLS (lower panel of figure 6.3a) did not show any appreciable dependence on temperature. Hence, we ascribed the observed decrease of the scattered intensity to a change of the refractive index of the particles, likely due to a phase transition of the membrane lipid bilayer or, more in general, to a structural reorganization of the membrane [84]. The results obtained from a suspension of E. coli are reported in figure 6.3b. Again, also with bacteria, a rather steep variation of the scattered intensity was observed within the same temperature range observed in the case of OMVs, suggesting the occurrence of a similar membrane transition. However, in the case of E. coli, the scattered intensity increased, whereas in the case of OMVs decreased. The scattered intensity measurements were unreliable above 35°C because of bacterial proliferation increased and the concentration increase prevented the separation of this contribution from that due to variations of bacterial optical properties. Although this, a transition temperature of 30 ± 3°C was obtained (figure 6.3b). We attributed the opposite behaviour of the scattered intensity to the

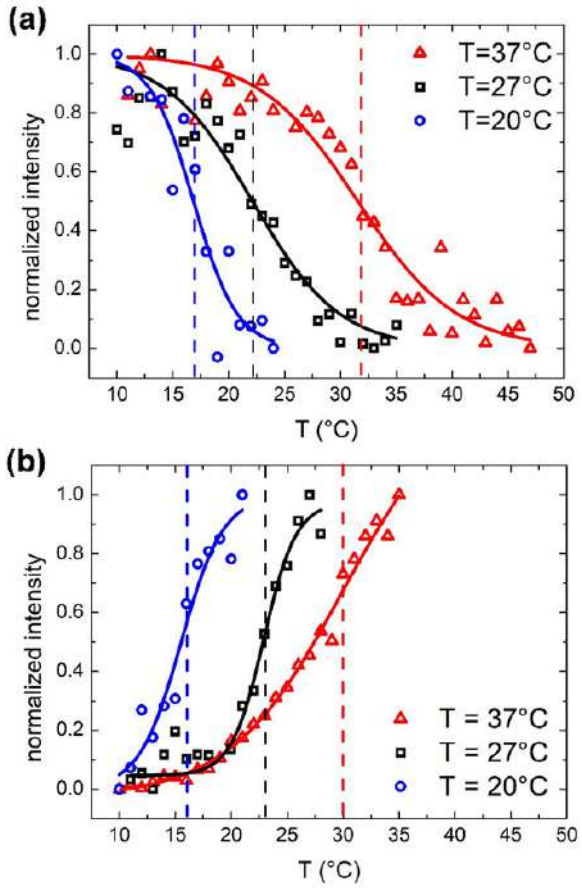

FIGURE 6.4: Normalised scattering intensity as a function of temperature: comparison between membrane phase transitions of OMVs (a) and E.Coli bacteria (b) grown at $37°C$, $27°C$ and $20°C$; vertical dashed lines highlights the transition temperatures.

different structures of the bacteria cell wall and, as a consequence, of the OMVs membrane.
Similar results were obtained also for samples (vesicles and bacteria) grown at $27°C$ and $20°C$. At these growth temperatures, OMVs were smaller (diameters were 37 ± 16 nm and 24 ± 10 nm, respectively, compared to 48 ± 12 nm at $37°C$) and their concentration (estimated by absorbance measurements) was found to be systematically lower than that obtained for the samples grown at $37°C$. Therefore, also the mean scattering intensity was significantly lower. Nevertheless, also in these conditions, the trend of the registered data suggested the presence of a phase transition. In figure 6.4 we compared the scattering intensity of vesicles (figure 6.4a) and bacteria (figure 6.4b) grown at different temperatures. For each sample, we reported the normalised scattering intensity, the fitting curve (solid line) and vertical dashed line that highlights the transition temperature. All the samples analyzed showed a similar behaviour in terms of phase transitions. Interestingly, for both OMVs and bacteria, a strong correlation between the growth temperature and the transition temperature of the membrane was found (figure 6.5). From previous E. coli studies, we know that, by reducing the temperature of the growth medium, the content of unsaturated lipids, which confer a higher flexibility to the membrane, increases.

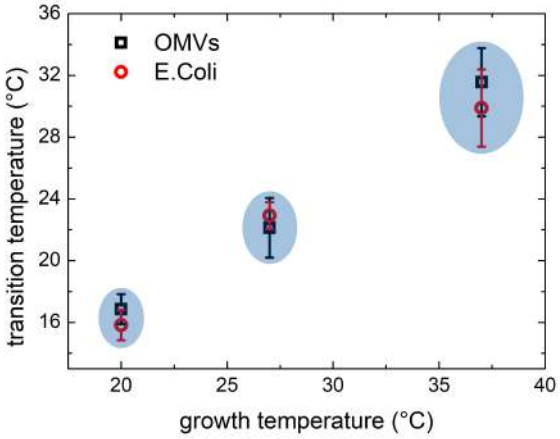

FIGURE 6.5: Comparison between phase transitions temperature of OMVs and E. coli bacteria grown at $37°C$, $27°C$ and $20°C$; the error bars represent the transition widths.

Moreover, bacteria membranes show thermotropic phase transitions whose characteristic transition temperature depends on the lipid composition [86], which, in turn, is related to the growth temperature [101]. It is reasonable to think that OMVs, originated from the bacterial outer membrane, may have a similar composition and similar thermotropic behaviours, but, to the best of our knowledge, this is the first experimental observation of this behaviour.

Scattering intensity simulations on Gram-negative OMVs

To better understand the different optical response observed for vesicles and bacteria, we calculated the scattering cross section of different structures simulating vesicles and bacteria by through Mie theory [97, 96]. Vesicles and bacteria have been

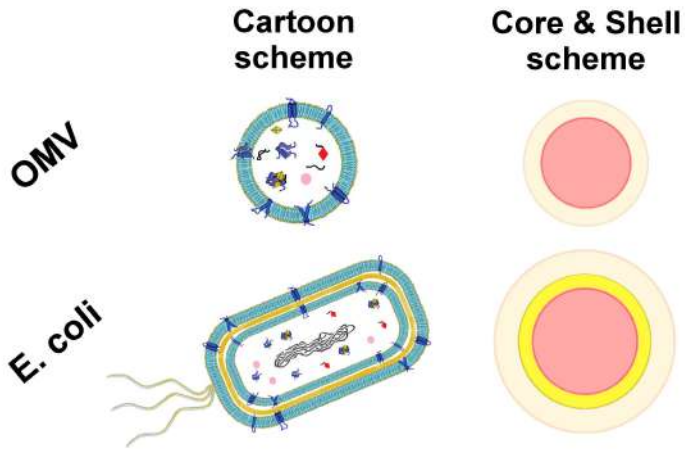

FIGURE 6.6: Outer membrane vesicle and E. coli bacterium schematization as core and shell of different densities (SAXS analysis) or different refractive index (scattering intensity simulations).

represented and modeled as shown in figure 6.6. In particular, OMVs have been

modeled as single-shelled spheres, where the core is the cytoplasm (assumed homogeneous) and the shell represents the lipid membrane, whereas in the case of E. coli also a second (internal) shell is added, which represents the cell wall, mainly composed of peptidoglycans. To take into account the thermotropic behaviour and evaluate the refractive index $n(T)$ of the lipid bilayer, we assumed the Boltzmann function dependence on the temperature (see equation 6.1) with the T_0 and ΔT values determined from experimental turbidimetric measurements. We also imposed the ratio of the asymptotic values of the refractive index ($\frac{n_0}{n_1}$) equal to the ratio of the measured intensities ($\frac{I_0}{I_1}$). Finally, we constrained the Boltzmann curve to assume the value of 1.44 at $T = 23°C$ according to the literature [102]. As to the refraction index of cytoplasm and peptidoglycan, for the sake of simplicity we neglect any temperature dependence assuming the constant values of 1.367 and 1.455 respectively. The results of the calculations obtained using MiePlot 4.6 simulator were reported in figure 6.7. In particular, figure 6.7a shows the transitions of OMV models, whereas figure 6.7b shows the corresponding curves calculated for the E. coli models. Notably, the simulations clearly confirmed not only the temperature-dependent

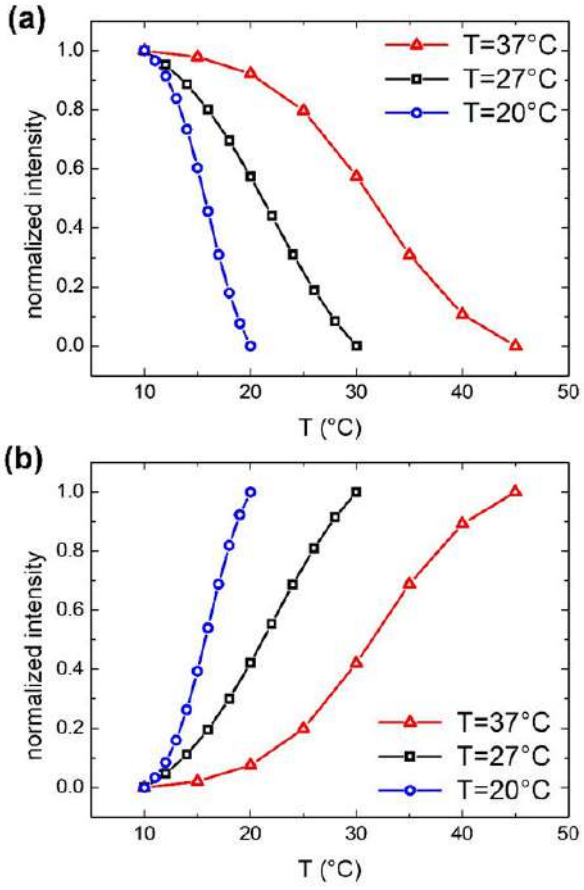

FIGURE 6.7: Normalized scattered intensity as a function of temperature: comparison between simulated membrane phase transitions of OMVs (a) and E. coli bacteria (b) grown at $37°C$, $27°C$ and $20°C$.

transition trend but also the opposite scattering intensity behaviour of OMVs and bacteria, as previously experimentally observed. Simulations gave us the possibility to identify the reason behind the transition differences observed in the case of OMVs and bacteria and ascribe this behaviour to the presence of a second "layer" beneath

the outer membrane (the cell wall comprising the peptidoglycan layer) with a fixed refractive index. In fact, this is the only difference between these two models (at least from the optical point of view). This strongly supports the hypothesis that the trend of the transition temperature represents a characteristic "fingerprint" of OMVs. This behaviour could be thus employed as a characteristic "marker" to distinguish vesicles from the bacteria that originated them.

Small Angle X-ray Scattering experiments on Gram-negative OMVs

To deeply investigate the temperature effects on OMVs structure, we performed SAXS experiments. Also in this case, we performed measurements on OMVs isolated by E.coli grown at three different temperatures but, due to the low concentration obtainable for vesicles grown at 27°C and 20°C, we obtained a signal sufficiently intense only for OMVs grown at 37°C. We reported SAXS patterns in figure

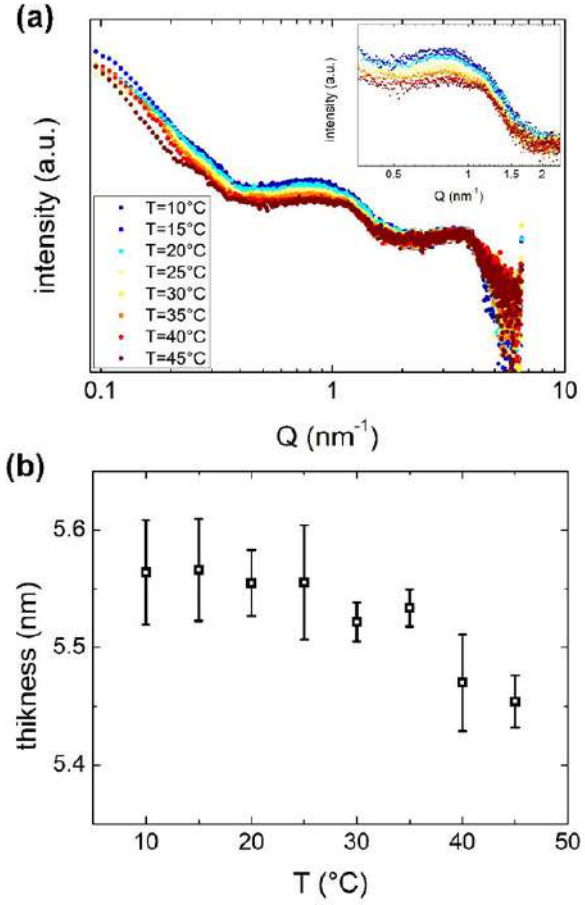

FIGURE 6.8: a) SAXS spectra corresponding to vesicles at temperatures between 10°C and 45°C. b) Vesicles bilayer thickness as resulting from SAXS data fitting procedure, as a function of temperature.

6.8a. The overall SAXS pattern, which is typical of shelled spheres, did not change significantly when the temperature increased. This evidence confirmed that OMVs size did not vary in the temperature range investigated and no membrane damages were reported. However, the smooth peak centered at $Q \approx 1\ nm^{-1}$ (inset of figure 6.8a) is related to the thickness of the membrane and has been already detected by

SAXS on Alix-positive exosome-like small extracellular vesicles [103]. This peak significantly changed the shape and moved towards higher Q values at increasing temperatures. In order to better understand the significance of this peak position shift, SAXS curves were analysed considering the simplified model of OMVs reported in figure 6.6. Although OMV membrane contains a mixture of different lipids, cholesterol, and proteins, this simple model appeared to be able to reasonably reproduce our SAXS data. The thickness and, the radius and the electron densities, as a function of temperature obtained from the fitting procedure are reported in figure 6.8b and 6.9, respectively. The thickness of the OMV membrane is the only parameter that

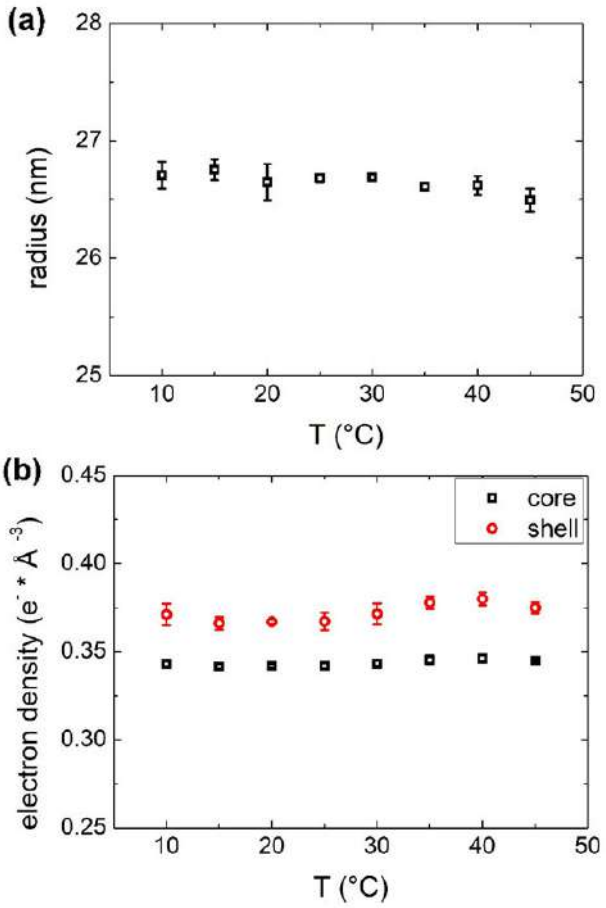

FIGURE 6.9: a) Vesicle radius as resulting from SAXS data fitting procedure, as a function of temperature. b) Vesicle core (black square) and shell (red circle) electron densities as resulting from SAXS data fitting procedure, as a function of temperature.

significantly changes as the temperature increases. This result confirms that vesicle size is not affected by temperature (at least in this range) and that vesicles remain intact, as indicated by the core electron density as well as the shell one. These findings suggest that temperature induces a rearrangement of membrane structural motifs, linked to the lipid membrane reorganization and/or to conformational changes of its components.

Turbidimetric experiment on Gram-positive MVs

In order to assess the feasibility of using the phase transition profile to discriminate extracellular vesicles coming from different bacteria (i.e., gram-negative and gram-positive bacteria) and potentially use this information for diagnostic purposes in the microbiology field, we also measured the phase transition properties of MVs from the gram-positive Lactobacillus rhamnosus LGG (LGG) compared to those obtained from the gram-negative E.coli. In this specific case, we studied only the phase transition of MVs from LGG by turbidimetric measurements, as this technique is easy to reproduce, does not require expensive equipment, is cheap and also relatively fast. In figure 6.10 (upper panel), we reported the results of the scattering intensity

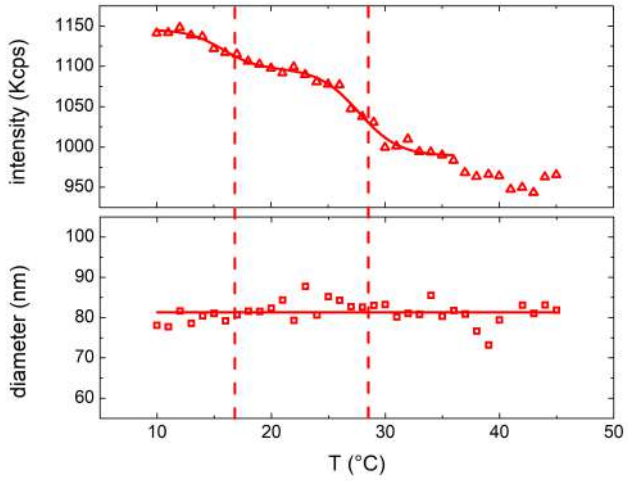

FIGURE 6.10: Mean scattered intensity (upper panel) and hydrodynamic diameter (lower panel)of a DLS measurement at increasing temperatures between $10°C$ and $45°C$ of vesicles by Lactobacillus Rhamnosus grown at $37°C$.

measurements in the temperature range between $10°C$ and $45°C$. By examining the profile of MVs from LGG, we observed the presence of multiple transitions, two of them at a $T < 35°C$ and probably another one less clear around $37°C$. DLS analysis confirmed that the diameter remained constant (as show in figure 6.10 (lower panel)) throughout all the temperature range. Similarly to what observed for OMVs, flocculation or precipitation of MVs did not occur, confirming that the transitions are only related to membrane modifications. The intensity data were fitted with a double Boltzmann function in the region at $T < 35°C$, providing two transition temperatures of $16 \pm 2°C$ and $28 \pm 3°C$. Interestingly, the scattering profile of MVs was completely different than that of OMVs, suggesting that MVs and OMVs have a different lipid composition of the membrane.

The analysis of mean scattering intensity as a function of the temperature has shown the presence of peculiar membrane phase transitions characteristic of both OMVs and bacteria. In particular, the transition temperature that we measured allowed to discriminate not only vesicles of different composition (i.e., OMVs and MVs) but also to correlate them to bacteria that originated them and to their culture conditions (i.e., temperature). The results have shown that it is possible to distinguish vesicles coming from different bacteria (i.e., gram-positive and gram-negative bacteria) by simply studying the phase transitions of their membranes. In a close

future, by implementing this technique, it could be possible to perform microbiological analysis by discriminating different bacteria in complex mixtures or matrices (i.e., biological fluids, stool, blood, tissues, etc.) More generally, this technique could be also employed in fields such as oncology, for example to discriminate human exosomes originating from tumors from that produced by normal cells and help clinicians to diagnose different form of tumors.

Thanks to the wavelength extension carried out in this last period, and to the development of the new balanced measurement method, we are currently able to performe LTS measurements on the OMVs. In particular, we plan to measure the radius and the concentration of OMVs across the transition. In such a way, we expect to evidanziate the membrane refractive index modification during the transition and estimate their temperature dependence. At present, preliminary measurements are underway.

Conclusions

This thesis is based on the design, realisation and testing of an apparatus for Laser Transmission Spectroscopy (LTS), a novel technique based on the analysis of the light intensity transmitted by a particle suspension as a function of the incident radiation wavelength. FORTRAN and LabView codes were properly developed for the data acquisition and analysis. Eventually, the LTS apparatus has been used for the determination of particle radii and absolute concentrations in different systems.
The core of the apparatus that has been designed and realised is a pulsed Nd:YAG tunable laser (emission wavelength in the range $410nm < \lambda < 2600nm$). The whole optical system is able to produce two identical beams: the first impinges on the sample, i.e. particles + solvent, the second on the solvent only.

The detection system, which simultaneously analyses the two beams in order to obtain the particle transmittance, is based on two Si photodiodes whose output voltage pulses are the input signals of a two channel variable gain lock-in amplifier. At first, the apparatus was realized following the seminal work of Li et al.. With this *conventional* setup, different series of measurements have been carried out on several systems obtaining rather good results. Although the estimation of the absolute concentration results to be accurate and rather robust, test measurements performed on standard polystyrene nanoparticles of different size and concentration showed significant inaccuracies. In particular, the width of the size distributions, relevant for the characterisation of suspensions, was partly uncontrolled, due to the strong dependence of the analysis on the experimental errors. To overcome this drawback, we developed an innovative lock-in amplifier for the detection of the photodiode voltage pulses. Standard techniques for small-signal detection indeed typically employ lock-in amplifiers whose sensitivity and resolution are limited by the selected full-scale. These characteristics maximise the apparatus sensitivity and resolution respect to the small amplitude variations of the input signal. In particular, we designed a new, highly performant, variable gain, lock-in amplifier that has been optimised to operate at the repetition rate and pulse duration of our laser, so allowing to detect small changes in the input signal amplitudes.
In order to increase the signal-to-noise ratio of the transmission spectra, has been implemented an innovative *balanced* measurement method, based on a calibration procedure, in which the gain of the new homemade lock-in amplifier is tuned, for each wavelength, to balance the transmitted intensity in both the optical paths of the experimental setup. The collected gain values are then employed to obtain the sample transmittance, and the related extinction coefficient, from the ratio between the two measured intensities. In this new balanced method, the error propagation is greatly reduced, thus obtaining a huge improvement in the distribution quality, in terms of both width and shape, and reliable and accurate estimates of the radii and absolute concentration of the samples under investigation.

Size and absolute concentration LTS measurements have been performed on sample belonging to three different fields: pharmaceutics, biophysics and cultural-heritage. In particular, the study of liposomes for drug delivery showed that LTS is

very useful to measure the liposome concentration, regardless of the lipid composition. This capability represents an *unicum* among the techniques applied in this field at present. The results of this study are reported in a paper to be submitted to an international journal.

LTS has also been applied to determine the absolute concentration of microvesicles derived from Microglia cells. This kind of study is, in principle, relevant for developing a new strategy for a proper cancer therapy. As a matter of fact, microvesicles, stimulated with different molecules, were employed for both *in vivo* and *in vitro* experiments, with the aim of studying the modifications induced in the glioma cell response, in terms of cell movement and proliferation. In particular, the measured concentration of the stimulated microvesicles allowed to conclude that the number of microvesicles per cell is almost the same, regardless the specific molecular treatment, and the response of the microvesicles stimulated is effectively due to the transfer of their cargo of mRNA to recipient glioma cells. These results are recently published in an international journal [48].

LTS technique has been also applied for the optimisation of the synthesis of silica nanocapsules used as biocide containers for stone artwork preservation. The nanocapsule synthesis procedure involves the dripping of the silicon oxide precursor in a constantly stirred water bath. In particular, the quality of silica nanocapsules results influenced by the dripping and stirring speeds. To choose the best syntesis parametres, we performed LTS measurements on suspension of nanocapsules obtained at different stirring speeds. The obtained density concentrations, compared with the Dynamic Light Scattering (DLS) distributions and electron microscopy images, allowed to find the best stirring velocity and obtain nanocapsules of good quality.

The present performances obtained by the new balanced LTS measurement method could be of paramount importance for the study exosomes, one of the recent hot-topics in biology. Within this context, we carried out a preliminar characterisation of Outer Membrane Vesicles (OMVs), bacterial vesicles analogous to exosomes. This study, performed by DLS and Small Angle X-rays Scattering, showed interesting membrane properties, which relate vesicles with progenitor cells. The analysis of mean DLS intensity as a function of the temperature showed the presence of membrane phase transitions characteristic of both vesicles and bacteria. This allowed to discriminate vesicles of different composition and to correlate them to progenitor bacteria.
The implementation of a recognition technique for membrane phase transitions could, in principle, allow to perform microbiological analyses to discriminate different bacteria in complex mixtures, such as biological fluids, blood or tissues. In an optimistic view, this method could allow the discrimination of human exosomes produced by cancer cells from those ones by normal cells, in diagnostic application. The results of this study are reported in a recently submitted paper entitled *"Biophysical characterization of membrane phase transition profiles for the discrimination of Outer Membrane Vesicles (OMVs) from Escherichia coli grown at different temperatures"*.
In these last months, thanks to a new funding, we were able to extend the accessible laser wavelength range down to 210 nm. With this upgrade, we hope to reach higher performances both in terms of minimum size and in concentration. On these bases, we plan to perform LTS measurements on OMVs, around the transition temperature, to deeply characterise the membrane behaviour with particular attention to the

membrane refractive index variation. Presently, preliminary LTS measurements on these vesicles are in progress.

Appendix A

Appendix A: Microglia-derived microvesicles affect microglia phenotype in glioma

In this appendix we report the paper "Microglia-Derived Microvesicles Affect Microglia Phenotype in Glioma" published on February 2019 [48], in which our Laser Transmission Spectroscopy measurements were fundamental to discriminate the amount of microvesicle per cell injected in the different experiments, for microvesicle extracted by non stimulated BV2 cells and stimulated BV2 cells (with LPS/INFγ and IL4).

frontiers in Cellular Neuroscience

ORIGINAL RESEARCH
published: 22 February 2019
doi: 10.3389/fncel.2019.00041

Microglia-Derived Microvesicles Affect Microglia Phenotype in Glioma

Alfonso Grimaldi[1†], Carmela Serpe[2†], Giuseppina Chece[2], Valentina Nigro[3], Angelo Sarra[4], Barbara Ruzicka[3], Michela Relucenti[5], Giuseppe Familiari[5], Giancarlo Ruocco[1], Giuseppe Rubens Pascucci[1], Francesca Guerrieri[1], Cristina Limatola[6,7] and Myriam Catalano[2,7]*

[1] Center for Life Nanoscience, Istituto Italiano di Tecnologia@Sapienza, Rome, Italy, [2] Department of Physiology and Pharmacology, Sapienza University of Rome, Rome, Italy, [3] Department of Physics, Istituto dei Sistemi Complessi del Consiglio Nazionale delle Ricerche, Sapienza University of Rome, Rome, Italy, [4] Department of Science, University of Roma Tre, Rome, Italy, [5] Department of Anatomical, Histological, Forensic Medicine and Orthopedics Sciences, Sapienza University of Rome, Rome, Italy, [6] Department of Physiology and Pharmacology, Laboratory Affiliated to Istituto Pasteur Italia – Fondazione Cenci Bolognetti, Sapienza University of Rome, Rome, Italy, [7] IRCCS Neuromed, Pozzilli, Italy*

Extracellular-released vesicles (EVs), such as microvesicles (MV) and exosomes (Exo) provide a new type of inter-cellular communication, directly transferring a ready to use box of information, consisting of proteins, lipids and nucleic acids. In the nervous system, EVs participate to neuron-glial cross-talk, a bidirectional communication important to preserve brain homeostasis and, when dysfunctional, involved in several CNS diseases. We investigated whether microglia-derived EVs could be used to transfer a protective phenotype to dysfunctional microglia in the context of a brain tumor. When MV, isolated from microglia stimulated with LPS/IFNγ were brain injected in glioma-bearing mice, we observed a phenotype switch of tumor associated myeloid cells (TAMs) and a reduction of tumor size. Our findings indicate that the MV cargo, which contains upregulated transcripts for several inflammation-related genes, can transfer information in the brain of glioma bearing mice modifying microglial gene expression, reducing neuronal death and glioma invasion, thus promoting the recovery of brain homeostasis.

Keywords: microglia, extracellular vesicles, tumor associated myeloid cells, brain tumors, glioma

OPEN ACCESS

Edited by:
Cinzia Volonté, Institute of Cell Biology and Neurobiology, CNR, Italy

Reviewed by:
Marta Fumagalli, University of Milan, Italy
Federica Barbieri, Università di Genova, Italy

***Correspondence:**
Cristina Limatola
cristina.limatola@uniroma1.it

[†] These authors have contributed equally to this work

***Received:** 24 October 2018*
***Accepted:** 25 January 2019*
***Published:** 22 February 2019*

Citation:
Grimaldi A, Serpe C, Chece G, Nigro V, Sarra A, Ruzicka B, Relucenti M, Familiari G, Ruocco G, Pascucci GR, Guerrieri F, Limatola C and Catalano M (2019) Microglia-Derived Microvesicles Affect Microglia Phenotype in Glioma. Front. Cell. Neurosci. 13:41. doi: 10.3389/fncel.2019.00041

INTRODUCTION

Cellular communication has been recently enriched by a new mechanism, that use the cargo transported by extracellular membrane vesicles (EVs). EVs include exosomes (Exo, 10–100 nm diameter), microvesicles (MV, 100–1000 nm) and apoptotic "blebs" (1–2 mm). EVs are produced by all cell types and their production dynamically changes in number and content in response to specific environmental signals. The content of EVs, considered true metabolic units, is released into the cytoplasm of receiving cells, where they mediate several functional effects (Iraci et al., 2017).

In the brain, EVs modulate synaptic activity and neuronal communication (Korkut et al., 2013; Chivet et al., 2014), and also contribute to spreading disease in several CNS pathologies, such as multiple sclerosis (Carandini et al., 2015), Alzheimer's disease (Aguzzi and Rajendran, 2009; Gouwens et al., 2018), prion disease (Fevrier et al., 2004), and Huntington's disease (Zhang et al., 2016). Neurocentric vision in acute and chronic diseases of the CNS turned out to be insufficient to explain the mechanisms responsible for several disease onset and progression. The role played by

non-neuronal cells, such as astrocytes and microglia, which are in constant communication with neurons to monitor brain parenchyma through their processes, actively contribute to maintain cerebral homeostasis.

EVs released by microglia, similarly to EVs released by macrophages, recapitulate, in their cargo, the inflammatory information of the donor cell (Garzetti et al., 2014; Cunha et al., 2016).

Microglial cells acquire a dysfunctional phenotype in many CNS pathologies, losing their ability to monitor and preserve brain homeostasis. In the context of glioma, tumor associated myeloid cells (TAMs) modify their phenotype and local microenvironment toward a pro-tumor, anti-inflammatory state supporting tumor cell proliferation, survival, and invasion (da Fonseca and Badie, 2013).

In this work, we investigated the role of MV released by polarized microglia on the modulation of microglia state *in vivo*, to verify the hypothesis to use MV to help host microglia to reacquire a homeostatic state in the context of glioma. At this aim EVs, and in particular microvesicles (MV) and exosomes (Exo) released by microglia in inflammatory conditions were isolated and analyzed for their *in vitro* and *in vivo* effects in glioma bearing mice. We demonstrated that *in vitro*, microglia derived LPS/IFNγ-MVs reduced the expression of anti-inflammatory genes in IL4-treated microglia. *In vivo*, LPS/IFNγ-MVs injected in the brain of mice with glioma reduced the anti-inflammatory phenotype of TAMs and significantly reduced tumor size and tumor induced neurotoxicity. We suggest that the cargo of LPS/IFNγ-MV, which contains specific mRNA for inflammatory genes, transfer this information to recipient cells modifying their gene expression profile toward a protective one. Altogether, these findings demonstrate that the administration of exogenous EVs could be a valuable approach to transfer protective signals to TAMs, restoring the homeostatic microglia phenotype.

RESULTS

Dimensional and Morphological Analyses of EVs Derived From Microglia

EVs, in particular microvesicles (MV) and exosomes (Exo), were obtained from BV2 cell line and primary mouse microglia. EV sizes were measured by Dynamic Light Scattering (DLS) performed at a constant temperature of 15°C. The CONTIN distribution demonstrated that BV2-derived MV (**Figure 1A**) had a polydispersity of 20%. The intensity-weighted distribution of hydrodynamic diameter shows that the main population peaked around 300 nm, providing 90% of the total scattered intensity, as evidenced by the integral of the distribution reported in the inset of **Figure 1A**. In MV released by primary microglia (**Figure 1B**) a polydispersity of 30–40% was obtained and two main populations were identified: the first peaked at 250 nm and the second at 880 nm. The distribution integral (inset of **Figure 1B**) highlights that 20% of the total scattered intensity is due to the smallest population, while 50% is due to the largest one. Exo had a polydispersity around 30–40%. Due to their size, the volume-weighted is the most accurate distribution to obtain qualitative information on sample composition. Seventy percent of Exo has a mean size of 34 ± 4 nm (derived from BV2 cells, **Figure 1C**) and of 39 ± 4 nm (derived from primary microglial cells, **Figure 1D**), while larger aggregates provide little contribution to the volume-weighted distribution, as evidenced in the insets of **Figures 1C,D**. For both populations there is a 30% of contribution to the overall scattered intensity due to larger aggregates.

EVs derived from BV2 cells were analyzed at the transmission electron microscopy: data shown in **Figure 1E** identify the typical round vesicle morphology and underlined a scattered composition in size, with the presence of aggregates (**Figure 1E**), that confirmed DLS data above reported.

MV Derived From Microglia Treated With LPS/IFNγ Reduce Migration and Invasion of GL261 Glioma Cells and Are Neuroprotective Against Glioma Excitotoxicity *in vitro*

Cultured primary microglia and BV2 cells were treated with LPS/IFNγ or IL 4. We previously verified microglia polarization by mRNA analysis (Grimaldi et al., 2016); we confirmed these data showing that LPS/IFNγ-treated cells increased NO release and that IL-4-treated cells increased Arg1 expression and activity (**Supplementary Figure S1** and related **Supplementary Methods**). Quantification of MV released by control (C-MV), LPS/IFNγ-treated (LPS/IFNγ-MV), and IL4-treated BV2 cells (IL4-MV) was measured by Laser Transmission Spectroscopy (LTS) (Li et al., 2010). LTS measurements showed that the number (N) of MV/cell in these three conditions was not significantly different (**Figure 2A**). MV were then tested to verify their ability to interfere with glioma cell migration and proliferation. Data shown in **Figure 2B** illustrate that GL261 migration was impaired by LPS/IFNγ-MV, while GL261 migration increased upon IL 4-MV treatment, at 24 and 48 h. In contrast, neither LPS/IFNγ-Exo nor IL 4-Exo (released by primary microglia) affected GL261 migration (**Supplementary Figure S2**). Based on these results, for successive experiments we decided to focus our interest only on the effect of MV. Similarly to migration, results obtained on CXCL12-induced GL261 invasion, demonstrated inhibitory effects of LPS/IFNγ-MV and no effects of IL 4-MV (**Figure 2C**). Note that basal GL261 invasion was significant reduced in the presence of LPS/IFNγ-MV and was significant enhanced in the presence of IL 4-MV. These data indicate that microglia-derived MVs modulate glioma cell movement and invasion.

To investigate the effect of MV on glioma cell viability and proliferation, MTT assay and BrdU staining were performed. Results reported in **Figure 2D** show that neither LPS/IFNγ-MV nor IL 4-MV directly modulate GL261 viability, at 24, 48, 72, or 96 h. Similarly, no changes in proliferation rate were induced by LPS/IFNγ-MV or by IL 4-MV, measured by bromodeoxyuridine (BrdU) staining after 24 h (**Figure 2E**) and 48 h (data not shown). To investigate whether microglia-derived MV could exert indirect effects on glioma, cells were co-cultured with a mixed neuroglia culture in the presence of LPS/IFNγ-MV, for 18 h: in these conditions a reduction of GL261 viability was

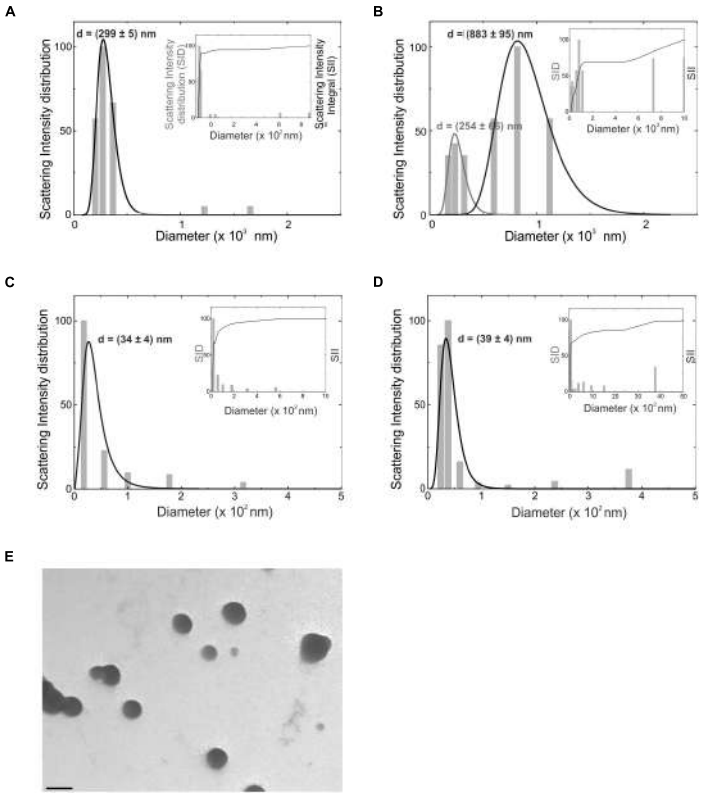

FIGURE 1 | Hydrodynamic diameter distribution (d) as obtained from CONTIN analysis of the intensity autocorrelation curves, for microvesicles obtained from BV2 microglia cell line **(A)** and from primary murine microglia **(B)**, for exosomes from BV2 **(C)** and primary microglia **(D)**, reported as intensity-weighted distribution. The overall normalized integral of the distribution is also reported in the inset of the relative panels (SID, scattering intensity distribution; SII, scattering intensity integral). Gray lines are fits through Log-normal distribution. **(E)** Transmission electron microscopy of EVs derived from BV2 cells. Bar = 100 nm, direct magnification 40000×, print magnification 213000×.

observed (**Figure 2F**), indicating an indirect effect of MV on glioma cell viability. In these same co-culture experiments, we also analyzed the effect of MV on neuron survival and observed (**Figure 2G**) that LPS/IFNγ-MV counteracted GL261-induced neurotoxicity, while IL 4-MV were ineffective.

Microglia-Derived LPS/IFNγ-MV Reduce Tumor Size in Mice

The above reported data prompted us to investigate the effect of LPS/IFNγ-MV in a mouse model of glioma. At this aim, GL261 cells were brain injected in the striatal region of the right hemisphere and, after 7 and 14 days, primary microglia-derived MV were infused in the tumor region via an implanted cannula. Fifteen days after tumor injection (**Figure 3**) LPS/IFNγ-MV treated mice had a significant reduction of tumor size while mice treated with IL 4-MV significantly increased the size of their brain tumors. Similar results were obtained with BV2-derived MV (**Supplementary Figure S3**). To investigate whether these effects on tumor size were mediated by alterations of GL261 cell proliferation, mice treated as in **Figure 3** were given BrdU

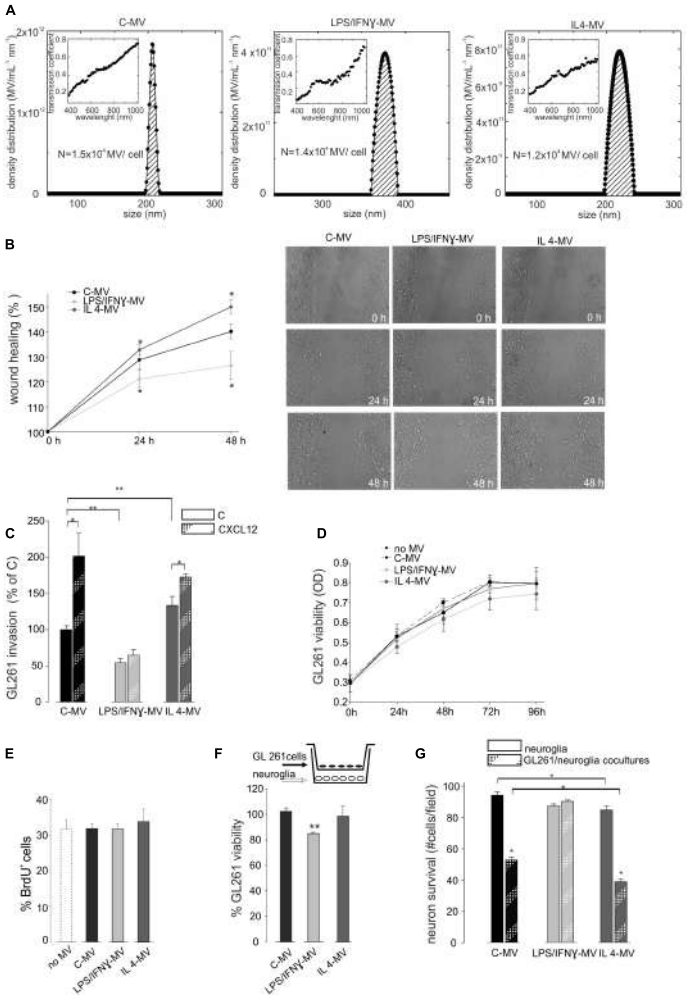

FIGURE 2 | (A) Density distribution of BV2-derived MVs, together with the transmission coefficient as a function of the wavelength (inset). The integral of the density distribution showed the number of MV per ml. Normalizing, the number of vesicles produced by each cell in control condition is $N = 1.5 \times 10^4$ (C-MV), with LPS/IFNγ is $N = 1.4 \times 10^4$ (LPS/IFNγ-MV), with IL4 is $N = 1.2 \times 10^4$ (IL4-MV). **(B)** GL261 glioma cells were treated with MV obtained from untreated microglia (C-MV), microglia treated with LPS/IFNγ (LPS/IFNγ-MV) and IL 4 (IL 4-MV) and a wound healing assay was performed. GL261 migration was measured 24 and 48 h after treatment, data are expressed as mean percentage of wound healing area ± SE, $N = 4$, $^*P < 0.001$ vs. C-MV (one way analysis of variance, Holm-Sidak method). On the right, representative wound healing assay on GL261 cells at 0 h and after 24 and 48 h of C-MV, LPS/IFNγ-MV and IL 4-MV treatment. **(C)** GL261 cells were assayed for basal invasion **(C)** and CXCL12-induced invasion in presence of MV obtained from untreated microglia (C-MV), microglia treated with LPS/IFNγ

(Continued)

FIGURE 2 | Continued
(LPS/IFNγ-MV) and IL 4 (IL 4-MV) in a Boyden chamber system. GL261 invasion was measured as mean percentage ± SE, $N = 4$; $^{*}P < 0.05$ and $^{**}P < 0.001$ (one way analysis of variance, Holm-Sidak method). **(D)** GL261 cells were assayed for cell viability without MV (no-MV), in presence of MV obtained from untreated microglia (C-MV), microglia treated with LPS/IFNγ (LPS/IFNγ-MV) and IL 4 (IL 4-MV) by MTT analysis. Cells were analyzed 0, 24, 48, 72, and 96 h after plating. Viability was reported in optical density (OD) mean ± SE, $N = 4$; no statistical significance vs. C-MV (one way analysis of variance, Holm-Sidak method). **(E)** GL261 cell proliferation was measured as % mean ± SE of $BrdU^{+}$ GL261 cells untreated (no-MV), treated with MV obtained from untreated microglia (C-MV), microglia treated with LPS/IFNγ (LPS/IFNγ-MV) and IL 4 (IL 4-MV) for 24 h, $N = 4$, no statistical significance vs. C-MV (one way analysis of variance, Holm-Sidak method). **(F)** GL261 cells, co-cultured with hippocampal neuroglial cultures (as depicted in the inset) were treated for 18 h with MV obtained from untreated microglia (C-MV), microglia treated with LPS/IFNγ (LPS/IFNγ-MV) and IL 4 (IL 4-MV), were analyzed for viability by trypan Blue staining. Data are expressed as number of viable cells/field ± SE, $N = 3$; $^{**}P < 0.05$, Student's *t*-test. **(G)** Hippocampal neuroglial cultures alone or co-cultured with GL261 cells (as depicted in the inset of panel **F**) were treated with MV obtained from untreated microglia (C-MV), microglia treated with LPS/IFNγ (LPS/IFNγ-MV) and IL 4 (IL 4-MV) for 18 h and were analyzed for neuronal viability. Data are expressed as number of viable cells/field ± SE, $N = 3$, $^{*}P < 0.001$, Student's *t*-test.

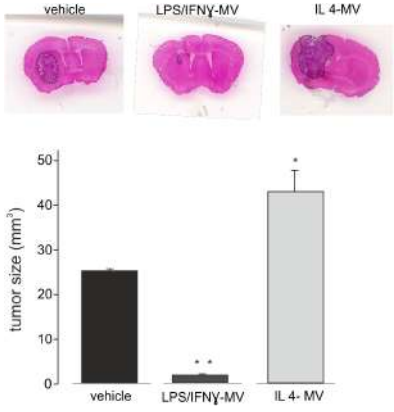

FIGURE 3 | Tumor size in the brain of GL261-bearing mice treated with vehicle or MV obtained from microglia treated with LPS/IFNγ (LPS/IFNγ-MV) and IL 4 (IL 4-MV). Tumor size (in mm^3) was reported as mean ± SE, $N = 7$/experimental group, $^{*}P < 0.05$, $^{**}p \leq 0.001$ vs. vehicle, Student's *t*-test. On the top, representative coronal brain sections of GL261-bearing mice treated as above, stained with hematoxylin-eosin; tumor area in the dashed line.

2 h before euthanasia. Quantification of BrdU-labeled cells, normalized for tumor area, revealed a significant reduction of cell proliferation in the tumoral region (**Figure 4A**) of LPS/IFNγ-MV treated mice. Treatment with LPS/IFNγ-MV also reduced glioma cell migration *in vivo*, as reported in **Figure 4B**, where tumor cell invasion was calculated as the number of cells protruding more than 150 μm from the main tumor mass. In the peritumor region, we evaluated neuronal death by Fluoro Jade staining, comparing mice treated with LPS/IFNγ-MV with control mice. Data shown in **Figure 4C** demonstrate that neuronal death was significant reduced in LPS/IFNγ-MV treated mice, demonstrating *in vivo* a neuroprotective effect of LPS/IFNγ-MV against tumor-induced excitotoxicity.

All these data demonstrated that LPS/IFNγ-MV carry anti-tumor information that are effective in reducing tumor size *in vivo*.

Microglia-Derived LPS/IFNγ-MVs Modify the Phenotype of Tumor-Associated Microglia

To understand the mechanisms of action of the injected MVs, we first decided to investigate their cellular localization upon brain injection. At this aim, MVs derived from primary microglia, were stained with the membrane-selective dye PKH26 and brain injected in glioma bearing mice. Cerebral slices obtained from the tumoral region show the presence of PKH26-MV on both $Iba1^{-}$ and $Iba1^{+}$ cells (**Figure 5A**). We never observed PKH26 staining outside the tumor area. It is known that a high amount of tumor associated microglia/macrophages (TAMs) are present in glioma, and may represent up to 50% of tumor mass (Hambardzumyan et al., 2016). TAMs exert tumor supporting function releasing factors that facilitate tumor proliferation and migration (Fonseca et al., 2012). We wonder whether the interaction of MVs with TAMs could modulate their pro-tumor activity, and investigated the effect of LPS/IFNγ-MV on gene expression of $CD11^{+}$ cells isolated from the brains of glioma-bearing mice. As shown in **Figure 5B**, the expression of *arg1*, *cd163*, *cd206*, *fizz1*, and *ym1* genes all correlated with an anti-inflammatory, pro-tumor phenotype, were up-regulated in $CD11b^{+}$ cells in the ipsilateral hemisphere of glioma bearing mice and were significant reduced upon LPS/IFNγ-MV treatment (with the exception of *fizz1*). Similar modulatory effects were observed *in vitro*: as shown in **Figure 5D**, LPS/IFNγ-MV (derived from primary microglia) significant reduced the microglial expression of all analyzed genes (*arg1*, *cd163*, *cd206*, *ym1*, and *fizz1*) except *ym1*, indicating a direct modulation likely induced by MV cargo that enter microglia also *in vitro* (**Figure 5C**).

All these data suggest that LPS/IFNγ-MVs might directly signal to microglia and instruct these cells toward an antitumor phenotype.

mRNA Analyses of Microglia-Derived LPS/IFNγ-MV

To investigate the nature of the cargo transported by LPS/IFNγ-MV that could help the understanding of the above described mechanisms, the mRNA content of MVs

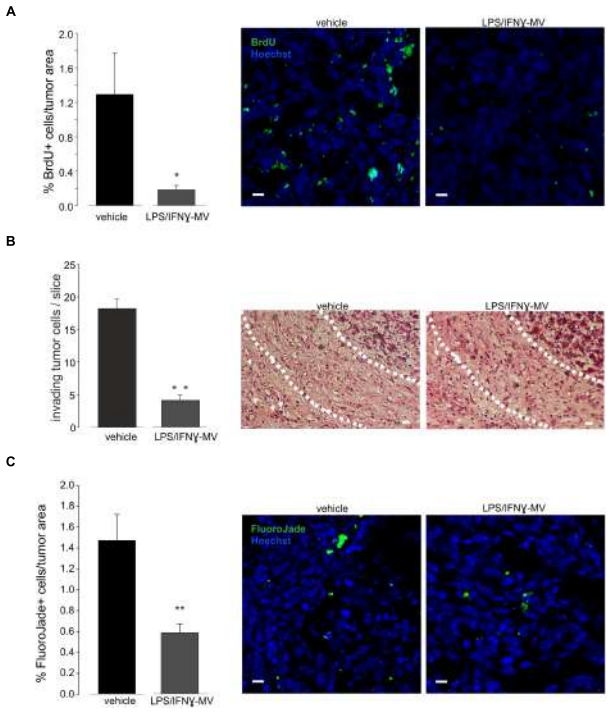

FIGURE 4 | (A) Cell proliferation, measured as BrdU$^+$ cell area/tumor area in GL261-bearing mice treated with vehicle or MV obtained from microglia treated with LPS/IFNγ (LPS/IFNγ-MV), data are expressed as mean percentage ± SE, $N = 3$, $^{**}P \leq 0.001$ vs. vehicle, Student's *t*-test. On the right: representative immunofluorescence on coronal brain slices of GL261-bearing mice treated as above (BrdU in green; Hoechst in blue), scale bars, 20 μm. **(B)** Glioma cells invading the brain parenchyma for more than 150 μm beyond tumor border 17 days after glioma cell transplantation in GL261-bearing mice treated with vehicle or MV obtained from microglia treated with LPS/IFNγ (LPS/IFNγ-MV), data are expressed as mean cell number ± SE, $N = 3$/experimental group, $^{**}P \leq 0.001$, Student's *t*-test vs. vehicle. On the right, representative brain peritumoral sections stained with haematoxylin/eosin; white arrows indicate glioma cells invading the brain parenchyma beyond the main tumor border for more than 150 μm (dashed line); scale bars, 20 μm. **(C)** Neuronal death, measured as Fluoro Jade$^+$ cells/tumor area in GL261-bearing mice treated with vehicle or MV obtained from microglia treated with LPS/IFNγ (LPS/IFNγ-MV), data are expressed as mean percentage ± SE, $N = 3$, $^{**}P \leq 0.001$ vs. vehicle, Student's *t*-test. On the right: representative immunofluorescence on coronal brain slices of GL261-bearing mice treated as above (Fluoro Jade in green; Hoechst in blue), scale bars, 20 μm.

released by primary microglia was analyzed by NanoString chip for the expression of 243 key inflammation-related genes and compared with MVs released by control, unstimulated microglia. As shown on **Figure 6A**, 18 genes were significantly up-regulated in LPS/IFNγ-MV. Data were confirmed by RT-PCR for *tnf*-α and *il1b* genes (**Figure 6B**), validating the immune panel system.

Pathway analysis, performed on the 10 most significant functional categories defined by the Gene Ontology Biological process (**Figure 6C**) indicated that LPS/IFNγ-MV contain 12% of genes involved in inflammatory responses (*c3*, *ccl4*, *ccl5*, *cxcl2*, *cxcl9*, *tnf*, *ptgs2*, *ccl7*, *il1b*, *ccl2*, *ccl3*, *il1rn*, *hif1a*), 14% of genes involved in defense responses (*irf7*, *c3*, *ccl4*, *ccl5*, *cxcl2*, *cxcl9*, *tnf*, *ptgs2*, *mx1*, *ccl7*, *il1b*, *ccl2*, *ccl3*, *il1rn*, *hif1a*), 12% of genes involved in responses to wounding (*c3*, *ccl4*, *ccl5*, *cxcl2*, *cxcl9*, *tnf*, *ptgs2*, *ccl7*, *il1b*, *ccl2*, *ccl3*, *il1rn*, *hif1a*), 12% of genes involved in immune responses (*irf7*, *c3*, *ccl4*, *ccl5*, *cxcl2*, *cxcl9*, *tnf*, *mx1*, *ccl7*, *il1b*, *ccl2*, *ccl3*, *csf3*), 4% of genes involved in regulation of natural killer cell chemotaxis (*ccl7*, *ccl4*, *ccl3*, *ccl2*, *ccl5*), 8% of genes involved in positive regulation of response to external stimuli (*c3*, *ccl4*, *ccl5*, *tnf*, *ccl7*, *ptgs2*, *il1b*, *ccl2*, *ccl3*), 10% of genes involved in regulation of cytokine production (*irf7*, *c3*, *ccl4*, *ccl5*, *tnf*, *ptgs2*, *il1b*, *ccl2*, *ccl3*, *hif1a*, *cebpb*), 13% of genes involved in immune system process

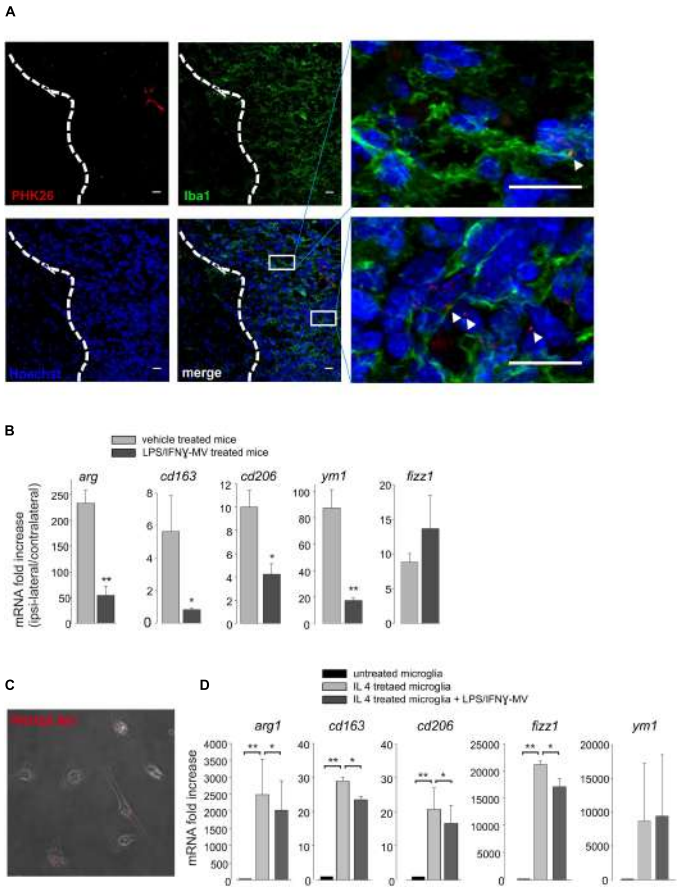

FIGURE 5 | (A) Immunofluorescence analysis for Iba1 (in green) of coronal brain sections from GL261-bearing mice treated with PKH26-stained MV (in red; Hoechst in blue) obtained from microglia. Tumor region at the right of the dashed line. In the merge, identification of two tumor regions shown at higher magnification. Scale bar: 20 μm **(B)** RT-PCR of anti-inflammatory genes (*arg1*, *cd163*, *cd206*, *ym1*, and *fizz1*) in CD11b$^+$ cells extracted from brains of GL261-bearing mice treated with vehicle or MV obtained from microglia treated with LPS/IFNγ (LPS/IFNγ-MV). Data are the mean ± SE of fold increase (normalized vs. contralateral cerebral hemisphere of each animal; gene expression was normalized vs. *gapdh*), $N = 5$, $^{**}P < 0.001$, $^{*}P < 0.05$ vs. vehicle treated mice, Student's *t*-test. **(C)** Merged of bright and fluorescence fields of microglia treated with IL 4 and incubated with PKH26-stained MV (in red) obtained from LPS/IFNγ-treated microglia. **(D)** RT-PCR on mRNAs of untreated or IL 4-treated microglia incubated with or without MV obtained from LPS/IFNγ-treated microglia, and analyzed for the expression of anti-inflammatory genes (*arg1*, *cd163*, *cd206*, *fizz1*, and *ym1*). Data are the mean ± SE of fold increase (normalized vs. *gapdh*), $N = 3$, $^{**}P < 0.001$, $^{*}P < 0.05$, Student's *t*-test.

(*irf7*, *c3*, *ccl4*, *ccl5*, *cxcl2*, *cxcl9*, *tnf*, *mx1*, *ccl7*, *il1b*, *ccl2*, *ccl3*, *hif1a*, *csf3*), 8% of genes involved in positive regulation of cytokine production (*irf7*, *c3*, *ccl4*, *ccl5*, *tnf*, *ptgs2*, *il1b*, *ccl3*, *hif1a*), and 7% of genes involved in leukocyte migration (*ccl4*, *ccl5*, *cxcl2*, *tnf*, *ccl7*, *il1b*, *ccl2*, *ccl3*). These data demonstrated that the MV mRNA content is highly complex, covering genes coding for proteins

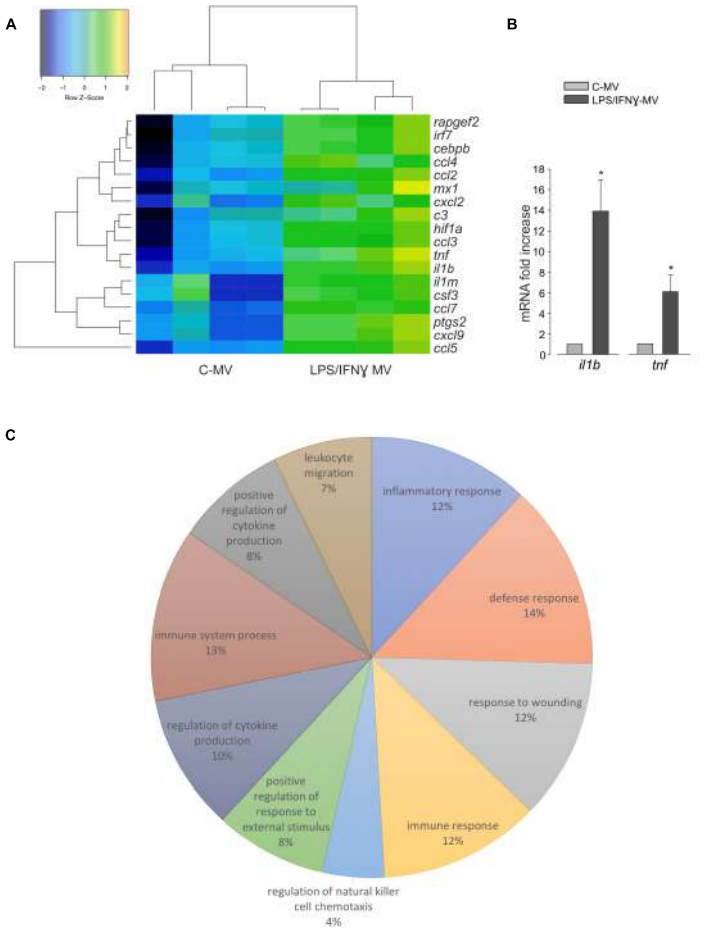

FIGURE 6 | (A) mRNAs isolated from MV released by untreated microglia (C-MV) or microglia treated with LPS/IFNγ (LPS/IFNγ-MV) were analyzed by NanoString. Heat map analysis of NanoString data show hierarchical clustering of 18 differentially expressed genes between C-MV and LPS/IFNγ-MV, $N = 4$. The signals were normalized and transformed to the log2 scale. The color scale indicates the gene expression standard deviations from the mean, with black/blue for low expression and green/orange for the high expression levels. Eighteen genes (listed on the right) were considered significant because with at least 2.8-fold changes with $P < 0.05$ (Wilcoxon test) at the 95% confidence level. Dendrograms illustrate the relationship-distance between samples and genes. **(B)** RT-PCR on mRNAs isolated from MV derived from untreated microglia (C-MV) or microglia treated with LPS/IFNγ (LPS/IFNγ-MV) analyzed for the expression of *il1b* and *tnf* genes. Data are the mean ± SE of fold increase (normalized vs. *gapdh*), $N = 3$, $^*P < 0.05$, Student's *t*-test vs. C-MV. **(C)** The pie chart illustrates the distribution of the 18 differentially expressed genes across the 10 most significant functional categories defined by the Gene Ontology Biological process. The percentage numbers represent the frequency of genes in each category. Data were analyzed using FIDEA tool.

related to different pathways of the inflammatory process, and that their delivery to TAM might contribute to re-activate the immune response, which oppose glioma growth.

MATERIALS AND METHODS

Primary Brain Cells Cultures

Neuroglial cultures were prepared from 0- to 2-day-old (p0–p2) C57BL/6N mice as already described (Lauro et al., 2010); neurons-astrocytes-microglia ratio is 60-35-5%. Microglia cultures were obtained as already reported (Grimaldi et al., 2016) and were 98% Iba1$^+$ positive (Lauro et al., 2010).

Cell Lines

BV2 murine microglial cells and GL261 murine glioma cells were cultured in DMEM supplemented with 10–20% heat-inactivated FBS, 100 IU/ml penicillin G, 100 μg/ml streptomycin, 2.5 μg/ml amphotericin B and grown at 37°C in a 5% CO_2 and humidified atmosphere.

Microglia Stimulation (Polarization)

Primary microglia and BV2 cells were treated for 24 hours with IFN-γ (20 ng/ml) and LPS (100 ng/ml), or with IL-4 (20 ng/ml) or with EVs.

Extraction of EVs

Cytokine-treated microglia were stimulated for 30 min with ATP (1 mM) in KRH (125 mM NaCl; 5 mM KCl; 1.2 mM $MgSO_4$; 1.2 mM KH_2PO_4; 2 mM $CaCl_2$; 6 mM D-glucose; 25 mM HEPES/NaOH, pH = 7.4). Cell supernatant was collected and centrifuged at 800 *g* for 5 min to remove cell debris. The obtained supernatant was centrifuged at 10000 *g* for 30 min at 4°C and the resulting pellet, containing MVs, was re-suspended in KRH buffer for DLS, LTS and transmission electron microscopy, in PBS for *in vivo* experiments or in serum-free DMEM for microglia stimulation, MTT, wound healing and BrDU proliferation assays. Remaining supernatant underwent ultracentrifugation at 100,000 *g* for 1-h at 4°C. The Exo, present in this second pellet, were re-suspended in KRH buffer for DLS measures and in serum free DMEM for wound healing assay. The same protocol permits to eliminate EVs from the medium used to re-suspend MVs and Exo and guarantees that the EVs obtained only derived from polarized microglial cells. In some experiments, EVs were labeled with PKH26, a lipophilic membrane red fluorescent dye (PKH26 GL-1KT, Sigma-Aldrich) according to manufacturer protocol. Briefly, PKH26 dye was re-suspended in diluent C to a final concentration of 0.6 μM (dye solution). MV were re-suspended in 500 μL of dye solution and incubated for 5 min, while mixed with gentle pipetting. Excess dye was bound with 500 μL EVs-depleted bovine serum albumin (1%, Sigma-Aldrich). MV pellet, obtained by centrifugation (10000 × *g*, 30 min, 4°C) was washed twice in PBS. PKH26-stained MV were re-suspended in PBS for *in vivo* administration and in serum-free DMEM for *in vitro* treatment. In all the experiments, the same procedure of staining minus MV was performed as control condition.

Dynamic Light Scattering and Data Analysis

Dynamic light scattering (DLS) measurements were performed using a standard optical setup. The monochromatic and polarized beam emitted from a He-Ne laser (10 mW at λ = 632.8 nm) was focused on the sample placed in a capillary of 2 mm of diameter positioned in a cylindrical VAT for index matching and temperature control. The scattered intensity was collected at a scattering angle $\theta = 90°$that, according to the relation $Q = (4\pi n/\lambda)\sin(\theta/2)$, corresponds to a scattering vector $Q = 0.0187\ nm^{-1}$. A single mode optical fiber collected the scattered light as a function of time and the signal was detected by a photomultiplier. In this way the normalized intensity autocorrelation function $g_2(Q,t) = <I(Q,t)I(Q,0)>/<I(Q,0)>^2$ with a high coherence factor close to the ideal unit value was measured. Measurements were performed at fixed temperature around 15°C. Reproducibility has been tested by repeating measurements several times on different samples. The intensity correlation curves obtained from DLS experiments have been analyzed with the Laplace inversion through the CONTIN algorithm weighted as overall contribution to the scattered intensity. However, the scattered intensity depends on the squared volume of the scattering particle, thus leading to an overestimation of the large particles. Therefore, this approach has good reliability for samples of EVs, whose hydrodynamic diameter is expected in the range $D_h = 100 \div 1000$ nm. On the other hand, small particles are under-represented in the intensity-weighted distribution and Laplace transformation can be very inaccurate. To represent the hydrodynamic diameter distribution of Exo with size expected in the range $D_h = 10 \div 100$ nm the volume-weighted distribution has been chosen. The mean size of each population has been calculated by fitting the scattering intensity distribution with a Log-normal function.

Laser Transmission Spectroscopy

Laser Transmission Spectroscopy (LTS) allows to obtain the density of MV in suspension by measuring the transmission of laser light (at zero angle with respect to the incoming beam) through the suspension as a function of wavelength (Li et al., 2010). The transmission of light through the MV sample (re-suspended in KRH) is recorded along with that of KRH. The fundamental data-acquisition process involves measuring the wavelength-dependent transmission of light through an aqueous suspension of vesicles. Given the extinction information, and the known wavelength-dependent properties of the vesicles, Mie theory can be used to accurately determine their density distribution as a function of diameter. The extinction data are analyzed and inverted by a mean square root-based algorithm that outputs the particle size distribution. The integral of the density distribution provides the number of MV per ml of solution and the absolute number (N) of MV per cell is calculated

as the ratio between the number of MV in a given volume and the total number of MV donor cells.

Transmission Electron Microscopy

Microvesicles derived from BV2 cells (extracted as above) were fixed by glutaraldehyde 2.5% in PBS buffer pH 7.4 at least 2 h and gently resuspended in PBS buffer. A drop of the solution was put on a Formvar copper grid 200 mesh for 10 min. After drying with filter paper, uranyl acetate aqueous solution (1%, 1 min) was used for negative staining. Samples were observed with a ZEISS EM 10 transmission electron microscope equipped with a Gatan CCD camera at 60 kw.

Neuronal Viability Assay

Neuroglial cultures at 9–11 days *in vitro* were co-cultured with GL261 cells (5×10^4/well) in the presence or absence of EVs with a ratio of donor:target cells 1:1. After 18 h, cells were treated with detergent-containing buffer and counted in a haemocytometer as already described (Lauro et al., 2010).

MTT Cell Viability Assay

GL261 cells were seeded into 24-well plates and treated with vehicle (untreated), IFN-γ /LPS- or IL 4-MV for 3 days. MTT (500 μg/ml) was added into each well for 1.5 h. DMSO was then added to stop the reaction and the formazan produced was measured at 570 nm. Viability of cells was expressed relative to absorbance.

Wound-Healing Assay

GL261 cells (5×10^5/ml) were seeded into the inner wells of cell culture inserts (ibidi, Germany) placed in a Petri dish. Once attached to the substratum, the inserts were removed, leaving a central 500 μm cell-free septum in which cells could migrate. Cell medium with MV released by IFN-γ /LPS- or IL 4-treated microglia (ratio 1:1 = donor: target cells) was added. Cells were incubated with a cell cycle blocker (cytarabine, 10 μM) to prevent GL261 proliferation for all the time of the experiment. Dishes were maintained at 37°C, 5% CO_2. Pictures of the starting point (0 h) and 24 and 48 h after treatment were taken at a phase contrast microscope (Nikon) and processed through MetaMorph 7.6.5.0 software (Molecular Device). GL261 migration was evaluated by the area between the two cell fronts (by ImageJ software) and data are expressed as % of area occupied by cells.

Invasion Assay

GL261 cells (7×10^3 cells/cm^2) were plated on matrigel-coated polycarbonate membranes (8 μm diameter pores, Corning) of a Boyden Chamber system in presence of IFN-γ /LPS-MV or IL 4-MV (ratio 1:1 donor:target cells) and incubated for 48 h at 37°C with CXCL12 (100 nM, Peprotech) in the lower chamber as chemoattractant. The experiments were performed in presence of cytarabine (10 μM). Cells adhering to the upper side of the membranes were scraped off, whereas cells that have invaded through the pores were stained with a solution containing 50% isopropanol, 1% formic acid, and 0.5% (wt/vol) brilliant blue R 250 and counted in more than 20 fields with a 20× objective.

In vivo Experiments

Experiments were approved by the Italian Ministry of Health, in accordance with the ethical guidelines on use of animals from the EC Council Directive 2010/63/EU. Eight-week-old male C57BL/6N mice were injected with GL261, as previously described (Grimaldi et al., 2016), in the right striatal brain region. During surgery, a guide cannula was placed 2 mm deep in the striatum and it was fixed with quick-setting cement. After 7 and 14 days, mice were infused via cannula with MVs obtained from 1×10^6 microglia cells re-suspended in 4 μl PBS). The day after the second infusion, animals were sacrificed and analyzed for tumor size (Grimaldi et al., 2016). Alternatively, mice were deeply anesthetized and CD11b$^+$ cells were isolated as already described (Grimaldi et al., 2016). Obtained cells were lysed in Trizol reagent (Invitrogen, Milan, Italy) for RNA extraction and Real Time PCR analysis.

BrdU Proliferation Assay

GL261 cells were grown on glass coverslips (1.5×10^4 cells/cm^2) in 24-well plates for 18 h. Cells were exposed to vehicle or EV for 24 h, cellular proliferation was analyzed adding BrdU (10 μM, Sigma-Aldrich, B5002) for 30 min. Cells were washed in PBS, fixed (4% PFA, 30 min), permeabilized (1% Triton X-100, 15 min), blocked (1% BSA, 1 h) at RT and incubated overnight with anti-BrdU (1:200, Novusbio, NB500-169). Hoechst was used to stain all nuclei. BrdU positive cells were counted out of 800 cells for condition. Proliferation rate is calculated as BrdU$^+$ cells respect to Hoechst stained cells. *In vivo*, 15 days after glioma cell injection, BrdU was i.p. injected (50 mg/kg). Two hours later, mice were killed and their brains processed for immunofluorescence.

Immunofluorescence

Coronal brain sections (20 μm) were washed in PBS, blocked (3% goat serum in 0.3% Triton X-100) for 1h at RT and incubated with anti-Iba1 (1:500, Wako, 019-19741, 4°C) or anti-BrdU (1:200, Novusbio, NB500-169, RT). Brain slices were stained with the fluorophore-conjugated secondary antibodies (1 h, RT) and Hoechst for nuclei visualization and analyzed using a fluorescence microscope. For Fluoro Jade-C staining, we followed the manufacturer instructions (Millipore, AG325).

Real Time PCR

RNAs extracted from all samples were quantified and retro-transcribed using IScriptTM Reverse Transcription Supermix (Bio-Rad). Real time PCR (RT-PCR) was carried out in an I-Cycler IQ Multicolor RT-PCR Detection System (Bio-Rad) using SsoFast Eva Green Supermix (Bio-Rad). The PCR protocol consisted of 40 cycles of denaturation at 95°C for 30 s and annealing/extension at 58°C for 30 s. The Ct values from each gene were normalized to the Ct value of GAPDH. Relative quantification was performed using the $2^{-\Delta\Delta Ct}$ method and expressed as fold increase. Primer sequences: arg1, forward: CTCCAAGCCAAAGTCCTTAGAG, reverse: AGGAGCTGTCATTAGGGACATC; cd163 forward: GCTAGACGAAGTCATCTGCACTGGG, reverse: TCAGCCT

CAGAGACATGAACTCGG; cd206 fw: CAAGGAAGGTTGG CATTTGT, reverse: CCTTTCAGTCCTTTGCAAGT; ym1 forward: CAGGTCTGGCAATTCTTCTGAA, reverse: GTCT TGCTCATGTGTGTAAGTGA; fizz1 forward: CCAATCCA GCTAACTATCCCTCC, reverse: ACCCAGTAGCAGTCA TCCCA; gapdh forward: TCGTCCCGTAGACAAAATGG, reverse: TTGAGGTCAATGAAGGGGTC.

RNA Isolation and NanoString nCounter Analysis

Total RNA was isolated from microglia-derived MV by Total Exosome RNA Protein Isolation Kit (# 4478545, Invitrogen) and concentrated using the Microcon10 centrifugal filters (#MRCPRT010, Merck Millipore). Gene expression raw data were normalized considering housekeeping genes via nSolver Software (NanoString). Statistical analysis was conducted in R (version 3.5.0) with RStudio (version 1.1.383[1]). On normalized and log2-transformed data, differential expression was tested applying the Wilcoxon test ($P < 0.05$) and filtering by log2FC > 1.5. All differentially expressed genes were classified into several catalogs according to the Gene Ontology (GO) annotation. The over-representation analyses of GO terms, including biological process and molecular function, were performed using the FIDEA tool[2].

Statistical Analysis

Statistical analyses were performed using SigmaPlot 11.0 Software unless otherwise stated.

DISCUSSION

The present study demonstrated that microglia-derived LPS/IFNγ-MV transfer a protective-antitumor phenotype to the brain of glioma bearing mice. We demonstrated that LPS/IFNγ-MV, which contain the transcripts for a number of inflammation-related genes, can modify TAMs phenotype reducing the expression of anti-inflammatory genes, exert protective effects on neurons and reduce glioma cell proliferation and invasion in surrounding parenchyma.

We have shown that LPS/IFNγ-MV contain 18 genes upregulated in comparison with MV isolated by unstimulated microglia. The majority of these genes referred to the immune response that could underlie the robust effect of MV on the modification of microglia phenotype. It is known that many solid tumors, such as colon-rectal, epithelial ovarian, brain and lung cancers, release EVs which are involved in supporting TAM reprogramming toward an anti-inflammatory, tumor-supporting phenotype (Fabbri et al., 2012; Challagundla et al., 2015; Neviani and Fabbri, 2015; Chen et al., 2017; Shinohara et al., 2017; Cooks et al., 2018). Our findings demonstrated that in the context of a brain tumor, microglia-derived MV can be used in reverse, as a tool to contrast glioma progression, modulating local microenvironment.

[1]http://www.rstudio.com/

[2]http://circe.med.uniroma1.it/fidea/

Previous reports described that EVs released from LPS stimulated BV2 cell line contain cytokines such as TNF-α and IL-6, as well as ribosome, focal adhesion, extracellular matrix, and membrane proteins (Yang et al., 2018). BV2-derived EVs expressing the cytokine IL-4, delivered in a mouse model of multiple sclerosis, propagated an anti-inflammatory response, upregulating microglia and macrophage expression of chitinase 3-like 3 (ym1) and arginase (arg-1), which reduced neuroinflammation with protective effects on tissues (Casella et al., 2018). Consistently, we observed that the EVs released by cytokine-stimulated microglia maintain the phenotype of the donor cells. This result is in line with the evidence that vesicles released by macrophages and dendritic cells reflect the inflammatory state of original cells (Kim et al., 2005; Viaud et al., 2009; Garzetti et al., 2014).

Microvesicle are supposed to transfer their cargo by docking at the plasma membrane of target cells, nevertheless the exact mechanism is not fully revealed. This interaction is neither stochastic nor unspecific because MV do recognize the target cells (Losche et al., 2004). The recognition takes place by activation of specific surface receptors (Gasser and Schifferli, 2004; Bianco et al., 2005), or by transfer of membrane receptors, as demonstrated for the chemokine receptor CCR5 (Mack et al., 2000) and the growth factor receptor EGFRvIII (Al-Nedawi et al., 2008). MV could function as messengers, being enriched in specific miRNA, mRNA, and proteins, to start an angiogenic program (Deregibus et al., 2007), to spread a danger signal through HMGB1 (Tucher et al., 2018) or to induce a developmental program (Ratajczak et al., 2006). In our experiments, we measured mRNA content of microglia released LPS/IFNγ-MV, but we cannot exclude additional transfer elements (such as membrane or signal proteins) from MV to glioma and TAM, responsible for the antitumor effects.

In addition to a modulation of TAM phenotype, we observed that LPS/IFNγ-MV affect glioma cell properties. We observed direct effects on glioma cell migration and invasion capability, and indirect effects on tumor cell viability, which requires the presence of parenchymal cells, likely microglia, as preferential target of microglia-derived EVs (Verderio et al., 2012). The effects of microglia-derived MV on GL261 cells could reflect the transfer of cell-donor information as reported for the first time for antigen-presenting cells that secrete exosomes able to stimulate T cell proliferation (Raposo et al., 1996) or, more recently in Alzheimer disease, for microglia released MV that exert toxicity on neurons (Joshi et al., 2014). In our experiments, EV-mediated reduction of tumor mass could be the cause of the EV-induced decreased neurotoxicity in the presence of glioma. However, we cannot exclude that EVs also directly target neurons, as shown by other authors (Antonucci et al., 2012; Chivet et al., 2014), but the lack of detectable PKH26-MV staining in extra tumoral regions of glioma bearing mice would suggest a direct or local paracrine effect. In addition, *in vitro* experiments demonstrated that microglia-derived MVs did not directly affect neuron viability.

The dimensional analyses of EVs extracted by primary mouse microglia and BV2 cell line reflect data reported on nervous system-released vesicles (Basso and Bonetto, 2016;

Zappulli et al., 2016) and underline the similarity between primary microglia and cell lines, at least for EV dimension. Our TEM analysis shows that single particles have a spherical morphology; in addition to single EV, multiple aggregates are observed confirming size and shape already reported for EVs derived from microglial cells (Turola et al., 2012; Gouwens et al., 2018). In comparison with more physiological conditions (*in vivo* or *ex vivo*), cell lines and primary cultures of microglia display many differences in term of gene expression and response to stimuli (Horvath et al., 2008; Henn et al., 2009). However, there are evident advantages in using EVs derived from microglia cells lines, such as the possibility to obtain sufficient EVs for potential therapeutic application and the similar results obtained with MV from BV2 or from freshly isolated microglia encourage in this direction. However, a detailed analysis of the cargo differences in MV obtained from cell lines, cultured or freshly obtained microglial cells is lacking.

The choice to deliver MV *in situ* into the tumor region allowed us to use a relatively small amount of vesicles per infusion and to observe a direct effect on tumor mass. Different brain delivery of EVs, as into the cisterna magna (Casella et al., 2018), would give additional information on the effects of EVs in the contralateral hemisphere, for the multicellular targets of EVs. Additional delivery methods were tested for EVs, such as the intravenous (Alvarez-Erviti et al., 2011) and intra-nasal (Zhuang et al., 2011) approach. Intravenous administration permits indirect access of MV to the brain through the initial absorption in different cells (Laso-García et al., 2018). Intranasal delivery might reduce the final brain concentration due to lungs and gastrointestinal tract dilution. Nevertheless, both delivering routes would be easily reproduced in humans, while intratumor transfer would be only possible upon surgery procedures during glioma removal. For that reason, alternative EV injection routes, in glioma models, need further investigations. For brain tumor treatment, EVs have been tested to convey specific molecules such as small interference RNAs for TGF beta 1 and VEGF (Zhang et al., 2014; Yang et al., 2017), pro-apoptotic peptides (Ye et al., 2018), and chemotherapeutic drugs (Tang et al., 2012; Yang et al., 2015). EVs are preferred to artificial nanoparticles for their low toxicity (Lewinski et al., 2008; Shvedova et al., 2010).

To our knowledge, this is the first evidence that, in the context of a brain glioma, microglia-derived MVs can be used to transfer a cargo of molecular information that reach TAM restoring a neuroprotective phenotype, modulating their inflammatory state and re-establishing a homeostatic brain microenvironment.

AUTHOR CONTRIBUTIONS

AG, CS, and MC conceived the study and performed the experiments. GC provided technical support for primary mouse cultures and cannulae implantation. VN, AS, BR, and GR performed the DLS and LTS experiments, and analyzed the results. MR and GF performed the TEM experiments and analyzed the results. GRP and FG performed the NanoString experiments and analyzed the results. CL and MC conceived the study and wrote the manuscript. All authors reviewed and approved the final manuscript.

FUNDING

This work was supported by grants from AIRC (IG2015-16699 to CL), from the Italian Ministry of Research (PRIN 2015E8EMCM_001 to CL), from the Italian Ministry of Health (H2020 Euronanomed2 "Nanoglio" to CL), and from Ateneo 2016 to CM; CL is part of the H2020 Twinning Project "SynaNet".

ACKNOWLEDGMENTS

The authors wish to thank the Imaging Facility at Center for Life Nano Science, Istituto Italiano di Tecnologia, for support and technical advice.

SUPPLEMENTARY MATERIAL

The Supplementary Material for this article can be found online at: https://www.frontiersin.org/articles/10.3389/fncel.2019.00041/full#supplementary-material

REFERENCES

Aguzzi, A., and Rajendran, L. (2009). The transcellular spread of cytosolic amyloids, prions, and prionoids. *Neuron* 64, 783–790. doi: 10.1016/j.neuron.2009.12.0162009

Al-Nedawi, K., Meehan, B., Micallef, J., Lhotak, V., May, L., Guha, A., et al. (2008). Intercellular transfer of the oncogenic receptor EGFRvIII by microvesicles derived from tumour cells. *Nat. Cell Biol.* 5, 619–624. doi: 10.1038/ncb1725

Alvarez-Erviti, L., Seow, Y., Yin, H., Betts, C., Lakhal, S., and Wood, M. J. (2011). Delivery of siRNA to the mouse brain by systemic injection of targeted exosomes. *Nat. Biotechnol.* 29, 341–345. doi: 10.1038/nbt.1807

Antonucci, F., Turola, E., Riganti, L., Caleo, M., Gabrielli, M., Perrotta, C., et al. (2012). Microvesicles released from microglia stimulate synaptic activity via enhanced sphingolipid metabolism. *EMBO J.* 31, 1231–1240. doi: 10.1038/emboj.2011.489

Basso, M., and Bonetto, V. (2016). Extracellular vesicles and a novel form of communication in the brain. *Front. Neurosci.* 10:127. doi: 10.3389/fnins.2016.00127

Bianco, F., Pravettoni, E., Colombo, A., Schenk, U., Möller, T., Matteoli, M., et al. (2005). Astrocyte-derived ATP induces vesicle shedding and IL-1 beta release from microglia. *J. Immunol.* 174, 7268–7277. doi: 10.4049/jimmunol.174.11.7268

Carandini, T., Colombo, F., Finardi, A., Casella, G., Garzetti, L., Verderio, C., et al. (2015). Microvesicles: what is the role in multiple sclerosis? *Front. Neurol.* 6:111. doi: 10.3389/fneur.2015.00111

Casella, G., Colombo, F., Finardi, A., Descamps, H., Ill-Raga, G., Spinelli, A., et al. (2018). Extracellular vesicles containing IL-4 modulate neuroinflammation in a mouse model of multiple sclerosis. *Mol. Ther.* 26, 2107–2118. doi: 10.1016/j.ymthe.2018.06.024

Challagundla, K. B., Wise, P. M., Neviani, P., Chava, H., Murtadha, M., Xu, T., et al. (2015). Exosome-mediated transfer of microRNAs within the tumor

microenvironment and neuroblastoma resistance to chemotherapy. *J. Natl. Cancer. Inst.* 107:djv135. doi: 10.1093/jnci/djv135

Chen, Z., Feng, X., Herting, C. J., Garcia, V. A., Nie, K., Pong, W. W., et al. (2017). Cellular and molecular identity of tumor-associated macrophages in glioblastoma. *Cancer Res.* 77, 2266–2278. doi: 10.1158/0008-5472.CAN-16-2310

Chivet, M., Javalet, C., Laulagnier, K., Blot, B., Hemming, F. J., and Sadoul, R. (2014). Exosomes secreted by cortical neurons upon glutamatergic synapse activation specifically interact with neurons. *J. Extracell. Vesicles* 3:24722. doi: 10.3402/jev.v3.24722

Cooks, T., Pateras, I. S., Jenkins, L. M., Patel, K. M., Robles, A. I., Morris, J., et al. (2018). Mutant p53 cancers reprogram macrophages to tumor supporting macrophages via exosomal miR-1246. *Nat. Commun.* 9:771. doi: 10.1038/s41467-018-03224-w

Cunha, C., Gomes, C., Vaz, A. R., and Brites, D. (2016). Exploring new inflammatory biomarkers and pathways during LPS-Induced M1 Polarization. *Mediat. Inflamm.* 2016:6986175. doi: 10.1155/2016/6986175

da Fonseca, A. C., and Badie, B. (2013). Microglia and macrophages in malignant gliomas: recent discoveries and implications for promising therapies. *Clin. Dev. Immunol.* 2013:264124. doi: 10.1155/2013/264124

Deregibus, M. C., Cantaluppi, V., Calogero, R., Lo Iacono, M., Tetta, C., Biancone, L., et al. (2007). Endothelial progenitor cell derived microvesicles activate an angiogenic program in endothelial cells by a horizontal transfer of mRNA. *Blood* 110, 2440–2448. doi: 10.1182/blood-2007-03-078709

Fabbri, M., Paone, A., Calore, F., Galli, R., Gaudio, E., Santhanam, R., et al. (2012). MicroRNAs bind to toll-like receptors to induce prometastatic inflammatory response. *Proc. Natl. Acad. Sci. U.S.A.* 109, E2110–E2116. doi: 10.1073/pnas.1209414109

Fevrier, B., Vilette, D., Archer, F., Loew, D., Faigle, W., Vidal, M., et al. (2004). Cells release prions in association with exosomes. *Proc. Natl. Acad. Sci. U.S.A.* 101, 9683–9688. doi: 10.1073/pnas.0308413101

Fonseca, A. C., Romão, L., Amaral, R. F., Assad Kahn, S., Lobo, D., Martins, S., et al. (2012). Microglial stress inducible protein 1 promotes proliferation and migration in human glioblastoma cells. *Neuroscience* 200, 130–141. doi: 10.1016/j.neuroscience.2011.10.025

Garzetti, L., Menon, R., Finardi, A., Bergami, A., Sica, A., Martino, G., et al. (2014). Activated macrophages release microvesicles containing polarized M1 or M2 mRNAs. *J. Leukoc. Biol.* 95, 817–825. doi: 10.1189/jlb.0913485

Gasser, O., and Schifferli, J. A. (2004). Activated polymorphonuclear neutrophils disseminate anti-inflammatory microparticles by ectocytosis. *Blood* 104, 2543–2548. doi: 10.1182/blood-2004-01-0361

Gouwens, L. K., Ismail, M. S., Rogers, V. A., Zeller, N. T., Garrad, E. C., Amtashar, F. S., et al. (2018). Aβ42 protofibrils interact with and are trafficked through microglial-derived microvesicles. *ACS Chem. Neurosci.* 9, 1416–1425. doi: 10.1021/acschemneuro.8b00029

Grimaldi, A., D'Alessandro, G., Golia, M. T., Grössinger, E. M., Di Angelantonio, S., Ragozzino, D., et al. (2016). KCa3.1 inhibition switches the phenotype of glioma-infiltrating microglia/macrophages. *Cell Death Dis.* 7, e2174. doi: 10.1038/cddis.2016.73

Hambardzumyan, D., Gutmann, D. H., and Kettenmann H. (2016). The role of microglia and macrophages in glioma maintenance and progression. *Nat. Neurosci.* 19, 20–27. doi: 10.1038/nn.4185

Henn, A., Lund, S., Hedtjarn, M., Schrattenholz, A., Porzgen, P., and Leist, M. (2009). The suitability of BV2 cells as alternative model system for primary microglia cultures or for animal experiments examining brain inflammation. *ALTEX* 26, 83–94. doi: 10.14573/altex.2009.2.83

Horvath, R. J., Nutile-McMenemy, N., Alkaitis, M. S., and Deleo, J. A. (2008). Differential migration, LPS-induced cytokine, chemokine, and NO expression in immortalized BV-2 and HAPI cell lines and primary microglial cultures. *J. Neurochem.* 107, 557–569. doi: 10.1111/j.1471-4159.2008.05633.x

Iraci, N., Gaude, E., Leonardi, T., Costa, A. S. H., Cossetti, C., Peruzzotti-Jametti, L., et al. (2017). Extracellular vesicles are independent metabolic units with asparaginase activity. *Nat. Chem. Biol.* 9, 951–955. doi: 10.1038/nchembio.2422

Joshi, P., Turola, E., Ruiz, A., Bergami, A., Libera, D. D., Benussi, L., et al. (2014). Microglia convert aggregated amyloid-β into neurotoxic forms through the shedding of microvesicles. *Cell Death Differ.* 21, 582–593. doi: 10.1038/cdd.2013.180

Kim, S. H., Lechman, E. R., Bianco, N., Menon, R., Keravala, A., Nash, J., et al. (2005). Exosomes derived from IL-10-treated dendritic cells can suppress inflammation and collagen-induced arthritis. *J. Immunol.* 174, 6440–6448. doi: 10.4049/jimmunol.174.10.6440

Korkut, C., Li, Y., Koles, K., Brewer, C., Ashley, J., Yoshihara, M., et al. (2013). Regulation of postsynaptic retrograde signaling by presynaptic exosome release. *Neuron* 77, 1039–1046. doi: 10.1016/j.neuron.2013.01.013

Laso-García, F., Ramos-Cejudo, J., Carrillo-Salinas, F. J., Otero-Ortega, L., Feliú, A., Gómez-de Frutos, M., et al. (2018). Therapeutic potential of extracellular vesicles derived from human mesenchymal stem cells in a model of progressive multiple sclerosis. *PLoS One* 13:e0202590. doi: 10.1371/journal.pone.0202590

Lauro, C., Cipriani, R., Catalano, M., Trettel, F., Chece, G., Brusadin, V., et al. (2010). Adenosine A1 receptors and microglial cells mediate CX3CL1-induced protection of hippocampal neurons against Glu-induced death. *Neuropsychopharmacology* 35, 1550–1559. doi: 10.1038/npp.2010.26

Lewinski, N., Colvin, V., and Drezek, R. (2008). Cytotoxicity of nanoparticles. *Small* 4, 26–49. doi: 10.1002/smll.2007005954

Li, F., Schafer, R., Hwang, C., Tanner, C. E., and Ruggiero, S. T. (2010). High-precision sizing of nanoparticles by laser transmission spectroscopy. *Appl. Opt.* 49, 6602–6611. doi: 10.1364/AO.49.006602

Losche, W., Scholz, T., Temmler, U., Oberle, V., and Claus, R. A. (2004). Platelet-derived microvesicles transfer tissue factor to monocytes but not to neutrophils. *Platelets* 15, 109–115. doi: 10.1080/09537100310001649885

Mack, M., Kleinschmidt, A., Brühl, H., Klier, C., Nelson, P. J., Cihak, J., et al. (2000). Transfer of the chemokine receptor CCR5 between cells by membrane-derived microparticles: a mechanism for cellular human immunodeficiency virus 1 infection. *Nat. Med.* 6, 769–775. doi: 10.1038/77498

Neviani, P., and Fabbri, M. (2015). Exosomic microRNAs in the tumor microenvironment. *Front. Med.* 2:47. doi: 10.3389/fmed.2015.00047

Raposo, G., Nijman, H. W., Stoorvogel, W., Liejendekker, R., Harding, C. V., Melief, C. J., et al. (1996). B lymphocytes secrete antigen-presenting vesicles. *J. Exp. Med.* 183, 1161–1172. doi: 10.1084/jem.183.3.1161

Ratajczak, J., Miekus, K., Kucia, M., Zhang, J., Reca, R., Dvorak, P., et al. (2006). Embryonic stem cell-derived microvesicles reprogram hematopoietic progenitors: evidence for horizontal transfer of mRNA and protein delivery. *Leukemia* 20, 847–856. doi: 10.1038/sj.leu.2404132

Shinohara, H., Kuranaga, Y., Kumazaki, M., Sugito, N., Yoshikawa, Y., Takai, T., et al. (2017). Regulated polarization of tumor-associated macrophages by miR-145 via colorectal cancer-derived extracellular vesicles. *J. Immunol.* 199, 1505–1515. doi: 10.4049/jimmunol.1700167

Shvedova, A. A., Kagan, V. E., and Fadeel, B. (2010). Close encounters of the small kind: adverse effects of man-made materials interfacing with the nanocosmos of biological systems. *Annu. Rev. Pharmacol. Toxicol.* 50, 63–88. doi: 10.1146/annurev.pharmtox.010909.105819

Tang, K., Zhang, Y., Zhang, H., Xu, P., Liu, J., Ma, J., et al. (2012). Delivery of chemotherapeutic drugs in tumour cell-derived microparticles. *Nat. Commun.* 3:1282. doi: 10.1038/ncomms2282

Tucher, C., Bode, K., Schiller, P., Claßen, L., Birr, C., Souto-Carneiro, M. M., et al. (2018). Extracellular vesicle subtypes released from activated or apoptotic T-lymphocytes carry a specific and stimulus-dependent protein cargo. *Front. Immunol.* 9:534. doi: 10.3389/fimmu.2018.00534

Turola, E., Furlan, R., Bianco, F., Matteoli, M., and Verderio, C. (2012). Microglial microvesicle secretion and intercellular signaling. *Front. Physiol.* 3:149. doi: 10.3389/fphys.2012.00149

Verderio, C., Muzio, L., Turola, E., Bergami, A., Novellino, L., Ruffini, F., et al. (2012). Myeloid microvesicles are a marker and therapeutic target for neuroinflammation. *Ann. Neurol.* 72, 610–624. doi: 10.1002/ana.23627

Viaud, S., Terme, M., Flament, C., Taieb, J., André, F., Novault, S., et al. (2009). Dendritic cell-derived exosomes promote natural killer cell activation and

proliferation: a role for NKG2D ligands and IL-15Ralpha. *PLoS One* 4:e4942. doi: 10.1371/journal.pone.0004942

Yang, T., Fogarty, B., LaForge, B., Aziz, S., Pham, T., Lai, L., et al. (2017). Delivery of small interfering RNA to inhibit vascular endothelial growth factor in zebrafish using natural brain endothelia cell-secreted exosome nanovesicles for the treatment of brain cancer. *AAPS J.* 19, 475–486. doi: 10.1208/s12248-016-0015-y

Yang, T. Z., Martin, P., Fogarty, B., Brown, A., Schurman, K., Phipps, R., et al. (2015). Exosome delivered anticancer drugs across the blood-brain barrier for brain cancer therapy in Danio Rerio. *Pharm. Res.* 32, 2003–2014. doi: 10.1007/s11095-014-1593-y

Yang, Y., Boza-Serrano, A., Dunning, C. J. R., Clausen, B. H., Lambertsen, K. L., and Deierborg, T. (2018). Inflammation leads to distinct populations of extracellular vesicles from microglia. *J. Neuroinflammation* 15:168. doi: 10.1186/s12974-018-1204-7

Ye, Z., Zhang, T., He, W., Jin, H., Liu, C., Yang, Z., et al. (2018). Methotrexate-loaded extracellular vesicles functionalized with therapeutic and targeted peptides for the treatment of glioblastoma multiforme. *ACS Appl. Mater. Interfaces* 10, 12341–12350. doi: 10.1021/acsami.7b18135

Zappulli, V., Friis, K. P., Fitzpatrick, Z., Maguire, C. A., and Breakefield, X. O. (2016). Extracellular vesicles and intercellular communication within the nervous system. *J. Clin. Invest.* 126, 1198–1207. doi: 10.1172/JCI81134

Zhang, X., Abels, E. R., Redzic, J. S., Margulis, J., Finkbeiner, S., and Breakefield, X. O. (2016). Potential transfer of polyglutamine and CAG-repeat RNA in extracellular vesicles in Huntington's disease: background and evaluation in cell culture. *Cell. Mol. Neurobiol.* 36, 459–470. doi: 10.1007/s10571-016-0350-7

Zhang, Y., Li, L., Yu, J., Zhu, D., Zhang, Y., Li, X., et al. (2014). Microvesicle-mediated delivery of transforming growth factor beta1 siRNA for the suppression of tumor growth in mice. *Biomaterials* 35, 4390–4400. doi: 10.1016/j.biomaterials.2014.02.003

Zhuang, X., Xiang, X., Grizzle, W., Sun, D., Zhang, S., Axtell, R. C., et al. (2011). Treatment of brain inflammatory diseases by delivering exosome encapsulated anti-inflammatory drugs from the nasal region to the brain. *Mol. Ther.* 19, 1769–1779. doi: 10.1038/mt.2011.164

Conflict of Interest Statement: The authors declare that the research was conducted in the absence of any commercial or financial relationships that could be construed as a potential conflict of interest.

Appendix B

Appendix B: side techniques

In this appendix we report the bases of the experimental techniques employed in this thesis. In particular we describe the Dynamic Light Scattering (DLS), the Transmission Electron Microscopy (TEM), and the Scanning Electron Microscopy (SEM).

B.1 Dynamic Light Scattering

Consider a scattering medium, such as a suspension of colloidal particles, illuminated by coherent light. At any instant, the far-field pattern of scattered light comprises a grainy random diffraction, or "speckle" pattern (figure B.1). The interference of the phases of the light scattered by the individual particles yields regions of large and small intensity, for constructive and destructive interference, respectively. Furthermore, since the scattering medium evolves in time, as in the case of particle positions $\vec{R}_j(t)$ which change due to Brownian motion, the phase changes, and the speckle pattern fluctuates from one random configuration to another. Thus, as sketched in figure B.1, the intensity $I(\vec{q},t)$ scattered to a point in the far field fluctuates randomly in time. Clearly, information on the motions of the particles is encoded in this random signal: at the simplest level, the faster the particles move, the more rapidly the intensity fluctuates (figure B.1 b).

In DLS, significant information is extracted from the fluctuating intensity by constructing its time correlation function, defined as

$$\langle I(\vec{q},0)I(\vec{q},\tau)\rangle \equiv \lim_{T\to\infty}\frac{1}{T}\int_0^T dt I(\vec{q},t)I(\vec{q},t+\tau) \tag{B.1}$$

This quantity effectively compares the signal $I(\vec{q},t)$ with a delayed version $I(\vec{q},t+\tau)$ of itself, for all starting times t and for a range of delay times τ.

Typical behaviour of the intensity correlation function is shown in figure B.1 b. At zero delay, equation (B.1) reduces to

$$\lim_{T\to\infty}\langle I(\vec{q},0)I(\vec{q},\tau)\rangle = \langle I(\vec{q})^2\rangle \tag{B.2}$$

For delay times much greater than the typical fluctuation time T_C of the intensity, fluctuations in $I(\vec{q},t)$ and $I(\vec{q},t+\tau)$ are uncorrelated, so that the average in equation (B.1) can be separated:

$$\lim_{T\to\infty}\langle I(\vec{q},0)I(\vec{q},\tau)\rangle = \langle I(\vec{q})\rangle\langle I(\vec{q},\tau)\rangle = \langle I(\vec{q})\rangle^2 \tag{B.3}$$

The intensity correlation function decays from the mean-square intensity at small delay times to the square of the mean at long times; the characteristic time T_C of this decay is a measure of the typical fluctuation time of the intensity (figure B.1c).

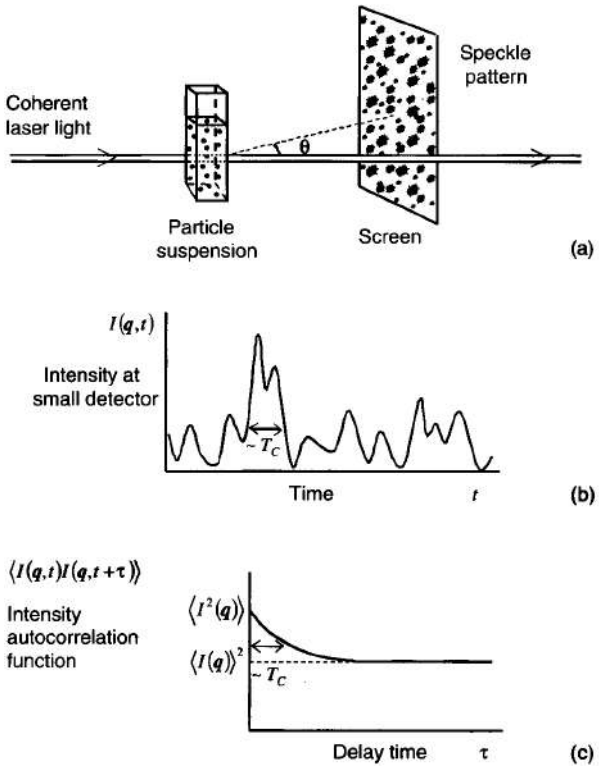

FIGURE B.1: a) Coherent (laser) light scattered by a random medium, such as a suspension of colloidal particles, gives rise to a random diffraction, or speckle, pattern in the far field. b) The fluctuating intensity observed at a detector with the size of about one speckle. c) The time-dependent part of the correlation function decays with a time constant T_C equal to the typical fluctuation time of the scattered light. Figure adapted from reference [104].

In the next sections we consider the properties of the scattered field and of the associated correlation functions, all of which underlie the theory of dynamic light scattering. For more detailed descriptions of dynamic light scattering and its applications, consult the references [105, 106, 107].

The correlation functions

To investigate the properties of the fluctuating scattered field, we consider the simple situation of a dilute suspension of identical spherical particles. The instantaneous amplitude of the field $E(\vec{q},t)$, for identical homogeneous spherical particles, omitting the pre-factors, can be espressed as

$$E(\vec{q},t) = \sum_j \exp[-i\vec{q}\cdot\vec{R}_j(t)]. \tag{B.4}$$

The total scattered field $E(\vec{q},t)$ is the (vectorial) sum of the individual "phase vectors" $\exp[-i\vec{q}\cdot\vec{R}_j(t)]$ making an angle $\vec{q}\cdot\vec{R}_j(t)$ with the real axis. Since the particles are randomly distributed throughout the sample, the phase angles are randomly distributed between 0 and 2π and, thus, the field $E(\vec{q},t)$ can be pictorially represented as a two-dimensional random walk of N vectors in the complex plane. Due to the motion of the particles, positions $\vec{R}_j(t)$ and phase angles $\{\vec{q}\cdot\vec{R}_j(t)\}$ change, and the total scattered field has fluctuations which become totally uncorrelated over times, such that the phase angles change by $\sim 2\pi$. In such conditions, the average value of the scattered field $\langle E(\vec{q},t)\rangle$ is zero.

The average of the scattered intensity is

$$\begin{aligned}\langle I(\vec{q},t)\rangle =& \langle |E(\vec{q},t)|^2\rangle = \sum_{j=1}^{N}\sum_{k=1}^{N}\langle \exp\{-i\vec{q}\cdot[\vec{R}_j(t)-\vec{R}_k(t)]\}\rangle \\ =& \sum_j 1 + \sum_{j\neq k}\langle \exp[-i\vec{q}\cdot\vec{R}_j(t)]\rangle\langle \exp[-i\vec{q}\cdot\vec{R}_k(t)]\rangle = N\end{aligned} \tag{B.5}$$

where, in averaging the cross-terms separately, we assume that the suspension is dilute, so that the particles position are uncorrelated. If the number N of particles in the scattering volume is large, the scattered field $E(\vec{q},t)$ is a complex (two-dimensional) random variable having a gaussian probability distribution.

Let's define the normalised time correlation function of the scattered field as

$$g^{(1)}(q,\tau) \equiv \frac{\langle E(\vec{q},0)\rangle E^*(\vec{q},\tau)}{I(\vec{q})} \tag{B.6}$$

In the case of isotropic samples, the averaged quantity $g^{(1)}(q,\tau)$ depends only on the modulus q of the scattering vector. Substituting eq. (B.4) into (B.6), after some manipulations, we obtain

$$\begin{aligned} g^{(1)}(q,\tau) &= N^{-1}\sum_j \langle \exp\{-i\vec{q}\cdot[\vec{R}_j(0)-\vec{R}_j(\tau)]\}\rangle \\ &= \langle \exp\{-i\vec{q}\cdot[\vec{R}(0)-\vec{R}(\tau)]\}\rangle \end{aligned} \tag{B.7}$$

The last step follows from the fact that the *average* motions of identical particles is obviously identical for each particle.

The normalised time correlation function of the scattered field $g^{(1)}(q,\tau)$ can be directly measured only with a heterodyne experimental setup, by mixing the diffused beam and a portion of the incident beam at the surface of the detector. When only the scattered light impinges on detector, in the homodyne setup, DLS measures the time correlation function of the scattered intensity. Using eq. (B.4), the time correlation function of the scattered intensity can be written as

$$\begin{aligned}&\langle I(\vec{q},0)I(\vec{q},\tau)\rangle = \\ &\sum_{j,k,l,m}\langle\exp\{-i\vec{q}\cdot[\vec{R}_j(0)-\vec{R}_k(0)+\vec{R}_l(\tau)-\vec{R}_m(\tau)]\}\rangle = \\ &\langle I(\vec{q},0)I(\vec{q},\tau)\rangle = N^2+N^2|\langle\exp\{-i\vec{q}\cdot[\vec{R}(0)-\vec{R}(\tau)]\}\rangle|^2\end{aligned} \tag{B.8}$$

where we exploit the independence of particle positions in a dilute suspension and consider the limit $N\to\infty$.

We define the normalised time correlation function of the scattered intensity by

$$g^{(2)}(q,t)\equiv\frac{\langle I(\vec{q},0)I(\vec{q},\tau)\rangle}{\langle I(\vec{q},0)\rangle^2} \tag{B.9}$$

and, using equations (B.5), (B.6), (B.7), and (B.8), we obtain that

$$g^{(2)}(q,t)=1+[g^{(1)}(q,t)]^2 \tag{B.10}$$

This result, called the "Siegert relation", reflects the factorisation properties of the correlation functions of a complex Gaussian variable.

The results derived until now correspond to the situation of "far-field", since they are derived considering the amplitude of the electric field scattered to a point in the far field. Actually, a detector has a non-zero active area and, therefore, sees different scattered fields (or intensities) at different points on its surface. Then, it can be shown that eq. (B.10) is modified to

$$g^{(2)}(q,t)=1+\beta[g^{(1)}(q,t)]^2 \tag{B.11}$$

where β is a factor which represents the degree of spatial coherence of the scattered light over the detector and is determined by the ratio of the detector area to the area of one speckle. When this ratio is much less than 1, as in the case of a "point detector" , $\beta\to 1$. On the contrary, when it is large, corresponding to the detection of many, independently fluctuating speckles, $\beta\to 0$. In practice, the detector aperture is usually chosen to accept about one speckle and $\beta\approx 0.8$. Inverting eq. (B.11) gives

$$\beta^{1/2}g^{(1)}(q,\tau)=\sqrt{g^{(2)}(q,\tau)-1} \tag{B.12}$$

where β is usually regarded as an uninteresting parametre, fitted during data analysis.

Particle sizing is one of the main applications of DLS. It is done by measuring the diffusion constant of particles undergoing Brownian motion in dilute suspension. Here, we first consider the simplest case of identical spherical particles, and then the more realistic situation where spherical particles are "polydispersed", i.e., they have a distribution of size.

Dilute suspension of identical spheres in Brownian motion

For a dilute suspension of identical, non-interacting spheres, with uncorrelated particles position, the field correlation function is given by

$$g^{(1)}(q,\tau) = \langle \exp\{-i\vec{q}\cdot[\vec{R}(0) - \vec{R}(\tau)]\}\rangle = \langle \exp \vec{q}\cdot[\Delta\vec{R}(\tau)]\rangle \tag{B.13}$$

where $\Delta\vec{R}(\tau) \equiv \vec{R}(\tau) - \vec{R}(0)$ is the displacement of the particle in time τ.

The displacement of a particle in Brownian motion is a real three dimensional random variable having a Gaussian probability distribution:

$$P[\Delta\vec{R}(\tau)] = \left[\frac{3}{2\pi\langle\Delta R^2(\tau)\rangle}\right]^{3/2} \exp\left[-\frac{3\Delta R^2(\tau)}{2\langle\Delta R^2(\tau)\rangle}\right] \tag{B.14}$$

where the particle mean-square displacement in time τ is

$$\langle\Delta R^2(\tau)\rangle = 6D_0\tau \qquad D_0 = \frac{k_B T}{6\pi\eta R} \tag{B.15}$$

where D_0 is the diffusion constant for a free particle, given by the Stoke-Einstein equation, with k_B the Boltzmann constant, T the temperature, η the viscosity of the suspending medium and R the particle radius. Evaluation of the average in eq. (B.13) over the distribution of eq. (B.14) gives

$$g^{(1)}(q,\tau) = \exp\left[-\frac{q^2}{6}\langle\Delta R^2(\tau)\rangle\right] = \exp(-q^2 D_0\tau) \tag{B.16}$$

In this simple case, $g^{(1)}(q,\tau)$ is measured by means of equation B.12 and fitted to an exponential in delay time τ giving the decay rate $q^2 D_0$. Since the scattering vector q can be calculated from the known setup of the experiment, the diffusion constant of the particles can be obtained and their radius calculated from equation B.15.

Dilute suspension of polydisperse spheres in Brownian motion

In a more realistic situation, the approximation of monodisperse system may be not verified, for example, in the presence of colloidal particles or for aggregates built up by particles with different masses. Since the scattering amplitude of a Brownian particle depends on the size of the particle, scattering data are affected by polydispersity. Here, we consider the effect of size polydispersity in the case of dilute systems, for which interactions between Brownian particles can be neglected and particle positions are uncorrelated. The assumption of dilute suspension of particle in Brownian motion leads to

$$g^{(1)}(q,\tau) = \frac{\sum_j b_j(q)^2 \exp(-q^2 D_j\tau)}{\sum_j b_j(q)^2} \tag{B.17}$$

with $D_j \equiv k_B T/6\pi\eta R_j$ the diffusion constant of particle j having radius R_j.

This result means that the intermediate scattering function for a dilute suspension of spheres is a sum of exponentials, each corresponding to particles with a definite size, weighted by the intensity scattered by that particles. Eq. (B.17) can be rewritten as

$$g^{(1)}(q,\tau) = \int P(D)\exp(-Dq^2\tau)dD \qquad \text{with} \quad \int_0^1 P(D)dD = 1 \tag{B.18}$$

where $P(D)$ is the normalised intensity-weighted distribution of diffusion constants, which is determined by the distribution $P(R)$ of particle sizes. We note that $g^{(1)}(q,\tau)$ (see eq. (B.18)) for polydisperse systems is written as the Laplace transform with respect to D of the intensity-weighted distribution of diffusion constants $P(D)$. Thus, in principle, inverse Laplace transformation of the measured $f_M(q,\tau)$ with respect to time yields $P(D)$, and hence information on the distribution of particle sizes. The difficulty with attempting this operation in practice is that the inverse Laplace transformation is a well-known "ill-conditioned" process, i.e. there exist many and often different distributions $P(D)$, whose transforms fit the measured data within experimental error [105]. Possible inversion procedures employ constrained regularisation methods to get the simplest (smoothed) solution, which is the least probable to show artefacts, being yet compatible with data. The most popular methods has been encoded in the program package, CONTIN, by Provencher [89].

DLS experimental setup

The DLS measurements reported in this thesis were performed employing a MALVERN Nano Zetasizer apparatus equipped with a 5 mW HeNe laser (Malvern Instruments LTD, UK). This system uses backscatter detection, i.e. the scattered light is collected at an angle of 173°. The main advantage of this detection geometry, when compared to the more conventional 90°, is its inherent larger insensitiveness to multiple scattering effects [108]. Intuitively, since nor the illuminating laser beam, nor the detected scattered light need to travel through the entire sample, chances that incident and scattered photons will encounter more than one particle are reduced. Moreover, as large particles scatter mainly in the forward direction, the effects on the size distribution of dust, or of large irregular aggregates, are greatly reduced. To obtain the size distribution, the measured autocorrelation functions were analysed by means of the CONTIN algorithm.

B.2 Transmission Electron Microscopy

The resolution ρ of a microscope, defined as the smallest distance between just resolvable specimen points, is limited by the wavelength λ of the radiation employed and the numerical aperture $n\sin\alpha$ of the objective lens, $\rho = 0.6\lambda/n\sin\alpha$. An improvement of the resolution is only possible by decreasing the wavelength, i.e. using ultraviolet or X-rays, ultrasound waves, electron and ions.

However, resolution is meaningless if we do not have enough image contrast, which originates as a result of interactions with the specimen. Absorption, refraction, phase shift, diffraction, birefringence and fluorescence are some examples of the light-specimen interactions used in normal, interference and polarizing light microscopes.

In electron microscopy, we have to consider the different types of electron-specimen interactions that influence the obtainable information and also the instrumental design of microscopes. Elastic scattering at atomic nuclei trough large angles $\theta > \alpha_0$ results in scattering contrast. Interference of elastically scattered electron waves results in phase contrast. Inelastic scattering of electron beam with the electron of the specimen atoms is accompanied by the excitation of electrons of the valence or of the inner shell, and it gives analytical information about the chemical composition of the specimen. Since in a specimen the number of electron is higher than that of atoms, inelastic scattering is the most important phenomenon in the image formation.

Contrast in the TEM depends not only on the thickness of the sample, but even on the atomic number of the atoms in the specimen. The higher the atomic number, the more electrons are scattered, and the greater is the contrast. Hence, to make biomacromolecules - composed mainly of carbon, oxygen, nitrogen, and hydrogen - visible, they are usually stained with heavy metal salts containing osmium, uranium, lead or tungsten. In negative staining, macromolecules or supramolecular assemblies are adsorbed from their suspension onto a thin carbon supporting film and then briefly washed with an aqueous solution of a heavy metal salt (e.g., 1% uranyl acetate or 2% Na-phosphotungstate), before the sample is allowed to dry. A very thin film of metal salt now covers the support film everywhere except where it has been excluded by the presence of an adsorbed macromolecule or supramolecular structure. Because the macromolecule allows the electrons to pass much more readily respect to the surrounding heavy metal film, a reversed or negative image of the molecule is created, hence the name "negative staining".

In general, in TEM the energy of the electron beam employed is around $100keV$ and the overall obtainable resolution is of the order of $0.1 - 0.2nm$.

Elements forming a TEM

A transmission electron microscope is composed by an electron-optical column, formed by a system of illumination (the electron source), a system of lens and condenser lenses, an objective, a specimen support, and a projection system. Then, a series of electric and electronic devices and circuits allows the control of the system of illumination. A vacuum producer and controller system is employed to keep the electron-optical column free from gas and impurity, which could damage the electron beam. The most critical parts of the instrument are the objective and specimen support, since the resolution power depends on them [109].

The illumination system is composed by the electron gun, the electromagnetic lenses, two condenser lenses, and a moving diaphragm.

The electron gun is formed by a cathode emitting electron into the vacuum and accelerates them through a voltage U between cathode and anode. The result is a kinetic electron energy $E = eU$. Thermionic emission from heated tungsten filaments or lanthanum hexaboride tips is the usual electron source for electron optical instruments. Operative parametres as the beam diameter, the total current, the brightness, and the energy distribution of the electron are extremely important for the resolution and the image formation.

Electron passes through a system of electromagnetic and condenser lenses, which allows to vary the angular aperture of the beam and fix the density of current and the exposition time. Electromagnetic lenses are the magnetic equivalent of the glass lenses in an optical microscope, while the double condenser system, consisting of two or more lenses and an aperture, controls spot size and beam convergence. Moreover, it focuses the beam on the specimen, so that only a small portion of the sample is illuminated, and the contamination and damage is reduced.

From condenser lenses the beam is focused on the specimen support. The preparing support grids are mounted in a specimen cartridge, which is introduced into the specimen stage from the top of the objective lens, or mounted on a specimen stub. The specimen stage enables to shift the specimen, special cartridges can tilt or rotate the specimen.

The image formation is realised by means of the objective lens, coupled with the projection and magnification system. The objective lens forms an inverted initial image, which is subsequently magnified. In the back focal plane of the objective

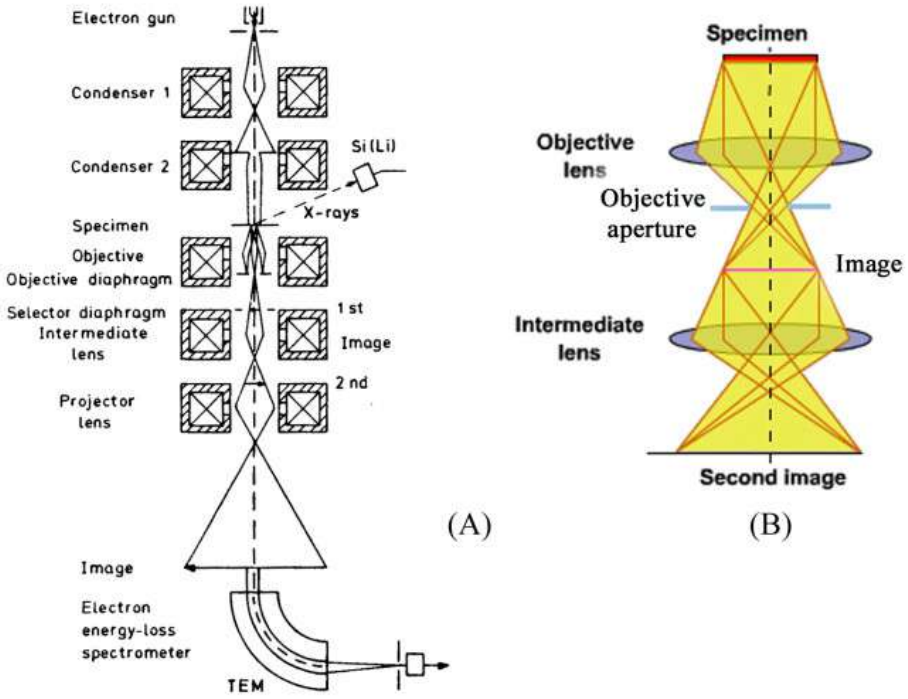

FIGURE B.2: a) Schematic view of a TEM apparatus. b) Schematic representation of the image formation system. Figure adapted from reference [109].

lens a diffraction pattern is formed. The objective aperture is placed in the back focal plane of the image, its function is to select the electrons that contribute to the image, and thereby affect the appearance of the image, improving the contrast of the final image (see fig. B.3). The first intermediate lens magnifies the initial image that is formed by the objective lens. The lens can be focused on the initial image or on the diffraction pattern formed in the back focal plane of the objective lens. This determines whether the viewing screen of the microscope shows a diffraction pattern or an image.

The system of projection transfers and magnify the image, or the diffraction pattern, formed on the objective. Magnification in the electron microscope can be varied from hundreds to several hundred thousands of times. This is done by varying the strength of the projector and intermediate lenses.

Imaging modes

The image is realised by collecting a portion of the scattered beam by means of the diaphragm of the objective. The image obtained in this way is called "bright field image". If the incident beam is tilted, the image in "dark field" is collected. This image presents bright region in correspondence to the region of the specimen which originates the diffracted beam, and, conversely, dark region corresponding to the other region. The image realised in bright field is complementary to the dark field image. The bright field image is the most employed procedure to collect sample images, since it reproduces as well more sensibly the regions which do not produce the well defined orientation of the diffraction beam. The contemporary application of the two modes makes the observation of nanometric object possible, so the morphology of the sample is easily observable.

The diffraction pattern of the specimen at the focal plane of the objective lens can be magnified on the viewing screen by changing the excitation (focal length) of the intermediate (or diffraction) lens and by selecting a specimen area by means of a diaphragm in front of this lens.

B.3 Scanning Electron Microscopy

SEM is an electronic microscopy which uses an electron beam as illumination source with whom scans the sample surface to obtain an image of its topography [110]. The incidents electrons can interact with the specimen atoms through elastic scattering in which the electrons are scattered by atomic nuclei or outer shell electrons with similar energies. Those having a scattering angle more than 90° are called backscattered electrons. The electrons can also undergo inelastic scattering, in which the atoms are ionised and emit secondary electrons, together with characteristic X-rays, Auger electrons and cathodoluminescence. The electrons mainly used for imaging

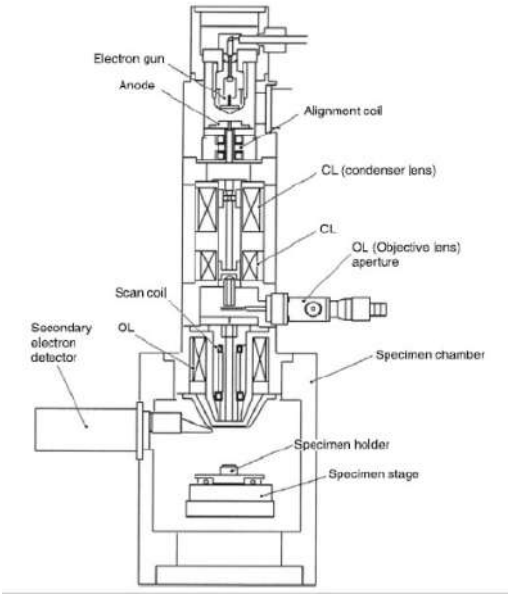

FIGURE B.3: Schematic view of a SEM apparatus.

are the secondary and the backscattered ones. Secondary electrons have low energies ($3 - 5\ eV$) and propagate for a distances of few nanometres, thus allowing to resolve surface structures with a precision of the order of 10 nm; for this reason, they are used for imaging surface textures and roughness. Backscattered electrons can undergo single or multiple scattering and have a energy greater than 50 eV. Because the number of backscattered electrons depends on the atomic number of the sample (elements with high atomic number scatter more electrons), they provide atomic contrast in the SEM images. Chemical information about the specimen's could be obtained through the analysis of the X-rays signal, by means the so called "micro-analysis". X-rays are emitted when a primary beam electron causes the ejection of an inner shell electron from the sample. This vacancy is filled by an outer shell electron which emits an X-ray, whose energy is related to the energy difference between the electron orbitals involved in the transition [111]. The main component of the SEM experimental setup is the electron gun. In the first experimental setup tungsten filament or lanthanum hexaboride cathodes were used, but recently field emission

sources are employed. To avoid electron scattering by air, a high-vacuum environment is needed. A field emission gun is composed by a single crystal tungsten wire with a very sharp tip which is the electron source. The emitter tip is placed between two anodes connected to two different voltages: the first is used to extract the electrons and the second to accelerating them. The emitted electron beam is guided towards the sample by a magnetic field generated by a system of condenser lenses made of copper. The beam is further focused by objective lenses which reduce the diameter of the electron beam and enhances the image resolution. This process decreases the beam size from 50 μm to $1 - 100$ nm. The laser beam scans the sample surface thanks to a system of scanning coils, which deflect the probe spot allowing his motion on the plane. In proximity of the specimen, different kinds of detectors are placed, each specific to the type of object to be revealed: solid state backscattered electron detectors, secondary electron detector, X-ray spectrometers for characteristic X-rays.

Bibliography

[1] Frank Li et al. "High-precision sizing of nanoparticles by laser transmission spectroscopy". In: *Applied optics* 49.34 (2010), pp. 6602–6611.

[2] James D Ingle and Stanley R Crouch. *Spectrochemical analysis*. English. Includes bibliographies and index. Englewood Cliffs, N.J. : Prentice Hall, 1988. ISBN: 0138268762.

[3] H. C. van de (Hendrik Christoffel van de) Hulst. *Light scattering by small particles*. English. Rev.ed. Reprint. Originally published: New York : Wiley 1957. (Structure of matter series). New York : Dover Publications, 1981. ISBN: 0486642283 (pbk.)

[4] Milton Kerker. *The scattering of light and other electromagnetic radiation: physical chemistry: a series of monographs*. Vol. 16. Academic press, 2013.

[5] NC Nguyen. "A note on tikhonov regularization of linear Ill-posed problems". In: *Massachusetts Institute of Technology* (2006), pp. 1–4.

[6] Andrey N Tikhonov and Vasilii Iakkovlevich Arsenin. *Solutions of ill-posed problems*. Vol. 14. Winston, Washington, DC, 1977.

[7] Ramesh M Gulrajani. "The forward and inverse problems of electrocardiography". In: *IEEE Engineering in Medicine and Biology Magazine* 17.5 (1998), pp. 84–101.

[8] Josef Honerkamp and Jürgen Weese. "Tikhonovs regularization method for ill-posed problems". In: *Continuum Mechanics and Thermodynamics* 2.1 (1990), pp. 17–30.

[9] William H Press et al. *Numerical recipes 3rd edition: The art of scientific computing*. Cambridge university press, 2007.

[10] Warren J Wiscombe. *Mie scattering calculations: Advances in technique and fast, vector-speed computer codes*. Vol. 10. National Technical Information Service, US Department of Commerce, 1979.

[11] Craig F Bohren and Donald R Huffman. *Absorption and scattering of light by small particles*. John Wiley & Sons, 2008.

[12] Jürgen Weese. "A reliable and fast method for the solution of Fredhol integral equations of the first kind based on Tikhonov regularization". In: *Computer physics communications* 69.1 (1992), pp. 99–111.

[13] Warren J Wiscombe. *MIEV Documentation*. 1996. URL: https://github.com/cfinch/Mie_scattering/blob/master/Wiscombe/MIEV.doc (visited on 09/12/2019).

[14] George M. Hale and Marvin R. Querry. "Optical Constants of Water in the 200-nm to 200-μm Wavelength Region". In: *Appl. Opt.* 12.3 (1973), pp. 555–563. DOI: 10.1364/AO.12.000555. URL: http://ao.osa.org/abstract.cfm?URI=ao-12-3-555.

[15] Nina Sultanova, S Kasarova, and Ivan Nikolov. "Dispersion proper ties of optical polymers". In: *Acta Physica Polonica-Series A General Physics* 116.4 (2009), p. 585.

[16] Peter B Johnson and R-W_ Christy. "Optical constants of the noble metals". In: *Physical review B* 6.12 (1972), p. 4370.

[17] IH Malitson. "Interspecimen comparison of the refractive index of fused silica". In: *Josa* 55.10 (1965), pp. 1205–1209.

[18] J Weese. *FTIKREG: A Program for the Solution of Fredholm Integral Equations of the First Kind, User Manual*. 1991.

[19] Ekspla. *Ekspla NT342*. URL: https://ekspla.com/product/nt342-series-tunable-lasers/ (visited on 09/24/2019).

[20] Robert W Boyd. *Nonlinear optics*. Elsevier, 2003.

[21] Thorlabs. *Thorlabs N-BK7 uncoated*. URL: https://www.thorlabs.com/newgrouppage9.cfm?objectgroup_id=1117 (visited on 09/27/2019).

[22] Mike L Meade. *Lock-in amplifiers: principles and applications*. 1. Mike Meade, 1983.

[23] A De Marcellis et al. "An integrated analog lock-in amplifier for low-voltage low-frequency sensor interface". In: *2007 2nd International Workshop on Advances in Sensors and Interface*. IEEE. 2007, pp. 1–5.

[24] M Davidovic et al. "Monolithically integrated dual-lock-in optical sensor". In: *Electronics Letters* 50.4 (2014), pp. 306–308.

[25] Francisco Paz and Martin Ordonez. "High-performance solar MPPT using switching ripple identification based on a lock-in amplifier". In: *IEEE Transactions on Industrial Electronics* 63.6 (2016), pp. 3595–3604.

[26] Stepan Sutula, Carles Ferrer, and Francisco Serra-Graells. "A 400 μ W Hz-Range Lock-In A/D Frontend Channel for Infrared Spectroscopic Gas Recognition". In: *IEEE Transactions on Circuits and Systems I: Regular Papers* 58.7 (2011), pp. 1561–1568.

[27] Andrea De Marcellis, Giuseppe Ferri, and Arnaldo D'Amico. "One-decade frequency range, in-phase auto-aligned 1.8 V 2 mW fully analog CMOS integrated lock-in amplifier for small/noisy signal detection". In: *IEEE Sensors Journal* 16.14 (2016), pp. 5690–5701.

[28] James F Cox. *Fundamentals of linear electronics: integrated and discrete*. Cengage Learning, 2002.

[29] B. Razavi. *Microelectronics*. Wiley, 2014. ISBN: 9781118165065. URL: https://books.google.it/books?id=3oiRZwEACAAJ.

[30] Andrea De Marcellis, Giuseppe Ferri, and Elia Palange. "A fully analog high performances automatic system for phase measurement of electrical and optical signals". In: *IEEE Transactions on Instrumentation and Measurement* 64.4 (2014), pp. 1043–1054.

[31] Gwyddion. *Gwyddion SPM data analysis software*. URL: http://gwyddion.net/ (visited on 10/11/2019).

[32] PubMed. *PubMed database*. URL: https://www.ncbi.nlm.nih.gov/pubmed (visited on 10/31/2019).

[33] Amarnath Sharma and Uma S Sharma. "Liposomes in drug delivery: progress and limitations". In: *International journal of pharmaceutics* 154.2 (1997), pp. 123–140.

[34] Zehui Cao et al. "Reversible cell-specific drug delivery with aptamer-functionalized liposomes". In: *Angewandte Chemie International Edition* 48.35 (2009), pp. 6494–6498.

[35] Rana Abu-Dahab, Ulrich Friedrich Schäfer, and Claus-Michael Lehr. "Lectin-functionalized liposomes for pulmonary drug delivery: effect of nebulization on stability and bioadhesion". In: *European Journal of Pharmaceutical Sciences* 14.1 (2001), pp. 37–46.

[36] SB Bhise. "Isoniazid toxicity". In: *Journal of Drug Design and Research* 4.7 (2017), p. 1060.

[37] Abdus Samad, Y Sultana, and M Aqil. "Liposomal drug delivery systems: an update review". In: *Current drug delivery* 4.4 (2007), pp. 297–305.

[38] Qingguo Xu, Yasuhiro Tanaka, and Jan T Czernuszka. "Encapsulation and release of a hydrophobic drug from hydroxyapatite coated liposomes". In: *Biomaterials* 28.16 (2007), pp. 2687–2694.

[39] Barbara Ruozi et al. "AFM, ESEM, TEM, and CLSM in liposomal characterization: a comparative study". In: *International journal of nanomedicine* 6 (2011), p. 557.

[40] Christian Isalomboto Nkanga et al. "General Perception of Liposomes: Formation, Manufacturing and Applications". In: *Liposomes-Advances and Perspectives*. IntechOpen, 2019.

[41] Ramsharan Singh et al. "A rapid isocratic high-performance liquid chromatography method for determination of cholesterol and 1, 2-dioleoyl-sn-glycero-3-phosphocholine in liposome-based drug formulations". In: *Journal of Chromatography A* 1073.1-2 (2005), pp. 347–353.

[42] Hiroki Kitayama et al. "Thermotropic phase behavior of hydrogenated soybean phosphatidylcholine–cholesterol binary liposome membrane". In: *Chemical and Pharmaceutical Bulletin* 62.1 (2014), pp. 58–63.

[43] Regine Maget-Dana. "The monolayer technique: a potent tool for studying the interfacial properties of antimicrobial and membrane-lytic peptides and their interactions with lipid membranes". In: *Biochimica et Biophysica Acta (BBA)-Biomembranes* 1462.1-2 (1999), pp. 109–140.

[44] C Huang and JT Mason. "Geometric packing constraints in egg phosphatidylcholine vesicles". In: *Proceedings of the National Academy of Sciences* 75.1 (1978), pp. 308–310.

[45] B De Kruijff, PR Cullis, and GK Radda. "Outside-inside distributions and sizes of mixed phosphatidylcholine-cholesterol vesicles". In: *Biochimica et Biophysica Acta (BBA)-Biomembranes* 436.4 (1976), pp. 729–740.

[46] Sagar A Pandit, David Bostick, and Max L Berkowitz. "Complexation of phosphatidylcholine lipids with cholesterol". In: *Biophysical journal* 86.3 (2004), pp. 1345–1356.

[47] VV Kumar. "Complementary molecular shapes and additivity of the packing parameter of lipids". In: *Proceedings of the National Academy of Sciences* 88.2 (1991), pp. 444–448.

[48] Alfonso Grimaldi et al. "Microglia-derived microvesicles affect microglia phenotype in glioma." In: *Frontiers in cellular neuroscience* 13 (2019), p. 41.

[49] AZ Miller et al. "Bioreceptivity of building stones: a review". In: *Science of the total environment* 426 (2012), pp. 1–12.

[50] Clifford A Price and Eric Doehne. *Stone conservation: an overview of current research*. Getty publications, 2011.

[51] Heiner Siedel and Siegfried Siegesmund. *Characterization of stone deterioration on buildings*. Springer, 2014, pp. 349–414.

[52] Giulia Caneva, Maria Pia Nugari, Ornella Salvadori, et al. *Biology in the Conservation of Works of Art*. 1991.

[53] Th Warscheid and Joanna Braams. "Biodeterioration of stone: a review". In: *International Biodeterioration & Biodegradation* 46.4 (2000), pp. 343–368.

[54] Lars Nordstierna et al. "Molecular release from painted surfaces: Free and encapsulated biocides". In: *Progress in Organic Coatings* 69.1 (2010), pp. 45–48.

[55] Cristopher Dresler et al. "Development of controlled release systems of biocides for the conservation of cultural heritage". In: *International Biodeterioration & Biodegradation* 125 (2017), pp. 150–156.

[56] Harrison Wanyika. "Sustained release of fungicide metalaxyl by mesoporous silica nanospheres". In: *Nanotechnology for Sustainable Development*. Springer, 2013, pp. 321–329.

[57] Amirali Popat et al. "Adsorption and release of biocides with mesoporous silica nanoparticles". In: *Nanoscale* 4.3 (2012), pp. 970–975.

[58] L Ruggiero et al. "Silica nanosystems for active antifouling protection: nanocapsules and mesoporous nanoparticles in controlled release applications". In: *Journal of Alloys and Compounds* 798 (2019), pp. 144–148.

[59] Ludovica Ruggiero et al. "Incorporation of the zosteric sodium salt in silica nanocapsules: synthesis and characterization of new fillers for antifouling coatings". In: *Applied Surface Science* 439 (2018), pp. 705–711.

[60] Hadi Valadi et al. "Exosome-mediated transfer of mRNAs and microRNAs is a novel mechanism of genetic exchange between cells". In: *Nature cell biology* 9.6 (2007), p. 654.

[61] Richard J Simpson et al. "Exosomes: proteomic insights and diagnostic potential". In: *Expert review of proteomics* 6.3 (2009), pp. 267–283.

[62] Douglas D Taylor and Cicek Gercel-Taylor. "MicroRNA signatures of tumor-derived exosomes as diagnostic biomarkers of ovarian cancer". In: *Gynecologic oncology* 110.1 (2008), pp. 13–21.

[63] A Masotti et al. "Oral glucose tolerance test unravels circulating miRNAs associated with insulin resistance in obese preschoolers". In: *Pediatric obesity* 12.3 (2017), pp. 229–238.

[64] Brooke L Deatherage and Brad T Cookson. "Membrane vesicle release in bacteria, eukaryotes, and archaea: a conserved yet underappreciated aspect of microbial life". In: *Infection and immunity* 80.6 (2012), pp. 1948–1957.

[65] Xi Chen et al. "Horizontal transfer of microRNAs: molecular mechanisms and clinical applications". In: *Protein & cell* 3.1 (2012), pp. 28–37.

[66] Mariantonia Logozzi et al. "High levels of exosomes expressing CD63 and caveolin-1 in plasma of melanoma patients". In: *PloS one* 4.4 (2009), e5219.

[67] Cristina Felli, Antonella Baldassarre, and Andrea Masotti. "Intestinal and circulating micrornas in coeliac disease". In: *International journal of molecular sciences* 18.9 (2017), p. 1907.

[68] YongKeun Park, Christian Depeursinge, and Gabriel Popescu. "Quantitative phase imaging in biomedicine". In: *Nature Photonics* 12.10 (2018), pp. 578–589.

[69] Terry J Beveridge. "Structures of gram-negative cell walls and their derived membrane vesicles". In: *Journal of bacteriology* 181.16 (1999), pp. 4725–4733.

[70] Steven J Biller et al. "Bacterial vesicles in marine ecosystems". In: *science* 343.6167 (2014), pp. 183–186.

[71] Terry J Beveridge et al. "Interactions between biofilms and the environment". In: *FEMS Microbiology Reviews* 20.3-4 (1997), pp. 291–303.

[72] Judith Hellman et al. "Release of Gram-Negative Outer-Membrane Proteins into Human Serum and Septic Rat Blood and Their Interactions with Iminunoglobulin in Antiserum to Eschevichia coli J5". In: *The Journal of infectious diseases* 181.3 (2000), pp. 1034–1043.

[73] Eun-Young Lee et al. "Gram-positive bacteria produce membrane vesicles: proteomics-based characterization of Staphylococcus aureus-derived membrane vesicles". In: *Proteomics* 9.24 (2009), pp. 5425–5436.

[74] Johanna Rivera et al. "Bacillus anthracis produces membrane-derived vesicles containing biologically active toxins". In: *Proceedings of the National Academy of Sciences* 107.44 (2010), pp. 19002–19007.

[75] Hildgund Schrempf et al. "Extracellular Streptomyces vesicles: amphorae for survival and defence". In: *Microbial biotechnology* 4.2 (2011), pp. 286–299.

[76] Jung Hwa Lee et al. "Transcription factor σB plays an important role in the production of extracellular membrane-derived vesicles in Listeria monocytogenes". In: *PloS one* 8.8 (2013), e73196.

[77] Yanlong Jiang et al. "Membrane vesicles of Clostridium perfringens type A strains induce innate and adaptive immunity". In: *International journal of medical microbiology* 304.3-4 (2014), pp. 431–443.

[78] Sumei Liao et al. "Streptococcus mutans extracellular DNA is upregulated during growth in biofilms, actively released via membrane vesicles, and influenced by components of the protein secretion machinery". In: *Journal of bacteriology* 196.13 (2014), pp. 2355–2366.

[79] Scott N Dean et al. "Targeting and delivery of therapeutic enzymes". In: *Therapeutic delivery* 8.7 (2017), pp. 577–595.

[80] Leo van der Pol, Michiel Stork, and Peter van der Ley. "Outer membrane vesicles as platform vaccine technology". In: *Biotechnology journal* 10.11 (2015), pp. 1689–1706.

[81] D Bottero et al. "Characterization of the immune response induced by pertussis OMVs-based vaccine". In: *Vaccine* 34.28 (2016), pp. 3303–3309.

[82] Xiaogang Wang et al. "Release of Staphylococcus aureus extracellular vesicles and their application as a vaccine platform". In: *Nature communications* 9.1 (2018), p. 1379.

[83] Terri N Ellis and Meta J Kuehn. "Virulence and immunomodulatory roles of bacterial outer membrane vesicles". In: *Microbiol. Mol. Biol. Rev.* 74.1 (2010), pp. 81–94.

[84] Nicolas Michel et al. "Determination of phase transition temperatures of lipids by light scattering". In: *Chemistry and physics of lipids* 139.1 (2006), pp. 11–19.

[85] Simone Aleandri et al. "How stereochemistry affects the physicochemical features of gemini surfactant based cationic liposomes". In: *Soft Matter* 8.21 (2012), pp. 5904–5915.

[86] Hermann Träuble and Peter Overath. "The structure of Escherichia coli membranes studied by fluorescence measurements of lipid phase transitions". In: *Biochimica et Biophysica Acta (BBA)-Biomembranes* 307.3 (1973), pp. 491–512.

[87] Jacek T Mika et al. "Measuring the viscosity of the Escherichia coli plasma membrane using molecular rotors". In: *Biophysical journal* 111.7 (2016), pp. 1528–1540.

[88] Allen G Marr and John L Ingraham. "Effect of temperature on the composition of fatty acids in Escherichia coli". In: *Journal of Bacteriology* 84.6 (1962), pp. 1260–1267.

[89] Stephen W Provencher. "A constrained regularization method for inverting data represented by linear algebraic or integral equations". In: *Computer Physics Communications* 27.3 (1982), pp. 213–227.

[90] Chris De Vos, Luc Deriemaeker, and Robert Finsy. "Quantitative assessment of the conditioning of the inversion of quasi-elastic and static light scattering data for particle size distributions". In: *Langmuir* 12.11 (1996), pp. 2630–2636.

[91] H Amenitsch, S Bernstorff, and P Laggner. "High-flux beamline for small-angle x-ray scattering at ELETTRA". In: *Review of scientific instruments* 66.2 (1995), pp. 1624–1626.

[92] AP Hammersley. "FIT2D V12. 012 Reference Manual V6. 0". In: *ESRF International Report No. ESRF98HA01T. Program available at http://www. esrf. eu/computing/scientific/FIT2D* (2004).

[93] Ingo Berndt, Jan Skov Pedersen, and Walter Richtering. "Structure of Multiresponsive "Intelligent" Core- Shell Microgels". In: *Journal of the American Chemical Society* 127.26 (2005), pp. 9372–9373.

[94] Francesco Spinozzi et al. "GENFIT: software for the analysis of small-angle X-ray and neutron scattering data of macromolecules in solution". In: *Journal of applied crystallography* 47.3 (2014), pp. 1132–1139.

[95] M Cerreto et al. "Effect of the irradiation on Neuroblastoma-derived microvesicles: A physical and biological investigation". In: *Colloids and Surfaces A: Physicochemical and Engineering Aspects* 532 (2017), pp. 195–202.

[96] Philip Laven. *MiePlot*. URL: http://philiplaven.com/mieplot.htm. (visited on 10/11/2019).

[97] Philip Laven. "Simulation of rainbows, coronas, and glories by use of Mie theory". In: *Applied optics* 42.3 (2003), pp. 436–444.

[98] Wonshik Choi et al. "Tomographic phase microscopy". In: *Nature methods* 4.9 (2007), p. 717.

[99] Robert E Marquis. "Immersion refractometry of isolated bacterial cell walls". In: *Journal of bacteriology* 116.3 (1973), pp. 1273–1279.

[100] Bruce J Berne and Robert Pecora. *Dynamic light scattering: with applications to chemistry, biology, and physics*. Courier Corporation, 2000.

[101] Sven Morein et al. "Wild-type Escherichia coli cells regulate the membrane lipid composition in a window between gel and non-lamellar structures". In: *Journal of Biological Chemistry* 271.12 (1996), pp. 6801–6809.

[102] Gisèle F White et al. "Physical properties of liposomes and proteoliposomes prepared from Escherichia coli polar lipids". In: *Biochimica et Biophysica Acta (BBA)-Biomembranes* 1468.1-2 (2000), pp. 175–186.

[103] Daniele P Romancino et al. "Palmitoylation is a post-translational modification of Alix regulating the membrane organization of exosome-like small extracellular vesicles". In: *Biochimica et Biophysica Acta (BBA)-General Subjects* 1862.12 (2018), pp. 2879–2887.

[104] Peter N Pusey. "Introduction to scattering experiments". In: *Neutrons, X-rays, and light: scattering methods applied to soft condensed matter. Amsterdam: Elsevier* 46 (2002), pp. 3–22.

[105] Wyn Brown. *Dynamic light scattering: the method and some applications*. Vol. 313. Clarendon press Oxford, 1993.

[106] Zukang Zhou and Benjamin Chu. "Light-scattering study on the fractal aggregates of polystyrene spheres: Kinetic and structural approaches". In: *Journal of colloid and interface science* 143.2 (1991), pp. 356–365.

[107] HZ Cummins and ER Pike. *Photon Correlation and Light Beating Spectroscopy, 1974*.

[108] Harbans S Dhadwal, Rafat R Ansari, and William V Meyer. "A fiber-optic probe for particle sizing in concentrated suspensions". In: *Review of scientific instruments* 62.12 (1991), pp. 2963–2968.

[109] Helmut Kohl and Ludwig Reimer. *Transmission electron microscopy: physics of image formation*. Springer, 2008.

[110] Weilie Zhou et al. "Fundamentals of scanning electron microscopy (SEM)". In: *Scanning microscopy for nanotechnology*. Springer, 2006, pp. 1–40.

[111] Robert Anderhalt. "X-ray microanalysis in nanomaterials". In: *Scanning Microscopy for Nanotechnology*. Springer, 2006, pp. 76–100.